Master thesis

Process-oriented study on events of unusual winter time CO_2 fluxes at the Bayelva site, Spitsbergen

Katharina Jentzsch

Institute of Geophysics and Meteorology

University of Cologne

Supervision:

Prof. Dr. Susanne Crewell (University of Cologne)

Prof. Dr. Julia Boike (Alfred Wegener Institute for Polar and Marine Research, Potsdam)

Date:

May 27, 2020

Abstract

The release of carbon dioxide from Arctic permafrost soils is both a consequence and a driver of the amplified increase of near-surface temperatures observed in the Arctic. The warming is most intense during the winter months where the CO_2 exchange is still poorly explored due to the extreme conditions of the Arctic winter. This study aims to contribute to a better understanding of the physical processes driving the CO_2 fluxes during the winter months based on a one year time series of eddy covariance flux estimates from the high Arctic Bayleva site. Its focus is on time periods of hours to days, where the magnitude of the CO_2 fluxes significantly exceeds its typical range of variation. These time periods are generally associated with an exchange of the large scale air masses influencing the study site and particularly occur simultaneously with high wind speeds. While fluxes indicating an unexpected uptake of CO_2 by the soil during the winter months are most likely related to sensor limitations, no clear measurement issues could be identified for time periods of apparent strong CO_2 release to the atmosphere. The advection of CO_2 rich air to the study site from remote regions is likely to be the most important cause of these observations, while the abrupt release of CO_2 stored below the measurement height or inside the snow pack might have an additional, although smaller, impact. In order to separate the individual contributions and to exclude any methodological issues, further research on the topic is urgently needed. Since the CO_2 flux events in total account for a significant part of 30 % of the net annual carbon uptake, their handling has pronounced implications for the quantification of the current Arctic carbon cycle. However, since the events of apparent intense CO_2 exchange are not yet sufficiently understood, their handling probably differs significantly among studies. Especially in the context of long term studies the events might easily even go unnoticed. When using already available flux data sets as an input for large scale modelling efforts, the presence of winter time CO_2 flux events at comparable study sites all over the Arctic region might thus introduce an unexpected uncertainty to future climate projections.

Table of Contents

1 Introduction

Over the past 150 years, the global mean near-surface air temperature has increased by 0.87 °C (AC3, 2015). In the Arctic this warming is amplified, since the 1990s exceeding the global warming by a factor of 2 to 3 (Figure 1.1).

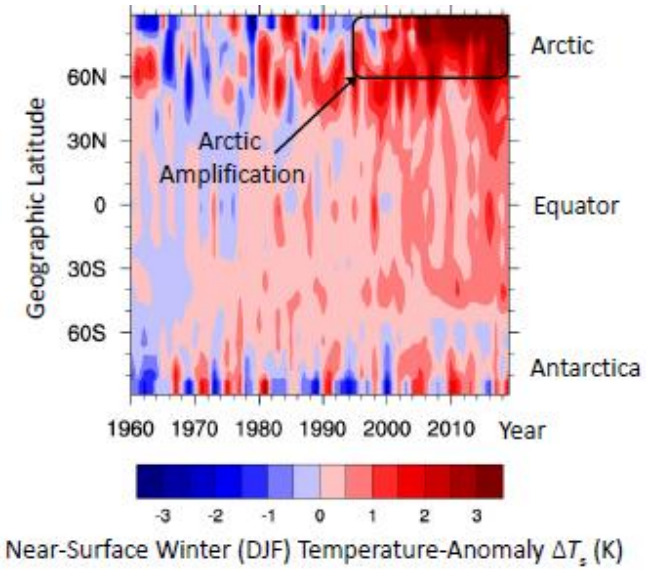

Figure 1.1: Zonally averaged, near-surface air temperature anomaly, averaged over the boreal winter season (December, January, February). The anomaly is given as the difference to the respective mean values for 1951 to 1980. (AC3, 2015 as adapted from Wendisch et al., 2017, based on data provided by the NASA Goddard Institute for Space Studies Team)

The excessive Arctic warming, which is predicted to proceed during the 21st century, is both a consequence and a driver of physical and biochemical feedback processes resulting from the unique Arctic conditions, atmospheric and oceanic transport of heat, humidity, and momentum as well as the tropospheric and stratospheric circulation (AC3, 2015). One feedback mechanism which is expected to gain more importance in the course of ongoing temperature increase is the permafrost carbon – climate feedback (Figure 1.2). Although a little delayed the strong warming trend results in an increase of permafrost temperatures all over the Arctic region (Biskaborn et al., 2019). When the permafrost starts to thaw, substantial quantities of organic carbon, stored in the frozen ground, are exposed to decomposition by soil microbes. A part of the carbon is consequently released to the atmosphere in the form of the greenhouse gases carbon dioxide and methane. The subsequent increase of their atmospheric concentration further amplifies the greenhouse effect, leading to even higher air temperatures and thus resulting in a positive feedback loop with global implications.

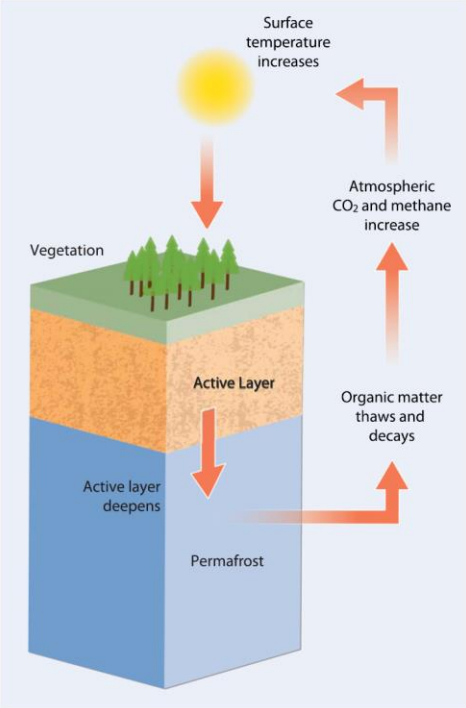

Figure 1.2: Scheme of the permafrost carbon–climate feedback (Schaefer et al., 2014).

Estimates of current permafrost soil carbon stocks amount to 1700 PgC (Tarnocai et al., 2009), which is about twice as much as is currently present in the atmosphere (Schuur et al., 2015). Today the terrestrial Arctic is considered as a net sink for CO_2 of between 0.3 and 0.6 $PgCyr^{-1}$ (Ciais et al., 2013), but is expected to become a carbon source at the latest by 2100 for all Representative Concentration Pathways (Abbott et al., 2016). On the whole, the permafrost carbon – climate feedback is predicted to cause between 0.13 °C and 0.27 °C additional global warming by 2100 and up to 0.42 °C by 2300 (Schuur et al., 2015). All of these predictions are model results, which are calculated based on information about the current state of the Arctic carbon cycle. However these input data are already subject to substantial uncertainties, introduced by a serious lack of long term flux observations in the remote Arctic regions. Flux measurements are particularly scarce for the winter months (Figure 1.3), where the Arctic warming is most pronounced (e.g. Serreze & Barry, 2011). This lack of data is particularly problematic with regard to the high temporal and spatial variability of the emissions, which complicates an upscaling of in situ measurements (ICOS, 2018). The scarcity of measurements furthermore hampers discoveries on the physical mechanisms controlling the CO_2 exchange between soil and atmosphere. In addition to the permafrost carbon-climate feedback, other processes, like changes in vegetation or water balance, might further amplify, offset or even compensate the release of CO_2 from thawing permafrost.

Both a densification of the observational network as well as deeper insights into permafrost landscape dynamics are urgently needed in order to refine the incorporation of carbon exchange processes into global climate models. This is the basic prerequisite to obtain reliable estimates on the net effect of permafrost carbon dynamics and thus on the future trajectory of global climate.

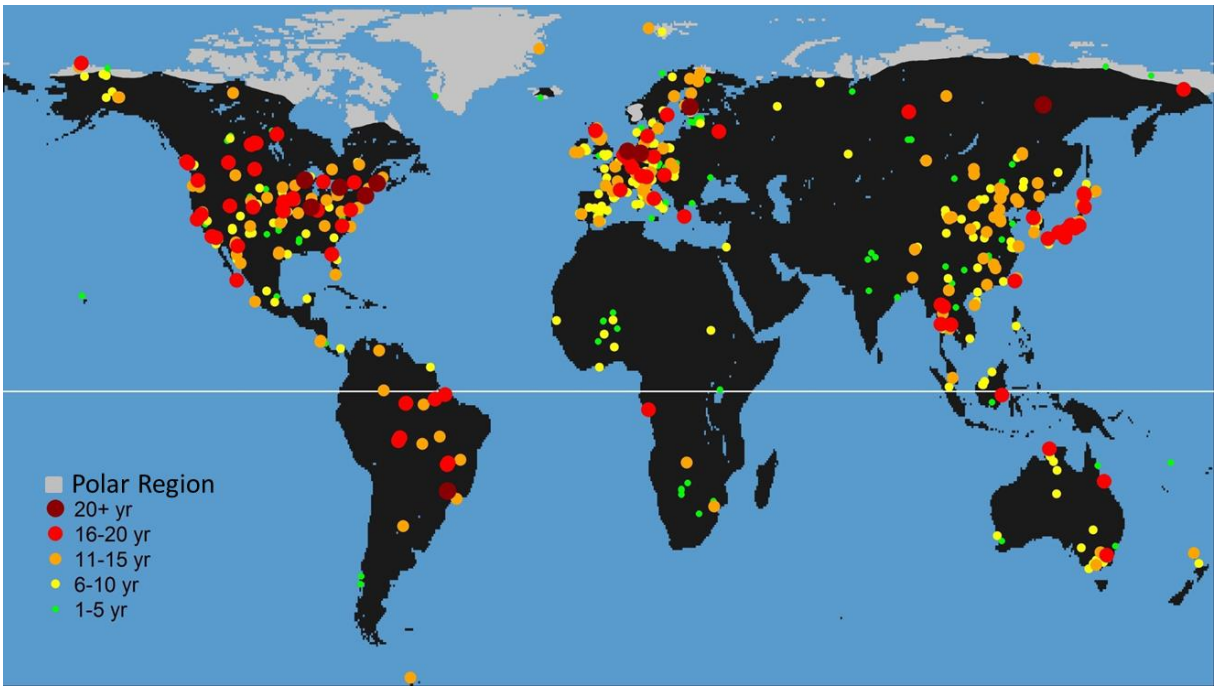

Figure 1.3: Eddy Covariance tower sites that participate in the FLUXNET 2015 Dataset and their operation period. (Adapted from FLUXNET, 2015). However the depicted data set length for the Arctic stations might even be too long, since at least the data uploaded for the two sites on Svalbard actually only comprise four and two years of flux data, respectively.

The aim of this thesis is to contribute to a better understanding of the physical drivers behind the surface CO_2 exchange in the Arctic during the winter time. Since CO_2 fluxes are generally small during the Arctic winter, their importance can easily be underestimated. However in polar regions wintry conditions are present during a large part of the year, rendering the total winter fluxes a major part of the annual carbon budget. The study is based on a one-year time series of half-hourly CO_2 flux estimates obtained from eddy covariance (EC) measurements at the high Arctic Bayelva site on Spitsbergen in 2015. Its focus is on time periods on the order of hours to several days during the winter time, where flux values indicate an unusually strong CO_2 uptake by the soil or release to the atmosphere. By discussing various physical and methodological approaches, the study aims at uncovering the reasons for the observed exchange processes. Once validated at other sites, the findings obtained from this thesis could on the one hand provide general recommendations on the handling of EC data from Arctic sites and on the other hand contribute to an improved representation of the Arctic carbon cycle in large scale modelling efforts.

The thesis is structured as follows. In chapter 2 the study is placed in the context of the current state of research on the topic. In chapter 3 the research site and the measurement setup as well as the sources of the data sets used in this study will be introduced. Chapter 4 illuminates the theoretical framework as well as the processing methodology. Chapter 5 finally presents the research results obtained in this study. Chapter 6 and discusses the implications of the study results for annual carbon budget studies. Chapter 7 summarizes the final results and suggests approaches for future research on the topic.

2 Observations and handling of unusual CO_2 fluxes in the literature

Time periods characterized by unusually high CO_2 fluxes have been observed in several studies applying the EC method in high-latitude ecosystems. This chapter therefore summarizes relevant observations stated in the literature, various explanatory approaches as well as the conclusions drawn concerning an appropriate handling of these flux estimates.

At the Bayelva site such events have already been observed by Lüers et al. (2014) between 2008 and 2009 during periods with high wind speeds and marked changes in atmospheric pressure. With a total absolute contribution of 2 to 3 gCm^{-2} per event, they bear a significant impact on the annual carbon budget (Lüers et al., 2014). Less influential episodic increases in CO_2 fluxes at high wind speeds were also documented by Pirk et al. (2017) for a second research site on Svalbard. The correlation between strong changes in meteorological parameters and gas fluxes is apparently not limited to CO_2 since Schaller et al. (2019) recently investigated episodic outbursts of CH_4 emission under similar environmental conditions in north-east Siberia.

Particularly challenging is the explanation of downward-directed CO_2 fluxes during the winter months, where they cannot be attributed to biotic uptake by photosynthesis. Nonetheless an apparent CO_2 uptake during the snow-covered season was found to significantly contribute to the annual carbon balance at various sites. For instance Kittler et al. (2017) recorded CO_2 uptake rates of up to 2 $\mu molm^{-2}s^{-1}$ in north-east Siberia. Hirata et al. (2005) and Ono et al. (2007) observed downward-directed CO_2 fluxes of up to 6 $\mu molm^{-2}s^{-1}$ and 5.9 $\mu molm^{-2}s^{-1}$, respectively at two sites in Japan. In the Canadian subarctic, Amiro (2010) similarly documents an unexpected CO_2 uptake during the winter months and Lafleur and Humphreys (2008) quantify its rate to 0.9 $\mu molm^{-2}s^{-1}$. Zhang et al. (2011) postulate a general long-term negative offset of the CO_2 flux time series, resulting in an underestimation of ecosystem respiration and an overestimation of photosynthetic carbon uptake.

Although similar unusually high absolute flux values are observed at many sites, there is a wide spread concerning the handling of these unexpected flux estimates across studies. On the one hand various physical mechanisms are proposed to cause the observed fluxes. Probably the most widely accepted hypothesis in this context is an episodic release of CO_2 rich air from the soil (Takle et al. 2004; Gu et al. 2005) or snow pores (Massman et al. 1997; Massman and Lee 2002), associated with wind-induced fluctuations in atmospheric pressure. This effect has also been confirmed by CO_2 concentration measurements performed directly inside the snow pack (Takagi et al. 2005; Seok et al., 2009; Graham & Risk, 2018). Another theory is that during high wind speeds the CO_2, which accumulated close to the ground during periods of stable atmospheric stratification, is all at once transported upwards to the measuring instruments (Aubinet et al., 2012; Schaller et al., 2019). Pirk et al. (2017) furthermore speculate that abiotic mechanisms, such as the exchange of CO_2-depleted gas stored in the snow pores, namely a reverse of the snow cover ventilation proposed for CO_2 emission, or CO_2 solution in meltwater, as recorded in ice cores by Jinho et al. (2008), could contribute to the apparent CO_2 uptake during the winter months. Yet so far no evidence could be found to support these propositions. Ma et al. (2014), furthermore suggest an absorption of dissolved carbon by rising groundwater. Details on the suggested physical mechanisms will be given in section 4.5 of this

study. Advection could furthermore lead to non-local contributions which might introduce a bias to the CO_2 fluxes when using the conventional EC method (Aubinet et al., 2012; Sievers et al., 2015; Schaller et al., 2019). However the overall issue is that most of the proposed physical processes can probably not explain the large magnitude of the observed fluxes (Lüers et al., 2014).

Therefore in the following, several studies will be presented, which on the other hand rate the observed fluxes as erroneous and unphysical, based on known shortcomings of the EC method in cold and low-flux environments. The EC technique is widely used to investigate the exchange of gas and energy at the earth's surface as it allows for long-term continuous flux measurements with a high temporal resolution at the ecosystem scale (Zhang et al., 2011; Schaller et al. 2019). However strict theoretic assumptions like steady-state conditions and a well-developed turbulent flow have to be met in order to ensure high-quality flux estimates (Foken & Wichura, 1996). At high latitudes these requirements cannot always be guaranteed for example due to environmental phenomena like the typically very stable atmospheric stratification, which largely inhibits turbulent exchange during the polar winter (Schaller et al., 2019). In addition to that, the harsh Arctic climate in combination with generally low absolute fluxes poses several technical challenges to the flux measurements. These are related among others to the low temperatures and a possible icing of the measurement sensors (Kittler et al., 2017; Goodrich et al., 2016). These issues are most severe during the winter months in remote areas where regular maintenance of the instruments cannot always be ensured. They are particularly associated with open-path gas analyzers (Kittler et al., 2017; Butterworth & Else, 2018) and generally assumed to cause the observed disagreement between the EC method and the enclosure technique using chamber measurements. Since chamber measurements do not only alter the environment being measured (Miller et al., 2015), but also require a high degree of manual service and are spatially confined to the centimeter-scale region enclosed by the chamber (Butterworth & Else, 2018), they are however not suited to replace EC measurements for collecting long-term, ecosystem-scale flux datasets in such remote regions. As opposed to open-path gas analyzers, fluxes obtained from closed-path measurements show significantly lower deviation from enclosure studies (Butterworth & Else, 2018). The main difference between the two gas analyzer types is that a closed-path instrument includes a housing of the measurement cell, whereas the optical path of open-path sensors is exposed to the atmosphere. Since open-path gas analyzers feature the advantage of requiring comparably little power and maintenance, several correction procedures have been derived from adjusting open-path to simultaneous closed-path measurements. These include corrections for additional sensible heat fluxes caused by instrument self-heating (Burba et al., 2006, 2008; Oechel et al., 2014; Kittler et al., 2017; Amiro 2010; Clement et al., 2009; Helbig et al., 2016), an enhanced correction for air temperature fluctuations (Hirata et al., 2005) as well as air pressure fluctuations (Zhang et al., 2010). Nevertheless the applied corrections are at times still insufficient to completely compensate the spurious flux contributions (Goodrich et al. 2016; Kittler et al. 2017). Butterworth and Else (2018) therefore regard open-path sensors as entirely unsuitable for the observation of the generally small CO_2 fluxes during the Arctic winter and instead promote the application of dried, closed-path gas analyzers.

Nonetheless it has to be taken into account that, even though a reference data set always helps to assess the reliability of flux estimates, simply taking closed-path or chamber measurements as the truth and adjusting open-path observations based on this assumption, might be problematic as well. Since they alter the temperature, radiation, pressure gradient, wind speed, turbulence and CO_2 concentration gradient inside the sample volume (Miller et al., 2015), the closed-path and particularly the enclosure technique, apart from excluding certain sources of error, might just as well exclude relevant physical processes. Furthermore, although the majority of studies documenting spurious winter time gas exchange employ open-path gas analyzers, events of unusually large fluxes of methane (Göckede et al., 2019; Schaller et al., 2019) and CO_2 (Pirk et al., 2017) are also observed with closed-path gas analyzers.

Ono et al. (2007) conclude that, according to mass conservation, when a downward turbulent CO_2 flux is observed in the absence of a local chemical reaction like photosynthesis or CO_2 solution in meltwater, at least one of the following requirements have to be met. The bare-soil surface has to be a net sink of CO_2, and/or CO_2 molecules are accumulated below the measurement point and/or the advective flux contributions are not negligible, and/or the turbulent flux itself has been incorrectly measured as a result of theoretical and practical issues.

The current state of research expresses the urgent need for a detailed quality assessment of winter time Arctic CO_2 fluxes before including them in cross-site annual carbon balance studies as recently performed by Natali et al. (2019). Especially in long-term studies, where short-term flux events cannot be thoroughly investigated, unusually high fluxes during the winter time are in some cases probably just removed from the time series as unphysical outliers. Particularly when gap filled, the resulting time series can give rise to a serious underestimation of the annual carbon budget and distort the actual effect of the current Arctic carbon cycle on the climate dynamics. Therefore further insights into the winter time Arctic CO_2 fluxes are needed in order to make general recommendations on how to deal with the widely observed unusual flux estimates and in order to improve the parameterization of permafrost carbon dynamics in global climate models.

Based on these highly topical open research questions, my master thesis primarily focusses on unusual CO_2 flux events instead of regarding them as a secondary issue next to the desired long-term studies. The various approaches in handling these unexpected CO_2 fluxes have mainly been discussed separately so far. Therefore my goal is to bring them together, combine them with further methodological approaches and quantify their explanatory power at the example of the high Arctic Bayelva site. With this I intend to close in on a general explanation of the not yet sufficiently understood but highly relevant flux events.

3 Study site and data sources

In the following section the research site and the data sets utilized in this study will be introduced. After giving a general overview of the location and topography as well as the climate, vegetation, soil and permafrost conditions of the study site in section 3.1, the focus will be on the setup and instrumentation of the EC system in section 3.2. Section 3.3 presents the auxiliary data, which is used in addition to the flux data obtained from the EC system.

3.1 The Bayelva research site

This study is based on measurement data recorded at the high Arctic Bayelva research site, run by Alfred Wegener Institute (AWI). The central part of the site is a soil and climate research station, which monitors meteorological and permafrost conditions since 1998 and provides the background data for my analyses (Section 3.3). The CO_2 fluxes discussed in this thesis, along with fluxes of sensible and latent heat, are estimated based on measurements of a nearby EC system, operated between 2007 and 2017 (Section 3.2). Over the past three decades the Bayelva site has been the focus of intensive investigations into fluvial hydrology (Hodson et al., 2002), soil and permafrost conditions (Boike et al., 2008, 2018; Roth & Boike, 2001; Westermann, 2010; Westermann et al., 2011), the surface energy balance (Boike et al., 2003; Westermann et al., 2009a, b, Lüers & Boike, 2013) and the micrometeorological processes controlling the surface gas and energy exchanges (Lloyd, 2001a; Lloyd et al., 2001; Lüers & Bareiss, 2010, 2011, 2013; Lüers et al., 2014).

The Bayelva site is located at 78°55'N and 11°50'E in the European high Arctic, about 2 km south west of the research settlement of Ny Ålesund, on the southern shore of the Kongsfjorden fjord on the island of Spitsbergen in the north west of the Svalbard archipelago (Figure 3.1). Due to the strong influence of the West Spitsbergen Ocean Current, a branch of the North Atlantic Current, the area is characterized by a maritime climate with cool summer and comparatively mild winter temperatures, given its latitude. Between 1998 and 2018 the mean annual air temperature amounted to -4.2 °C and was subject to an increase of +1.46 °C (± 0.05 °C) per decade (Bacher, 2019). During the same time period the annual liquid precipitation sums ranged from 139.1 mm to 394.1 mm with an increase of 76 mm (± 44 mm) per decade (Bacher, 2019). The area is typically snow covered for the eight months from October to May (Ebenhoch, 2018). The study site is located in the Bayelva catchment area, which is bordered by two mountains, Zeppelinfjellet and Scheteligfjellet, with the glacial Bayelva River originating from the two branches of the Brøggerbreen glacier on either side of the Brøggerfjellet (Figure 3.1 d). The terrain flattens out to the north of the study site and the Bayelva River flows into the Kongsfjorden and into the Arctic Ocean about 1 km downstream (Lüers et al., 2014). The weather and permafrost station is situated on the top of the Leirhaugen hill at approximately 25 m a.s.l. while the EC system was installed at about 20 m a.s.l. on its by less than 5° inclined north western slope. Within the hilly tundra of the Bayelva catchment, areas of sparse vegetation alternate with exposed soil and sand or rock fields. Typical permafrost features, such as non-sorted circles, form the dominant ground pattern (Boike et al., 2018). Continuous permafrost underlies the unglaciated coastal areas to a depth of about 100 m (Humlum, 2005). The rise in air temperature is also reflected in the permafrost

temperatures as well as in an increase in active layer thickness of 5 ± 0.7 cmyear^{-1} between 1999 and 2016 (Ebenhoch, 2018).

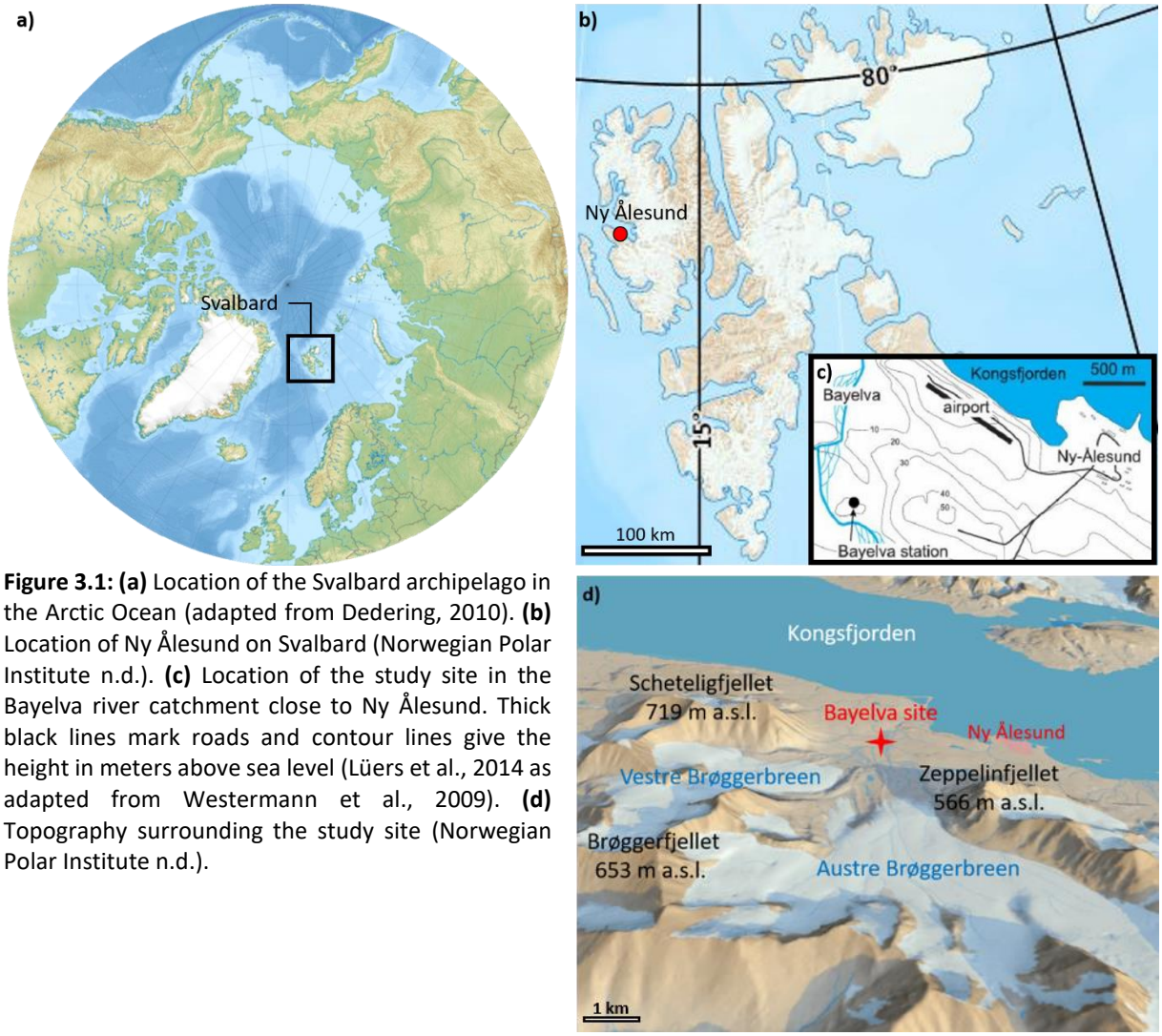

Figure 3.1: (a) Location of the Svalbard archipelago in the Arctic Ocean (adapted from Dedering, 2010). **(b)** Location of Ny Ålesund on Svalbard (Norwegian Polar Institute n.d.). **(c)** Location of the study site in the Bayelva river catchment close to Ny Ålesund. Thick black lines mark roads and contour lines give the height in meters above sea level (Lüers et al., 2014 as adapted from Westermann et al., 2009). **(d)** Topography surrounding the study site (Norwegian Polar Institute n.d.).

3.2 Eddy Covariance system

The EC system operated between March 2007 and October 2017. Due to its remote location and because the system initially ran on solar and wind power, the choice of measurement instruments was limited to low power sensors, which need a minimum of manual maintenance. The measurement setup therefore consists of a CSAT3 ultrasonic anemometer and a LI-7500 open-path infrared gas analyser, which was updated to LI-7500A in 2014 and to LI-7500RS in 2017. Both instruments are mounted on a mast, in 2015 at a height above the snow free ground of 2.75 m (Figure 3.2). Figure 3.2 c visualizes the average flux source area of the EC system as determined by Westermann et al. (2009). The image reveals that most of the contributing surface flux originates from an area along the prevailing wind directions, which is unobstructed by man-made structures. The orientation of the measurement setup with respect to the local wind field is assessed in more detail in section 5.2.2.1.

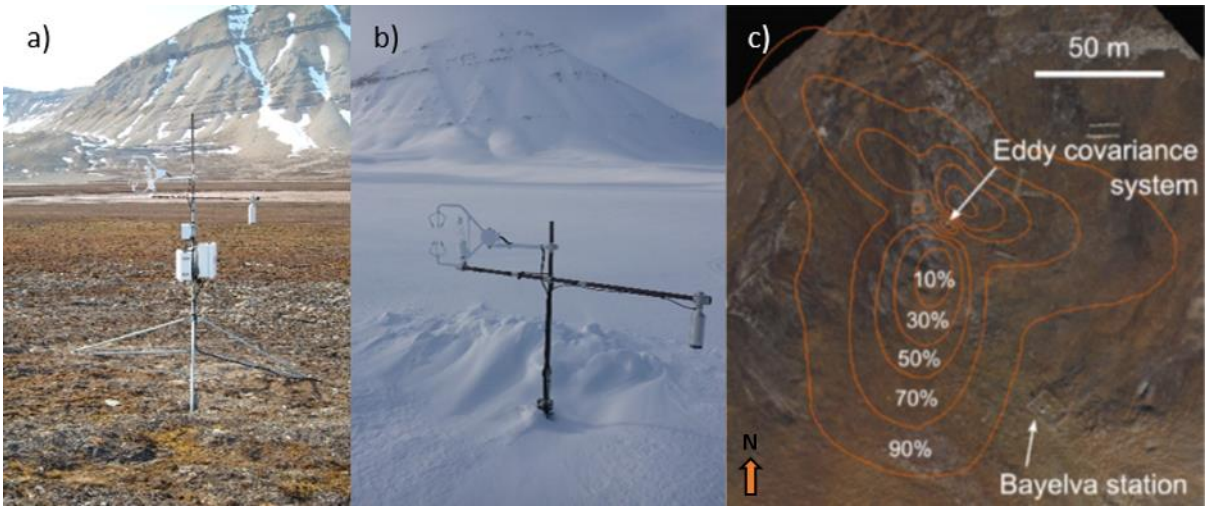

Figure 3.2: View of the EC system in **(a)** July 2009 (photo by AWI member) and **(b)** April 2014 (photo by S. Frey, AWI), when facing west. **(c)** The average footprint of the EC system from 01.07.2008 to 30.09.2008 with fractions of the total flux originating within the respective contours, superimposed on an orthorectified aerial photo (adapted from Westermann et al., 2009 by Lüers et al., 2014).

The CSAT3 calculates the wind speed and the speed of sound along the three non-orthogonal sonic axes from the flight times of two ultrasonic waves transmitted between each of the three pairs of transducers (Figure 3.3 a). The three wind components are then rotated to form the orthogonal x, y and z components of the velocity vector in the instrument frame. Making use of the direct relationship between the speed of sound and the air density, i.e. temperature and humidity, the average sonic virtual temperature T_S between the sonic axes is derived.

The LI-7500 samples the densities of CO_2 and water vapour in its measurement path (Figure 3.3. b). A rotating chopper filter wheel makes the wavelengths of an infrared beam transmitted between an infrared source and detector alternate between the non-absorbing reference bands at 3.95 µm for CO_2 and at 2.4 µm for water vapour, the CO_2 absorption band at 4.26 µm and the water vapour absorption band at 2.59 µm. The gas densities are then calculated from the attenuation of the absorption bands along the measurement path compared to the reference. With the firmware update in 2014, the chopper motor housing temperature was set to a lower operating temperature of 5 °C. This winter setting reduces power consumption and minimizes heating by the electronics (LI-COR Inc., 2015). Further information on the specifications of the sensors can be obtained from the respective manuals (Campbell Scientific Inc., 1998; LI-COR Inc., 2001, 2009, 2015).

At Bayelva both the measurements of the anemometer as well as of the gas analyser are performed at a frequency of 20 Hz. To account for the changing height of the EC system due to the snow cover dynamics, the snow depth is recorded every minute using an ultrasonic ranging sensor. Additionally half hourly averages of atmospheric pressure and temperature are derived from high frequency measurements recorded by the gas analyser box.

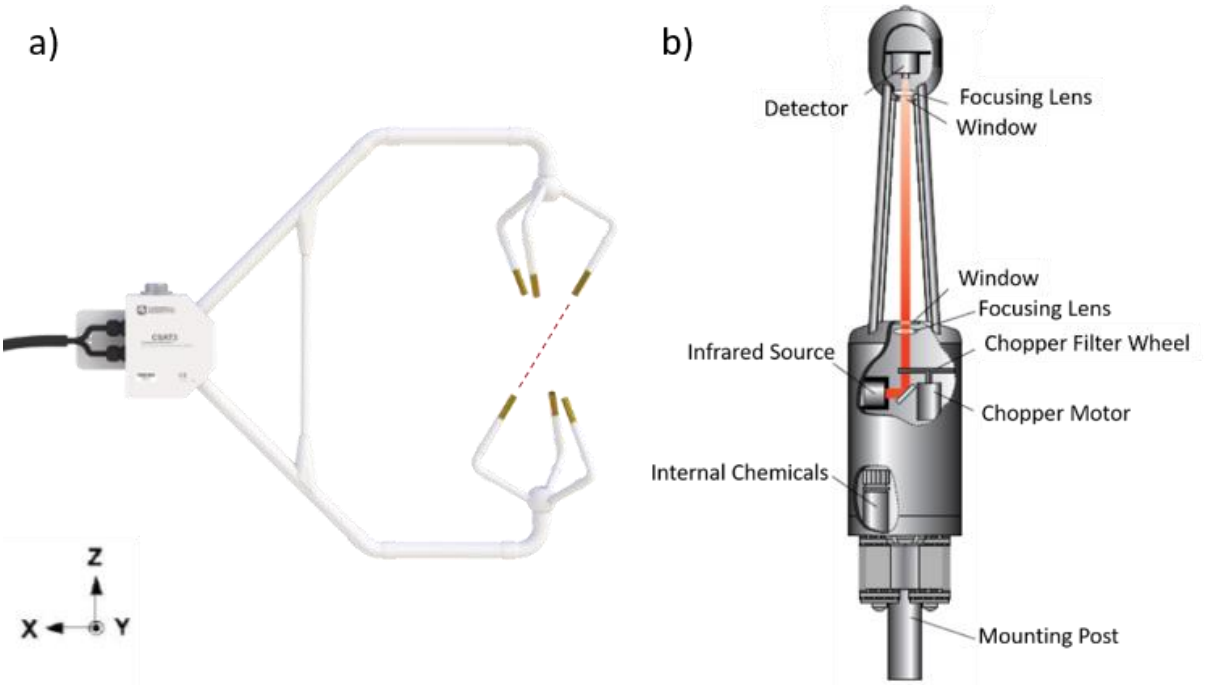

Figure 3.3: Schematic of **(a)** the non-orthogonal geometry of a CSAT3 sonic anemometer head. The red line visualizes one of the three acoustic paths between the pairs of transducers and the coordinate system shows the three components of the velocity vector in the instrument frame (adapted from Campbell Scientific Inc., 1998) and **(b)** the LI-7500 open-path infrared gas analyser (adapted from LI-COR Inc., 2009).

3.3 Auxiliary data

In addition the flux data obtained from the EC system several other data sets are used to characterize the environmental conditions during the CO_2 flux events. Most of the auxiliary data originates from the Bayelva meteorological and soil station. The meteorological parameters involve the 2 m air temperature, relative humidity, incoming and outgoing short- and longwave radiation, liquid precipitation, snow depth, snow dielectric number and snow temperature, which are available at half hourly resolution. The soil variables of soil temperature and volumetric liquid water content are recorded once per hour at depths between 1 and 89 cm. An additional temperature sensor is installed at a depth of 141 cm. A detailed overview of the measured variables, the instruments employed as well as the resulting long-term data set is provided by Boike et al. (2018). Atmospheric pressure measurements with a temporal resolution of one minute from the Baseline Surface Radiation Network (BSRN) station in Ny Ålesund were used to validate the observations obtained from the EC system. The pressure recorded at the Bayelva EC site was found to be constantly lower than the one at the BSRN site by about 2.5 hPa, which can be attributed to the pressure decrease with the height above the sea level. Due to the otherwise good agreement of the two time series the local pressure measurements at the EC system are rated as suitable for the further analyses. Furthermore hourly recorded photographs of the study area were used along with photographs of the larger area around Ny Ålesund, obtained from the webcam installed on Zeppelin Mountain (Pedersen, 2013).

In addition to the in situ measurements, reanalysis data are used to assess larger scale circulation patterns. On a 0.25°x0.25° grid hourly ERA5 geopotential and horizontal wind

speed components on the 850 hPa level (obtained from Climate Data Store: https://cds.climate.copernicus.eu/cdsapp#!/home) are used to visualize and identify the synoptic situation and dominant weather systems over the Arctic Ocean. In addition to that, the circulation weather types (CWT) classification (processed by T. Marke, University of Cologne), based on ERA-Interim 500 hPa and 850 hPa geopotential, covering the area around Ny Ålesund (77.25° to 81° N, 9.75° to 14.25° E) on a 0.75°x0.75° grid, provides an insight into larger scale prevailing wind directions four times per day (0, 6, 12, 18 UTC). Additionally pure cyclonic or anticyclonic conditions are identified based on shear vorticity.
Furthermore, data from manual snow profile measurements of the CO_2 concentration in the air-filled pores, snow density and dielectric properties, performed in May 2016, are employed as a rough indication of snow characteristics at the Bayelva site. Additionally, an average snow density of 0.37±0.05 gcm^{-3} in the vicinity of the EC system was obtained from gravimetrical measurements in March 2009 (Westermann et al., 2009).

4 Theoretical background and methodology

The following chapter outlines the processing steps applied to the measurement data. First of all in section 4.1 the theory behind the EC method will be illuminated. Section 4.2 then deals with its practical implementation, introducing the processing logic of the software EddyPro as well as the ogive optimization method as an alternative to the conventional EC technique. In section 4.3 a different concept to derive surface fluxes, the bulk approach, will be presented. Section 4.4 gives an overview of further processing steps applied to the final flux time series, including the definition of the study period and the detection of unusual CO_2 fluxes. Following, section 4.5 provides detailed descriptions of physical mechanisms, which might, according to the literature, cause unusually high CO_2 fluxes during the winter time. It is furthermore explained how the possible contribution of these physical drivers to the observed fluxes can be quantified.

4.1 Theoretical background of the Eddy Covariance Method

In this section the physical background as well as the mathematical principles behind the EC method are outlined, following Stull (1988) and Burba (2013).
The atmospheric boundary layer (ABL) is the lowermost part of the troposphere and thus responds rapidly to changes at the earth's surface. Through this layer mass, heat and momentum are exchanged between the surface below and the free atmosphere above. This exchange takes place in the form of fluxes and in the ABL is most effectively achieved by turbulent transport. All measurements in this study are conducted in the surface layer, that is the lowermost part of the boundary layer, where fluxes can be assumed to be constant with height. Since turbulence is the dominating transport mechanism in the ABL, the desired exchange of energy, momentum, moisture and other gases at the surface can thus be quantified by the vertical turbulent fluxes of these quantities at the measuring height.
Assuming horizontal homogeneity and stationarity, the vertical turbulent flux F can generally be expressed as the mean product of the molar concentration of dry air ρ_d in $molm^{-3}$, the

vertical wind speed w in ms^{-1} and the dry mole fraction or mixing ratio r of the gas of interest in molmol^{-1}.

$$F = \overline{\rho_d w r} \tag{4.1}$$

Reynolds decomposition is used to separate the terms into their mean ($\bar{}$) and turbulent ($'$) contributions, where the turbulent part denotes the deviation from the mean.

$$F = \overline{(\overline{\rho_d} + \rho'_d)(\bar{w} + w')(\bar{r} + r')} \tag{4.2}$$

Performing the multiplication, considering that

- the averaged deviation from the average is zero: $\overline{a'} = 0$

and assuming that

- air density fluctuations are negligible: $\rho'_d \approx 0$
- the mean vertical flow is negligible: $\bar{w} \approx 0$

leads to the following classical equation for the vertical turbulent flux, where negative flux values indicate a downward transport and positive values an upward transport of the respective quantity.

$$F = \overline{\overline{\rho_d}\bar{w}\bar{r} + \overline{\rho_d}\bar{w}r' + \overline{\rho_d}w'\bar{r} + \overline{\rho_d}w'r' + \rho'_d\bar{w}\bar{r} + \rho'_d\bar{w}r' + \rho'_d w'\bar{r} + \rho'_d w'r'} \tag{4.3}$$

$$\approx \overline{\rho_d} \overline{w'r'}$$

Based on this equation an expression is found for the sensible heat flux in Wm^{-2}

$$H = \bar{\rho} c_p \overline{w'T'}, \tag{4.4}$$

where $\bar{\rho}$ is the mass density of air in kgm^{-3}, c_p the specific heat capacity of air at a constant pressure in Jkg^{-1}K^{-1} and T the ambient temperature in K. Similarly the latent heat flux in Wm^{-2} is obtained as

$$LE = L_v \overline{\rho_d} \overline{w'r'_{H_2O}}, \tag{4.5}$$

where L_v is the latent heat of vaporization in Jmol^{-1} and r_{H_2O} the dry mole fraction of water vapor. Furthermore the CO_2 flux in molm^{-2}s^{-1} can be expressed as

$$F_{CO_2} = \overline{\rho_d} \overline{w'r'_{CO_2}}. \tag{4.6}$$

The term $\overline{a'b'}$ appearing in the flux equations is called covariance and is a measure of the degree of common relationship between the two variables a and b. The connection between covariance and turbulent flux is visualized in figure 4.1. Figure 4.1 a shows a schematic representation of the sensible heat flux in a statically unstable environment, where the temperature decreases with height (left panel) and as well as a stable environment featuring a temperature increase with height (right panel). If in the unstable case an air parcel is deflected downwards from height 1 due to a negative deviation of the vertical wind speed from its mean value, its temperature shows a negative deviation from the mean temperature at height 2. If air is transported upwards from height 1 by a positive fluctuation in w, its temperature exceeds the mean value at height 2. In both cases the covariance $\overline{w'T'}$ and hence

the sensible heat flux becomes positive, indicating an upward heat flux. On the contrary in the stable case both an upward and a downward displacement of air, result in the wind and temperature deviations having different signs. Therefore their covariance takes on a negative value, indicating a net downward transport of heat.

Figure 4.1 b demonstrates exemplarily how the net CO_2 flux is reflected in the covariance between the high-frequency time series of vertical wind speed and CO_2 concentration. In the upper plot, on many occasions, an upward (downward) moving wind, that is a positive (negative) deviation of w from its mean value, coincides with a positive (negative) deviation of the CO_2 concentration from its average. An upward moving wind therefore carries a higher CO_2 content than the downward movement, indicating a positive, that is upward directed CO_2 flux or net release of CO_2 from the soil. In the lower panel positive fluctuations in the vertical wind frequently coincide with negative fluctuations in the CO_2 concentration and vice versa. The upward moving wind therefore carries a lower CO_2 content than the downward movement, resulting in a negative covariance and hence a downward flux, indicating a CO_2 uptake by the ground.

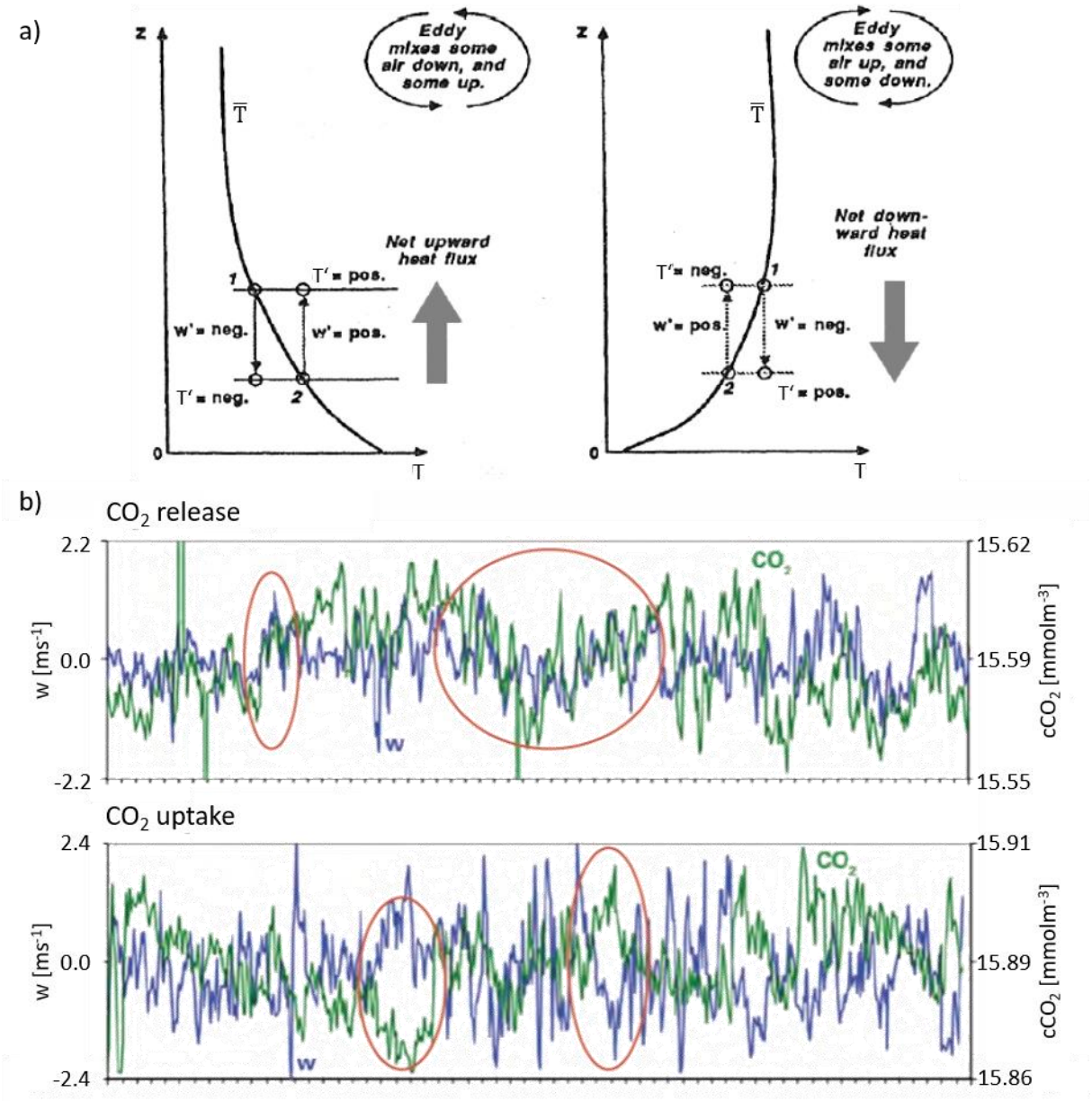

Figure 4.1: Visualization of **(a)** the covariance $\overline{w'T'}$ determining the sensible heat flux using a schematic representation (Stull, 1998) and **(b)** the covariance $\overline{w'c'_{CO_2}}$ representing the CO_2 flux with the aid of high frequency measurement time series of vertical wind speed w and molar density c_{CO_2} of CO_2 (Burba, 2013). The red ovals mark time periods with a pronounced covariance between the two time series.

The fluctuations of the wind around its mean value, as described above, arise from irregular swirls of motions, so called eddies. Their entirety is denoted as turbulence, while the relative strength of the different scale eddies defines the turbulence spectrum, as depicted in figure 4.2. This schematic illustration shows the energy distribution of turbulent eddies depending on their wavelength and frequency. On the basis of the four distinct peaks appearing in the diagram, the turbulence spectrum can be subdivided into four scales of turbulence from low to high frequencies. Next to the annual cycle there is the synoptic scale on which the change between cyclones and anticyclones takes place on a timescale of three to six days. The smaller peak next to it stands for the diurnal cycle of meteorological elements. In the area with frequencies above about 10^{-3} Hz the turbulent transport of gases and energy by sensible, latent heat and momentum flux takes place. In order to extract these desired microturbulent

fluctuations from a time series, the lower-frequency contributions thus have to be filtered out. For this purpose the conventional eddy covariance method takes advantage of the spectral gap, the region of low energy between the meso- and microturbulence scale, which reaches its minimum at a time scale of about 30 min. Longwave contributions are thus removed from a time series of high-frequency measurements by subtracting the mean value from each 30 min sub-interval. In the following the fluctuations on the microturbulent scale are referred to as turbulence.

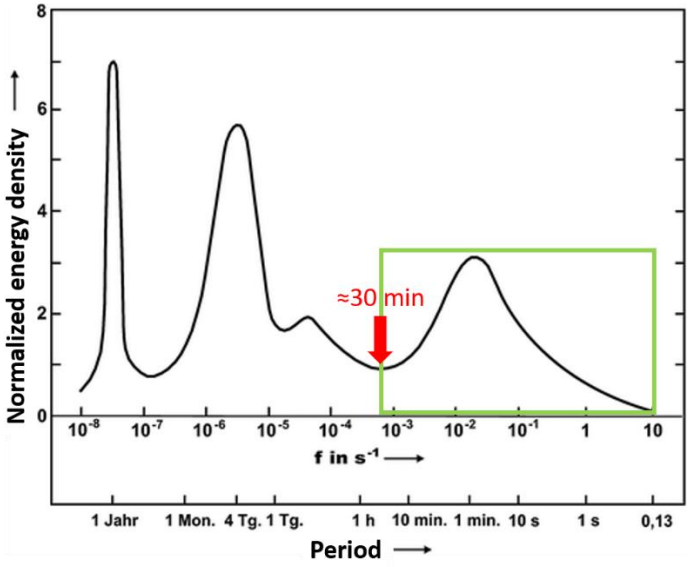

Figure 4.2: Schematic representation of the turbulence spectrum (adapted from Foken, 2016 as adapted from Roedel & Wagner, 2011). The local turbulent fluxes investigated in this study take place on the microturbulence scale (green box). The red arrow marks the spectral gap, separating the microturbulence scale from the lower-frequency contributions.

Turbulence is essentially produced by two mechanisms. On the one hand, depending on the direction of the sensible heat flux, buoyancy caused by solar heating or long-wave radiative cooling of the ground, can either produce or suppress turbulence. On the other hand wind shear generated by the frictional drag on the air flow over the surface mechanically induces turbulence. A measure of atmospheric stability in the surface layer can be derived from the relative contributions of buoyancy and wind shear to the production of turbulence.

$$L = -\frac{u_*^3}{\kappa \frac{g}{\theta_v}\left(\overline{w'\theta'_v}\right)_s} \tag{4.7}$$

This measure, called the Obukhov length is proportional to the height in m above the surface at which the buoyancy first dominates over the mechanical shear production of turbulence. Therein g is the gravitational constant, κ the von Kármán constant and θ_v the virtual potential temperature. The index s marks the surface value of the buoyancy flux. Due to the dependency of the Obukhov length on the buoyancy flux $\overline{w'\theta'_v}$ with opposite sign, $L > 0$ indicates a stable, $L \to \pm\infty$ a neutral and $L < 0$ an unstable stratification. In the results chapter of this study the surface layer scaling parameter ζ is used to determine the atmospheric stability, according to

$$\zeta = \frac{z}{L}. \tag{4.8}$$

Strictly speaking, only the sign of this parameter relates to static stability, with negative values implying unstable and positive values statically stable stratification. Nevertheless, in this study the definition by Schaller et al. (2019) is applied to distinguish between unstable ($\zeta < -0.0625$), neutral ($-0.0625 \leq \zeta \leq 0.0625$) and stable ($\zeta > 0.0625$) conditions. The friction velocity

$$u_* = \sqrt[4]{\overline{u'w'}^2 + \overline{v'w'}^2} \tag{4.9}$$

is used as a measure of the mechanical wind shear production of turbulence. From the definition of the Obukhov length follows that atmospheric stability determines the dominant driver of turbulence. Thus under the typically stable conditions during the polar night, related to the strong radiative cooling of the surface, wind shear is expected to be the main cause for turbulent transport.

However the production of turbulence is only one part of the turbulence spectrum. In order to examine the complete life time of turbulent eddies, a close-up of the microturbulent part of the spectrum (green box in figure 4.2) is depicted in figure 4.3 a. This energy spectrum can be subdivided into three sections. The energy-containing range A holds most of the turbulent energy, which is generated by buoyancy and/or wind shear in this spectral region. The resultant energy containing eddies themselves are also subject to instabilities, provoked by other eddies, which after some time makes them break up into smaller eddies. This process takes place in the inertial subrange B, where energy is neither produced nor dissipated but handed down to smaller and smaller scales. If displayed on a double-logarithmic scale, this range appears as a straight line with a slope of -5/3. Once the eddies are sufficiently small, viscosity can affect them directly. As a consequence the eddies dissipate and their kinetic energy is converted to internal energy, that is heat (C). (Kaimal & Finnigan, 1994)

Next to the kinetic energy, Fourier spectra and cospectra can be calculated for variance and covariance in order to determine the contribution to the total variance or eddy flux from each scale of motion (Figure 4.3 b). Often the frequency-weighted form of spectra and cospectra is used. The inertial subrange of the spectra then typically shows a slope of -2/3, while cospectral energy declines at a rate of -4/3. The specific behaviour of spectra and cospectra furthermore depends on the atmospheric stability in a way that from stable to unstable conditions the co(spectral) peak is shifted to a higher intensity and to lower frequencies (Stull, 1988). The cumulative summation of cospectral energy, starting from the highest frequencies is denoted as ogive and ideally converges to the final flux estimate.

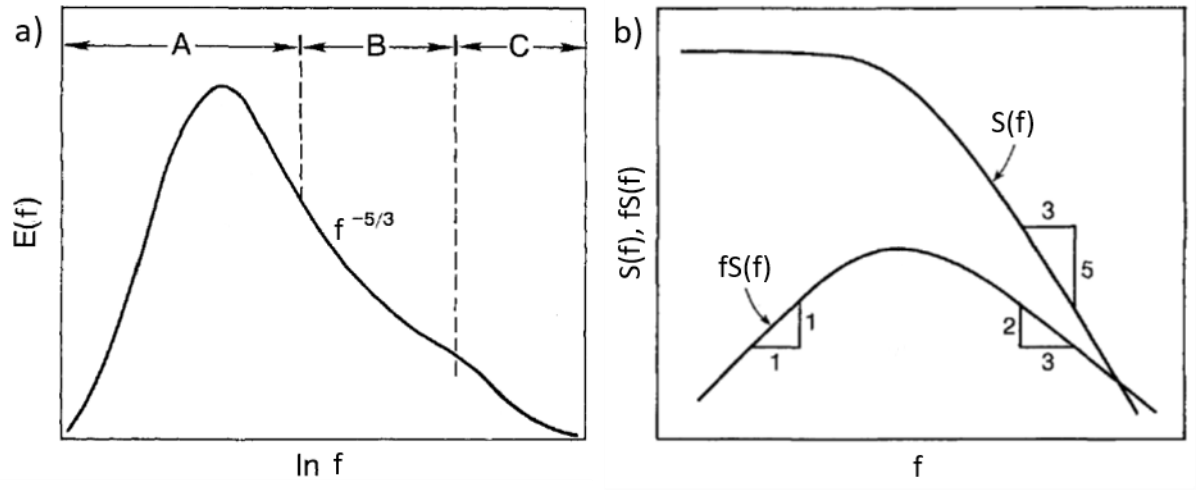

Figure 4.3: (a) Schematic illustration of energy spectrum in the ABL, showing the energy-containing range (A), the inertial subrange (B) and the dissipation range (C). E denotes the contribution to the total kinetic energy as a function of the frequency f. **(b)** Double logarithmic representations of a frequency-weighted and unweighted spectral distribution S. (Adapted from Kaimal & Finnigan, 1994)

Sensor noise exceeding the signal levels or sporadic spikes in the signal can lead to unacceptably strong noise contamination at the high-frequency end of a spectrum (Figure 4.4). This white noise usually appears as a rise in power spectral density, approaching a slope of +1 over at least one decade of the internal subrange, where the spectrum should actually be falling (Kaimal & Finnigan, 1994).

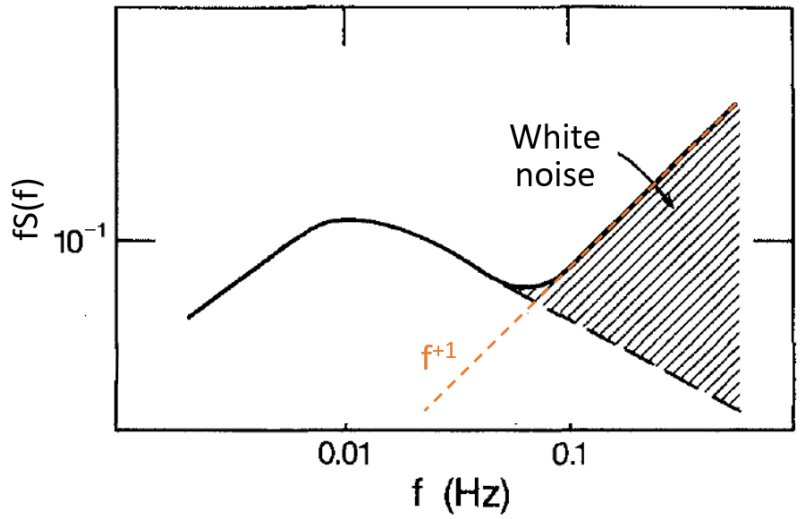

Figure 4.4: Spectrum affected by high-frequency noise with logarithmic scales on both axes (Adapted from Kaimal & Finnigan, 1994).

4.2 Practical implementation of the eddy covariance method

The first part of this section provides an overview of the processing procedure of the EC software EddyPro, including techniques for raw data screening, flux corrections as well as quality criteria and error sources. Following, an alternative to the conventional EC method as well as its implementation in the ogive optimization toolbox is presented.

4.2.1 Flux calculation and evaluation using the software EddyPro

In this study the open source software EddyPro 7 (LI-COR Inc., 2017) is employed to calculate the turbulent fluxes of gas, energy and momentum from one year of high frequency eddy covariance measurements. Following the EddyPro software instruction manual (LI-COR Inc., 2020), this chapter outlines the processing logic of the software as well as the specific settings chosen in this study for raw data handling, flux computation, correction and quality assessment of the final flux estimates.

4.2.1.1 Preliminary processing

In a first step the high frequency readings of wind components, sonic temperature, CO_2 and water vapor mass density as well as atmospheric pressure and temperature are separated into data sets of 30 minutes. Furthermore the raw data is filtered for instrument malfunctions according to the diagnostic output of anemometer and gas analyzer. The following processing procedure is performed separately for each 30 minute averaging interval.

4.2.1.1.1 Despiking and raw data statistical screening

Nine tests are performed in order to assess the statistical quality of the raw time series, following Vickers and Mahrt (1997). For each test and for each concerned variable a flag indicates whether the variable passed the test. No flux estimates are discarded on the basis of these test results but they will be used in the case studies (Section 5.6) to investigate the physical plausibility of the flux time series.

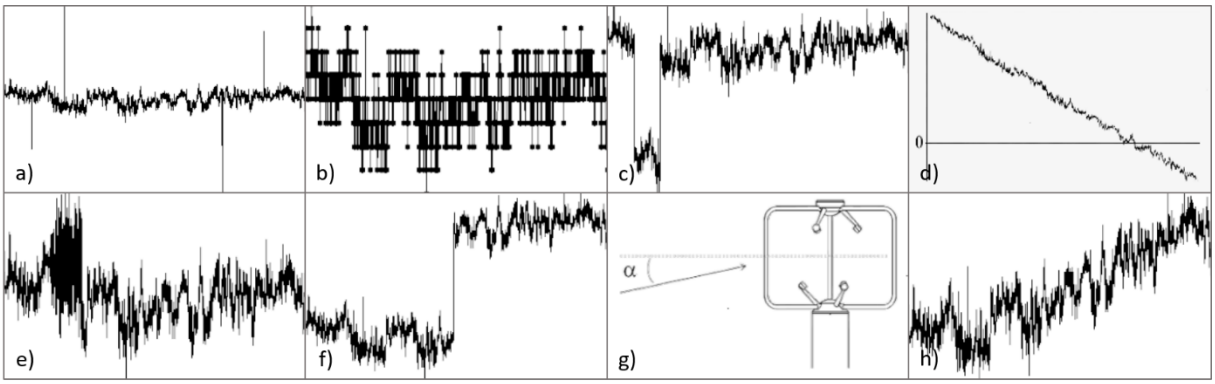

Figure 4.5: Statistical tests in EddyPro. Examples for **(a)** spikes, **(b)** a resolution problem, **(c)** a drop out, **(d)** absolute limits, **(e)** excessive skewness and kurtosis, **(f)** a discontinuity, **(g)** the Angle of Attack test and **(h)** non-stationarity of the horizontal wind. (LI-COR Inc., 2020)

A spike detection algorithm proposed by Vickers and Mahrt (1997) and based upon the paper by Højstrup (1993) is employed to detect and eliminate short-term out-ranged values in the time series. A spike is therein defined as up to three consecutive values outside of a plausibility range defined within a moving time window. A variable is hard-flagged, if for a flux averaging period, the number of spikes exceeds 1% of the number of data samples (Figure 4.5 a).

Under stable conditions, when only weak winds are present, the fluctuations of certain variables may be too small to be captured at the given amplitude resolution. A variable is hence flagged for a resolution problem, if it does not cover its typical range of variation with sufficient homogeneity. An instrument's insufficient resolution is indicated by a step ladder appearance of the time series (Figure 4.5 b).

The drop-outs test detects relatively short periods with consecutive values that are statistically different from the mean value of the averaging period. The occurrence of drop-outs may be due to a short term instrument malfunction, for example due to rain or to the obstruction of the optical or sonic path or might indicate an unresponsive instrument or electronic recording problems (Figure 4.5 c).
Values exceeding certain absolute plausibility limits are eliminated from the time series (Figure 4.5 d).
Furthermore variables are hard (soft) flagged if their skewness is lower than -2 (-1) or larger than 2 (1) or if their kurtosis is lower than 1 (2) or larger than (8) 5. Excessive skewness and kurtosis might indicate periods of instrument malfunction (Figure 4.5 e).
The goal of another test is to detect discontinuities that lead to longer term changes in the mean value. They are detected using the Haar transform (Lee et al., 2004; Mahrt, 1991; Vickers and Mahrt, 1997), which calculates the difference in some quantity over two half-window means (Figure 4.5 f).
A flux averaging period is flagged if the angle of attack α is outside of the range between -30° and 30° in more than 10 % of the time (Figure 4.5 g).
Another test assesses whether the horizontal wind undergoes a systematic change during the flux averaging period. If the relative variation of the horizontal wind between the beginning and the end of the averaging period, based on linear regression, is beyond a value of 0.5, the flux averaging period is hard-flagged for instationary horizontal wind (Figure 4.5 h).

4.2.1.1.2 Axis rotation for tilt correction

A rotation of the wind measurements into the local wind streamlines is performed in order to prevent fluxes evaluated perpendicular to the local streamlines from being affected by spurious contributions from the variance of along streamlines components.
In general a wind vector can be transformed from the sonic anemometer coordinate system x, y, z into another coordinate system x', y', z' by matrix multiplication with a rotation matrix $\boldsymbol{A}$:

$$\begin{pmatrix} u' \\ v' \\ w' \end{pmatrix} = \boldsymbol{A} \begin{pmatrix} u \\ v \\ w \end{pmatrix}. \tag{4.10}$$

In this context u', v' and w' denote the components of the wind vector after the coordinate rotation. In a 3-dimensional coordinate system the full coordinate transformation can be divided into three rotations around the three axes of the coordinate system x, y, z (Figure 4.13). These rotations can be described by three rotation matrices $\boldsymbol{B}$, $\boldsymbol{C}$, $\boldsymbol{D}$ and three angles γ, β, α, where

$$\boldsymbol{A} = \boldsymbol{BCD} \tag{4.11}$$

with

$$\boldsymbol{B} = \begin{pmatrix} cos(\gamma) & -sin(\gamma) & 0 \\ sin(\gamma) & cos(\gamma) & 0 \\ 0 & 0 & 1 \end{pmatrix}, \tag{4.12}$$

$$\boldsymbol{C} = \begin{pmatrix} 1 & 0 & 0 \\ 0 & cos(\beta) & -\sin(\beta) \\ 0 & \sin(\beta) & \cos(\beta) \end{pmatrix}, \tag{4.13}$$

$$\boldsymbol{D} = \begin{pmatrix} cos(\alpha) & 0 & \sin(\alpha) \\ 0 & 1 & 0 \\ -\sin(\alpha) & 0 & \cos(\alpha) \end{pmatrix}. \tag{4.14}$$

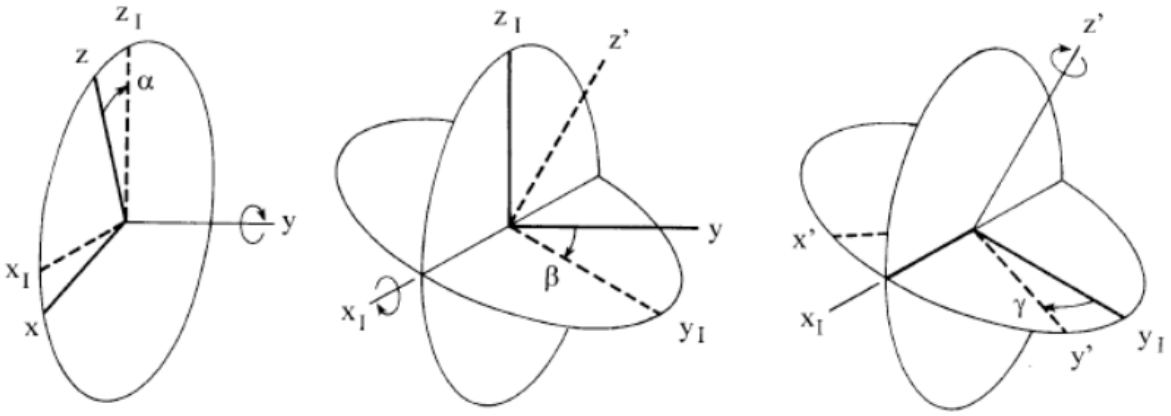

Figure 4.6: Definitions of the tilt angles α, β and γ. The original axes are x, y, z and the final axes are x', y', z'. x_I, y_I, z_I are intermediate axes. (Wilczak et al., 2001)

Two different methods to determine the rotation angles are compared in this study. Both methods intend to nullify the mean vertical wind velocity $\overline{w}$ in order to meet a basic assumption of the eddy covariance technique, but on a different time scale.

The double rotation method (Kaimal & Finnigan, 1994) consists of two rotations of the coordinate system, performed for each flux averaging period. First the coordinate system is rotated around its z-axis into the mean wind, so that the mean cross-stream wind component is nullified $\bar{v} = 0$ with $\gamma = tan^{-1}\left(\frac{\bar{v}}{\bar{u}}\right)$ and a second rotation around the new y-axis nullifies the mean vertical wind component $\overline{w} = 0$ with $\alpha = tan^{-1}\left(\frac{\overline{w}_I}{\overline{u}_I}\right)$.

The planar fit method (Wilczak et al., 2001) on the other hand is the preferred choice for sites with complex or sloping topography, which might result in a mean vertical wind component actually differing from zero (Lee et al., 2004). In this case the anemometer tilt with respect to longer term (days to weeks) local streamlines is assessed by fitting a plane to the actual measurements of the average vertical wind component $\overline{w}_m$, as a function of the horizontal components, $\bar{u}_m$ and $\bar{v}_m$. This is based on the rationale that if the anemometer is tilted with respect to the local streamlines, a certain amount of the horizontal wind speed will be found in the measured vertical component $\overline{w}_m$, so that the latter can be expressed as a linear combination of the horizontal wind components:

$$\overline{w}_m = b_0 + b_1\bar{u}_m + b_2\bar{v}_m. \tag{4.15}$$

By means of a multiplication of the measured wind vector with the rotation matrix $\boldsymbol{P} = \boldsymbol{D^T C^T}$, the coordinate system is rotated around its y-axis by the angle α and around the resulting x_I-axis by an angle β. Thereby the z-axis is placed perpendicular to the plane of the local streamlines so that the long-term mean of the vertical wind component $\overline{w}$ is nullified (Figure 4.6). The rotation angels α and β result from the fitting parameters b_0, b_1 and b_2, which are determined via bilinear regression, with

$$\sin(\alpha) = \frac{-b_1}{\sqrt{b_1^2 + b_2^2 + 1}}, \tag{4.16}$$

$$\cos(\alpha) = \frac{\sqrt{b_2^2 + 1}}{\sqrt{b_1^2 + b_2^2 + 1}}, \tag{4.17}$$

$$\sin(\beta) = \frac{b_2}{\sqrt{b_2^2 + 1}}, \tag{4.18}$$

$$\cos(\beta) = \frac{1}{\sqrt{b_2^2 + 1}}. \tag{4.19}$$

A third rotation around the z'-axis by the angle γ, similar to the first rotation of the double rotation method, aligns the wind vector with the mean wind direction.

For the calculation of the one year flux time series, the more robust double rotation method is applied in order to reduce the processing time and to improve the comparability of the flux estimates since no further setting options are available, which might influence the performance of this coordinate rotation. However, given the sloping terrain and the complex topography of the study site (Section 3.1) a better performance is generally expected from the planar fit method. Fluxes resulting from either of the two rotation methods are thus compared in the case studies in section 5.6. The specific performance of the planar fit method at the study site is furthermore outlined exemplarily in appendix A.1.

4.2.1.1.3 Extracting turbulent fluctuations

Next, the turbulent fluctuations need to be extracted from the time series. Therefore block averaging, which is also called Reynolds averaging, is applied, where the mean value of a variable is subtracted from each averaging period, leaving the turbulent fluctuations as individual departures from the mean.

4.2.1.1.4 Time lag compensation

Due to the physical distance between anemometer and gas analyser, the wind field takes some time to travel from one instrument to the other. This results in a certain delay between the moments the same air parcel is sampled by the two sensors. A mismatch between the measured time series is induced, which needs to be compensated. Due to the variability in wind regimes usually an automatic time lag detection via covariance maximization is applied instead of assuming a constant delay time. This procedure determines the time lag which maximizes the covariance of two variables within a window of plausible time lags. These limits can either be defined by the user or calculated automatically by the software. In this study the "Covariance maximization with default" option is used, which implies, that if a covariance maximum is not attained within the plausibility window, a default value is used, either taken as the user-defined expected time lag or automatically calculated by EddyPro.

4.2.1.2. Flux calculation and correction

Before actually calculating the flux estimates, some key average ambient variables such as air temperature, pressure, and molar volume, average concentrations expressed as mole fractions, mixing ratios and average molar densities as well as additional micrometeorological parameters are evaluated. Next, uncorrected gas, energy and momentum fluxes are calculated according to equations 4.4 to 4.6. The following corrections are then applied to the raw flux estimates in order to derive the final fluxes.

4.2.1.2.1 Correction of gas fluxes for air density fluctuations

Eddy covariance measurements intent to capture fluxes associated with the ecosystem removing or adding gas from and into the air flow above it. If gas concentrations are measured in terms of density, other processes inducing additional changes in gas density, namely thermal and pressure expansions and contractions as well as water dilution, thus need to be eliminated. This is achieved by applying the WPL-correction by Webb et al. (1980)

$$F_{CO_2,WPL}=F_{CO_2,0}+\frac{\mu}{1+\mu\frac{\overline{\rho_v}}{\overline{\rho_d}}}\frac{\overline{c_{CO_2}}}{\overline{\rho_d}}E+\frac{\overline{c_{CO_2}}}{\bar{\rho}c_p\bar{T}}H+\left(1+\mu\frac{\overline{\rho_v}}{\overline{\rho_d}}\right)\frac{\overline{c_{CO_2}}}{\bar{p}}\overline{w'p'}$$

Raw CO_2 flux | Water dilution | Thermal expansion | Pressure expansion

WPL density terms

,

where $F_{CO_2,WPL}$ denotes the CO_2 flux after the WPL correction in mmolm^{-2}s^{-1} , $F_{CO_2,0}$ the raw covariance using fast CO_2 molar density measurements c_{CO_2} in mmolm^{-3} as measured by the gas analyzer, $\mu = 1.6077$ is the ratio of molar masses of air and water, E the water vapor flux in kgm^{-2}s^{-1} , ρ_v the water vapor density and p the atmospheric pressure in Pa.

When H and LE have the same magnitude, H affects $F_{CO_2,WPL}$ about five times as much as LE (Webb et al., 1980). The greater the mean concentration of a constituent compared to its turbulent fluctuations, the greater is the required relative flux correction. In the case of CO_2, the magnitude of the WPL-terms commonly exceeds that of the CO_2 flux itself (Webb et al., 1980).

Although the influence of pressure fluctuations is usually neglected, it was shown to introduce a small positive bias to the CO_2 fluxes, which may become significant during high wind speeds, at high elevations, in complex terrains, in ecosystems with very small fluxes and when integrated over long periods (Burba, 2013; Zhang et al., 2011; Massman & Lee, 2002).

4.2.1.2.2 Instrument surface heating correction

If the open-path gas analyzer model LI-7500 or LI-7500A/RS is operated in summer configuration, self-heating of the instrument might induce a temperature difference between the ambient air and the air inside the measurement path. This results in an additional sensible heat flux inside the path to the one calculated from the CSAT measurements in the ambient air. Since this additional sensible heat flux is not taken into account when correcting for

density fluctuations via the WPL correction, this might lead to erroneous latent heat and CO_2 flux estimates. The additional sensible heat flux in the path can either be calculated from in-path fast temperature measurements or quantified based on estimates of the temperature difference between instrument surface temperatures and air temperatures. For the latter slow surface temperatures of the instrument top, bottom and spar are estimated and related either to air temperature via linear regression or to air temperature, global radiation, longwave radiation and wind speed via multiple regression. Regression parameters can either be user-defined or the default values obtained in field studies by Burba et al. (2008) can be applied.

There are several reasons that led to the decision not to apply this correction in this. First of all precautions have been taken to reduce or eliminate the influence of instrument self-heating, including a 45° tilt of the gas analyzer from the vertical and operating the gas analyzer in the winter configuration, allowing for a 5 to 20 times reduction in surface heating (Burba, 2013). Since no in-path temperature measurements have been performed and no experiments were conducted to determine the site-specific instrument surface temperature, the only option to account for instrument self-heating is to estimate the additional sensible heat flux using the default regression parameters proposed by Burba et al. 2008. This might be subject to considerable uncertainties, particularly because the default values refer to a vertically mounted sensor. Furthermore Lüers et al. 2014 found that the correction method proposed by Burba et al. (2008) yields flux values which amount to an unrealistically high annual carbon budget for the Bayelva site between 2008 and 2009.

Typically the impact of the correction is small, with additional in-path sensible heat fluxes of between 15 and 20 Wm^{-2}, resulting in a heat correction term of 0.68 to 0.91 $\mu molm^{-2}s^{-1}$ at most (Burba, 2013). However in an area with extremely low, near-zero fluxes, like the Bayelva site, any bias significantly affects the cumulative results, and should be corrected. Therefore and because several studies found that the correction efficiently removes inexplicable off-season CO_2 uptake and achieves a good agreement with closed-path and chamber measurements (Kittler et al., 2017; Oechel et al., 2014; Ono & Yamada, 2007), the effect of the correction is quantified and discussed in the case studies in section 5.6.

4.2.1.2.3 Correction for high-frequency and low-frequency spectral attenuations

Two distinct effects might result in a flux underestimation by the eddy covariance method, which needs to be compensated via spectral corrections.

Block averaging over a 30 minute time window leads to an attenuation of flux contributions in the frequency range close to the (inverse of the) flux averaging interval. This loss of longer-term turbulent flux contributions is corrected by applying a high-pass filtering correction proposed by Moncrieff et al. (2004).

At the same time instrument capacities limit the temporal and spatial resolution of small eddies, resulting in a dampening of the high-frequency turbulent fluctuations. This loss is compensated by applying a low-pass filtering correction following Moncrieff et al. (1997).

The spectral correction procedure comprises the following steps. First of all an ideal flux cospectrum is calculated. Second the high- and low-pass filtering properties of the actual

measuring system, averaging period and detrending method are determined. Third the flux attenuations are estimated and in a fourth step used to calculate the spectral correction factors and to finally perform the correction. (LI-COR Inc., 2020)

4.2.1.3 Quality assessment

Given the manifold sources of uncertainty to the EC method, a thorough quality assessment of the final flux estimates is indispensable. In this study an overall flagging system introduced by Mauder and Foken (2004) is applied to give a first overview of the usability of the calculation results. In the case studies (section 5.6) the individual flux estimates are then inspected for physical plausibility in more detail. Additionally the random uncertainty introduced by sampling errors is taken into account to further evaluate the reliability of the data.

4.2.1.3.1 Overall flagging system

The main objective of assessing the data quality is to determine if the simplifications assumed in the EC method (Section 4.1), are justified under the given micrometeorological conditions. The steady state test and the integral turbulence characteristics (ITC) test are therefore used to evaluate the assumptions of stationarity and fully developed turbulent conditions (Foken et al., 2004; Foken & Wichura, 1996; Göckede et al., 2008).

For the steady state test the covariances for each whole 30 minute averaging period are compared to the averaged covariances during subsets of 5 minutes. The flux quality is determined based on the deviation of the two covariances. A time series is considered to be in steady state if the difference is lower than 30 %.

The ITC test compares the measured ratio of the standard deviation of a turbulent parameter and its turbulent flux to a modelled one. This parameterization is based on the flux-variance similarity, meaning that the ratio is nearly constant or a function for example of the stability. The test is performed for both parameters involved in the covariance. Again the flux quality is evaluated based on the deviation of measurement and model result. At a difference of less than 30 % a well-developed turbulence can be assumed.

The results from both quality tests are combined into a unique overall flag following the flagging policy after Mauder and Foken (2004) (Table 4.1). A flag of 0 denotes high quality data that can be used for fundamental research such as process studies, a value of 1 is attained for moderate quality data, suitable for general analysis such as long term observations and annual budgets, whereas data flagged 2 should be discarded from the time series.

Table 4.1: Overall flagging system after Mauder and Foken (2004).

Stead state test deviation range [%]	ITC test deviation range [%]	Final flag
0 - 30	0 – 30	0
≤ 100	≤ 100	1
≥ 101	≥ 101	2

4.2.1.3.2 Detailed quality assessment

A more detailed quality assessment is performed in the framework of case studies in section 5.6. CO_2 fluxes are hard or soft flagged according to overall FCO_2 flags of 1 or 2, respectively. Moreover the results from steady state and ITC test are considered separately with soft flags denoting deviations of more than 30 % and hard flags marking deviations exceeding 100 %. In addition to the CO_2 fluxes, these flags are also listed for the sensible and latent heat flux due to the possible error propagation from the energy fluxes to the CO_2 fluxes via the WPL correction. Furthermore to ensure sufficient turbulent mixing near the surface, averaging intervals with a friction velocity smaller than 0.1 ms^{-1} are hard flagged. Also considered as low-quality are fluxes during averaging intervals where wind directions between 15 and 55 ° might lead to a flow distortion by the upwind tower structure. Hard or soft flags are furthermore assigned when the CO_2 signal strength drops below 93 or 73, respectively, indicating an obstruction of the optical path, for example by dirt or precipitation. The thresholds were determined visually from the behaviour of CO_2 fluxes as a function of CO_2 signal strength. Although instrument malfunctions are already filtered out from the raw data, time periods between one hour before and one day after liquid precipitation was recorded and between one hour before and one hour after maintenance works were carried out at the station are furthermore checked for unphysical outliers exceeding the 10^{th} or the 90^{th} percentile of the flux time series. Additionally the raw data flags resulting from the spike count and statistical tests (section 4.2.1.1.1) are considered. From the whole one-year time series a filtered time series is obtained by applying the most common quality criteria. This filtering includes the exclusion of fluxes with an overall FCO_2 flag of 2, times where the friction velocity or the wind direction are outside their specified limits, unphysical fluxes during precipitation events and maintenance works as well as fluxes hard-flagged for a low CO_2 signal strength. Due to these filtering steps 54 % of the CO_2 fluxes are discarded from the original time series. The effects of the individual filtering steps are listed in section 5.3.

4.2.1.3.3. Flux random uncertainty due to sampling error

Including a careful choice of the study site and the instrument setup and orientation as well as flux corrections and a detailed quality assessment, many efforts are made to eliminate the major sources of error affecting the EC technique. In this study the method of Finkelstein and Sims (2001) is applied to additionally estimate the random uncertainty due to sampling errors as the variance of the EC measurement, that is the variance of the covariance. The error bars shown in some figures of chapter 5 are based on these estimates since to my knowledge currently no straight-forward error propagation rules exist for EC fluxes. Nevertheless these estimates only cover one source of error and should therefore not be interpreted as being representative for the total flux uncertainty.

4.2.2 Ogive Optimization

As outlined in section 4.1 the conventional EC method is based on the assumption of a clear and fixed spectral gap separating the turbulent scale from lower-frequency contributions. Figure 4.7 reveals limitations of this approach. In the ideal case, represented by figures A and

B, the turbulent and low-frequency contributions are clearly separated by the spectral gap allowing to isolate the former simply by choosing an appropriate averaging time T_1 of about 30 min and using fast response instruments recording at a frequency T_2 of 20 Hz in our case. The related ogive can thus be found to converge to a stable flux estimate within the averaging interval. In this case the conventional EC method perfectly extracts the turbulent flux from a time series. In the typical case (Figures C and D) the existence of a spectral gap is unclear. There are overlapping contributions from low-frequency motions and turbulence as well as site and instrument-specific non-white noise and dampening. The arising flux errors when applying the EC method with a fixed averaging interval are typically still assumed to be negligible and the low-pass filtering correction, described in section 4.2.1.2.3 may furthermore reduce instrument-specific non-white noise and/or dampening. In the third case (Figures E and F) there is an excessive low-frequency influence relative to the turbulent contribution. Adjusting the averaging interval is not sufficient anymore to separate the severely overlapping high- and low-frequency contributions. The resultant ogive either converges to an extremum or diverges, depending on the direction of the low-frequency fluxes.

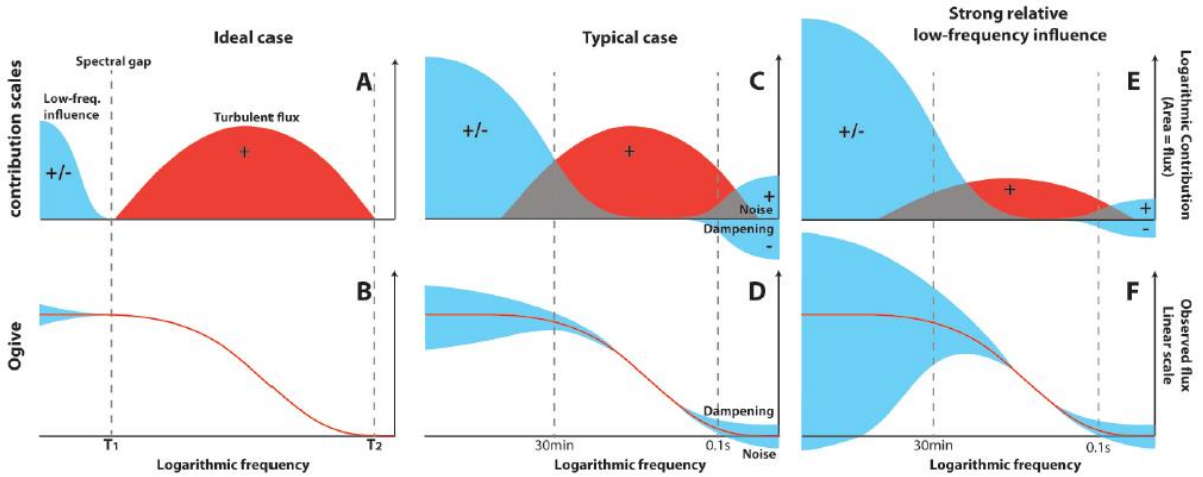

Figure 4.7: (top row) Cospectra and **(bottom row)** ogives during typical observational situations. The respective turbulent fluxes are shown in red and the low-frequency, noise and dampening components in blue. (Sievers et al., 2015)

The above examples show how low-frequency influence can affect our ability to capture high-frequency turbulent fluxes. However the severity of this problem still depends on the desired type of application of the EC method. On the one hand, in long-term net ecosystem-exchange studies flux estimates are understood to be site-specific, applying only for the unique conditions of a particular ecosystem. In this kind of studies low-frequency contributions, which are characteristic for the study site, may be included, also in order to achieve a closure in energy and carbon-balance. Process-oriented studies on the other hand search for local biogeochemical processes causing the observed fluxes. In order to qualify these fluxes for up-scaling through numerical modelling, low-frequency fluctuations associated with larger-scale phenomena like topographical forcing, gravity waves, deep convection and large roll vortices need to be excluded and only the locally meaningful turbulent fluxes should be retained.

This study searches for universal drivers of the CO_2 exchange in a low-flux environment where any low-frequency contribution can significantly affect the final flux estimate and at a site where low-frequency forcing is likely to be caused by the surrounding topography. All of this renders it crucial to assess the uncertainty introduced by low-frequency influences when using the conventional EC method and to filter out these contributions if necessary.

For this purpose the ogive optimization method proposed by Sievers et al. (2015) (version 1.01.00, toolbox publicly available through the Mathworks file exchange) is applied. In contrast to the conventional EC logic, this method assumes a dynamic spectral gap between often overlapping spectral flux contributions. Its processing procedure is explained with the aid of an exemplary output for a 60 min observation of sensible heat flux (Figure 4.8). In order to find the optimal combination of data set length and detrending interval to separate turbulent and low-frequency flux contributions, first of all a density map of 14 000 ogives is generated by varying the averaging interval as well as the running mean window used for detrending. Next, a copectral distribution model is fitted to the density map to identify the most likely flux estimate. In this example of a sensible heat flux, consistent with the near absence of low-frequency contributions, a strong consistency appears between the ogive density patter, the 30 min linearly detrended as well as the modelled ogive. Under these conditions the conventional approach thus suffices to obtain a reliable flux estimate. Only the haze around the final ogive shows that a small part of permutations states are affected by low-frequency motions, also visible in the cospectrum.

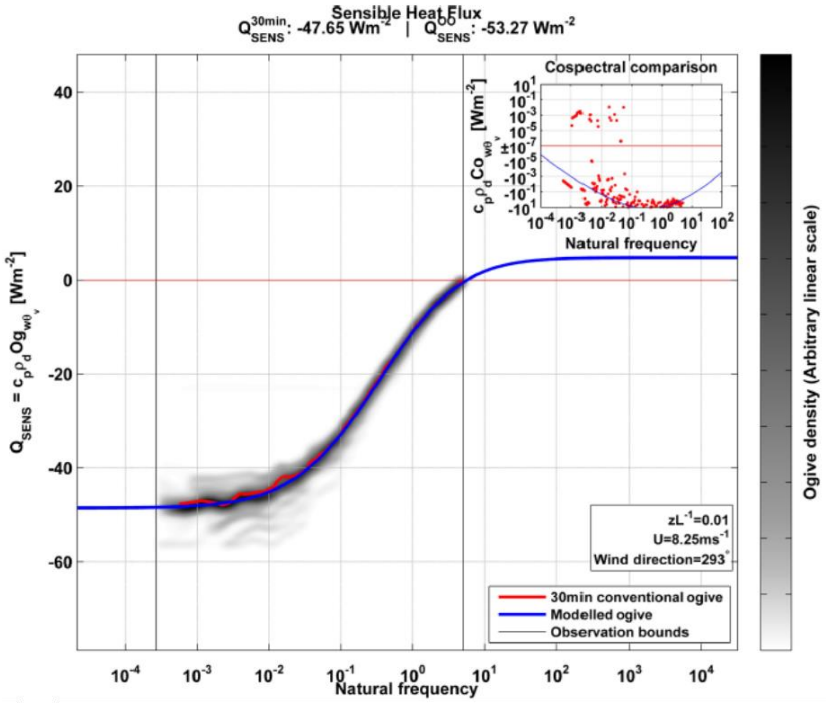

Figure 4.8: Example for a 60 min observation of sensible heat flux. The main figure depicts the ogive density (gray shading), the modelled ogive (blue line) and the standard 30 min linear detrended ogive (red line). The corresponding cospectra of the modelled ogive and the conventional 30 min observation are shown in the inner figure. (Sievers et al., 2015)

Further deviations of the ogive optimization toolbox (OOT) from the flux computation with EddyPro include the use of linear detrending instead of block averaging. Furthermore the OOT

automatically determines time lags based on wind regimes and the specific geometry of the eddy covariance system. From the documentation of the OOT the type of coordination implemented in the toolbox could not be determined.

4.3 Bulk transfer method

In this study the bulk transfer method is used to obtain an independent estimate of the surface energy fluxes in order to validate the results from the EC method. Following Stull (1988) a vertical flux F_ξ of any quantity ξ is assumed to be driven by the vertical change in ξ. In the following, fluxes are calculated between the surface (subscript $surf$) and the measuring height h_m (subscript a), relating the vertical gradient of the desired quantity to the turbulence structure in the surface layer, using

$$F_\xi = -U_T\left(\overline{\xi_a} - \overline{\xi_{surf}}\right). \tag{4.20}$$

$$U_T = D_{(n,s,u)} \cdot \overline{u_a} \tag{4.21}$$

represents the transport velocity as a function of the mean horizontal wind velocity $\overline{u_a}$ at the measuring height and the bulk transfer coefficient D for neutral (n), stable (s) or unstable (u) conditions. Following Price and Dunne (1976), from the general formulation, expressions can be derived for the sensible heat flux

$$H = -\rho c_p D_{H(n,s,u)}\left(T_a - T_{surf}\right) \tag{4.22}$$

as well as for the latent heat flux

$$LE = -\rho_d L_{(v,s)} D_{LE(n,s,u)} \frac{0.622}{p}\left(e_a - e_{surf}\right), \tag{4.23}$$

where $L_{(v,s)}$ refers to the latent heat of vaporization ($LE < 0$ and $T_s = 0\ °C$) or sublimation ($LE < 0$ or $T_s < 0\ °C$), p to the atmospheric pressure, e_a to the water vapor pressure at the measurement height and e_s to the ice saturated vapor pressure over a cold snowpack ($T_s < 0\ °C$) or water saturated vapor pressure over a melting snowpack ($T_a = 0\ °C$). The surface temperature is calculated from the longwave radiation measurements according to

$$T_{surf} = \sqrt[4]{\frac{LW_{out} - (1-\varepsilon)LW_{in}}{\varepsilon\sigma}}, \tag{4.24}$$

where $LW_{out,in}$ denote the outgoing and incoming longwave radiation and σ is the Stefan-Boltzmann constant. The emissivity is set to 0.99 for the snow covered surface (e.g. Rees, 1993; Bussières, 2002).

It is usually assumed that

$$D_{H(n,s,u)} = D_{LE(n,s,u)} = \frac{\kappa^2}{ln\left(\frac{h_m}{z_0}\right)^2} \cdot \psi_{(n,s,u)}, \tag{4.25}$$

where κ denotes the von Kármán constant and z_0 the roughness length, that is the height at the bottom of the logarithmic wind profile where the wind speed is zero. Furthermore

$$\psi_n = 1, \tag{4.26}$$

$$\psi_s = \frac{1}{1 + 10R_i}, \tag{4.27}$$

$$\psi_u = 1 - 10R_i, \tag{4.28}$$

with the bulk Richardson number

$$R_i = \frac{g\Delta z\left(T_a - T_{surf}\right)}{u_a^2 T_a}, \tag{4.29}$$

where g represents the gravitational acceleration and Δz the distance between the snow surface and the measuring height.

4.4 Further processing of the resultant flux time series

The following section deals with the post-processing of the final data set. First of all the choice of the study period and its extraction from the whole one-year time series are explained. The second subsection thereafter presents the procedure of identifying events of unusually high CO_2 fluxes in the time series.

4.4.1 Definition of the study period

This study focuses on the time period of 2015, where the influence of CO_2 uptake by the ground due to photosynthesis can be assumed to be negligible. The aim is to reduce the complexity of the large amount of interacting processes by eliminating one major driver of CO_2 fluxes. This narrows down the wide range of possible mechanisms that could explain the observed flux events. Furthermore the exclusion of the CO_2 uptake during the summer month at the same time largely eliminates the seasonal trend as well as the diurnal cycle from the time series. The detection of events of unusually high CO_2 fluxes is therefore facilitated since they are less obscured by fluctuations on other time scales.

The time period where the CO_2 exchange is dominated by photosynthesis is herein defined as the summer time where the running monthly mean of the CO_2 fluxes constantly stays below zero (Figure 4.9). This classification is based on the filtered time series (section 4.2.1.3.2) in order to avoid an influence of unphysical flux values. As a result the study period is limited to the time from the beginning of 2015 to 10 June 2015 and from 12 September 2015 until the end of 2015. It starts during the polar night, which lasts until 17 February 2015. At the time where photosynthesis gains importance due to increasing solar radiation, the ground is still snow covered. The snow free period continues beyond the date where the CO_2 uptake by the vegetation is back to a minimum. Shortly after the beginning of the time with constant snow cover on 16 October 2015, the sun finally stays below the horizon after 25 October 2015.

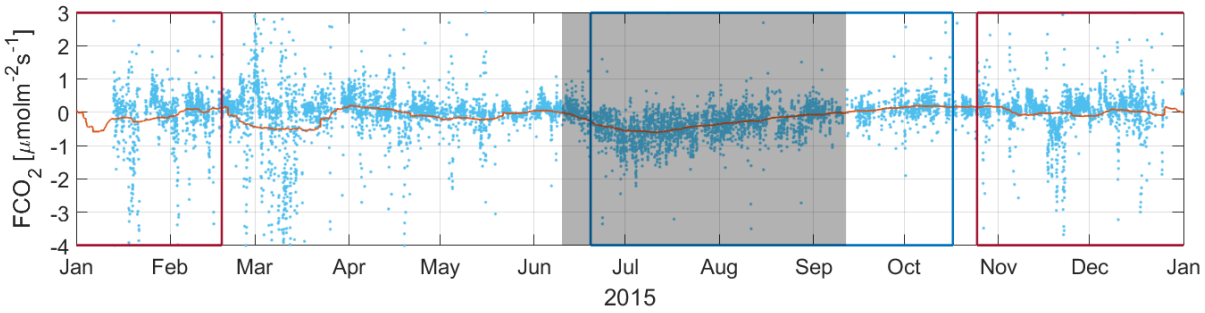

Figure 4.9: Definition of the study period based on a running monthly mean of the CO_2 flux time series. The chart is limited to the range between -4 and 3 µmolm^{-2}s^{-1} for reasons of clarity.

4.4.2 Event detection

Following Schaller et al. (2019) a median absolute deviation (MAD) test (Mauder et al., 2013) is applied to detect periods of outranged CO_2 fluxes in the data set. This test detects values x_i in the time series whose deviation from the previous and the next value

$$d_i = (x_i - x_{i-1}) - (x_{i+1} - x_i) \tag{4.30}$$

exceeds the following limits

$$\langle d \rangle - \frac{q \cdot MAD}{0.6745} \leq d_i \leq \langle d \rangle + \frac{q \cdot MAD}{0.6745}, \tag{4.31}$$

where $\langle d \rangle$ denotes the median of all double differenced values d_i and

$$MAD = \langle |d_i - \langle d \rangle| \rangle. \tag{4.32}$$

If at least two consecutive values d_i exceed the range given in equation (4.31), the corresponding fluxes x_i are labelled as an event. By defining a minimum duration for the event, it is avoided that a sequence of high-frequency spikes, which sometimes pass the raw data spike detection, are misinterpreted as an event. The threshold value of $q = 4$ was found to be suitable to reliably separate events from periods with a regular CO_2 exchange. Since, equivalent to the findings of Schaller et al. (2019), the MAD test is not always able to capture the whole event, detected events are extended to both sides until the CO_2 flux changes sign. Subsequently events consisting of excessively large and irregular spikes were removed and some smaller events were manually added based on a visual inspection of the time series. An example for the event detection is given in figure 4.10. In the following the detected time periods of unusually high absolute CO_2 fluxes are referred to as events while the individual fluxes during the events are denoted as positive and negative event fluxes, respectively.

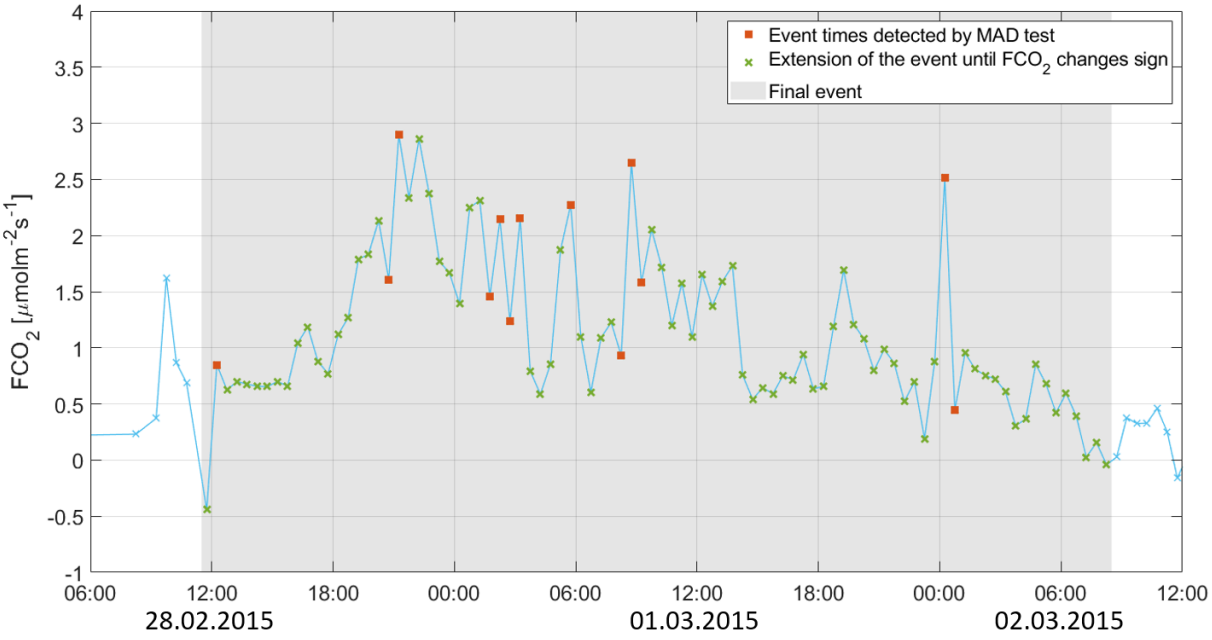

Figure 4.10: Example for the detection of CO_2 flux events based on the MAD test and an extension of the identified time periods.

4.5 Estimation of physical mechanisms proposed in the literature

The winter time events in the CO_2 fluxes can most likely not be explained by the biotic processes usually assumed to be the most important drivers of CO_2 exchange. Vascular plants were found to photosynthesize until below -3 °C under the snow cover (Bate and Smith, 1983) and lichens and mosses even below -10 °C (Sveinbjörnsson and Oechel, 1981; Walton and Doake, 1987; Kappen, 1993). Nonetheless the influence of photosynthesis by plants and snow algae can most likely be excluded as a cause for CO_2 uptake events, particularly during the dark polar night (Pirk et al., 2017). At the same time the observed short-time outbursts of CO_2 exceed a magnitude that could possibly be related to an instantaneous release of CO_2 produced by microbial respiration. It can therefore be speculated that the unusually high CO_2 fluxes are instead caused by abiotic mechanisms, such as convective or advective gas transport below the measurement height or inside the snow pack or thermo-physical processes like the solution of CO_2 in water (Pirk et al., 2017).

In the following sections these mechanisms will be explained in detail and approaches will be presented to estimate their possible contributions to the observed fluxes.

4.5.1 Pressure pumping

During the entire study period the soil temperature at the Bayelva site stayed above the minimum temperatures of between -10 °C and -20 °C reported for soil respiration (Mikan et al., 2002; Elberling & Brandt, 2003). Therefore throughout the winter CO_2 is released from the soil into the snow pack, which acts as a storage layer, delaying the CO_2 exchange between soil and atmosphere (Lüers et al., 2014; Graham & Risk, 2018). Accordingly a CO_2 concentration gradient forms within the snow pack, with concentrations decreasing with distance from the soil (Graham & Risk, 2018). This slow but constant vertical transport of CO_2 away from its source of production is achieved via diffusion (Seok et al., 2009). Ice crusts on top of the snow cover could reduce or prevent diffusive CO_2 emission to the atmosphere and trap relatively

high concentrations within the snowpack (Jones et al., 1999). If there is a strong enough decrease in temperature between the soil and the snow surface, CO_2 can be released to the atmosphere by thermal convection (Powers et al., 1985; Sturm, 1991; Sturm & Johnson, 1991). While under calm conditions diffusion is the major transport mechanism of CO_2 in the snow pack, there is growing evidence that advective transport is responsible for large, episodic CO_2 emissions (Jones et al., 1999; Takagi et al., 2005; Massman & Frank, 2006; Sievers et al, 2015; Laemmel et al., 2017; Graham & Risk, 2018). This is consistent with findings of a strong negative correlation between wind speed and CO_2 concentration inside the snow pack (Takagi et al., 2005; Graham & Risk, 2018). This advective gas transport is caused by the ventilation of porous media like the snow pack or to a lesser extent also the less permeable soil. Atmospheric air is mixed into the soil or snow pores, replacing the CO_2-enriched air, which is in exchange released to the atmosphere (Graham & Risk, 2018). This phenomenon is often referred to as wind or pressure pumping and is caused by different meteorological mechanisms acting on various time scales (Graham & Risk, 2018). At the low-frequency end, barometric pumping is driven by rapid changes in air pressure, associated with the passage of frontal systems. These large scale pressure fluctuations cause the air to alternately expand and contract, making it move very slowly in and out of the snow cover (Clements & Wilkening, 1974; Colbeck, 1989; Cunningham & Waddington, 1993). Next to synoptic weather systems, pressure fields can be induced through the interaction of the wind flow with the local aerodynamic roughness elements like nearby mountains and snow drifts (Jones et al., 1999; Massman & Frank, 2006). This process, known as topographic pumping, can likewise initiate air currents within the snow cover (Colbeck, 1989). At high-frequency time scales of seconds to minutes, turbulent pumping is caused by fast pressure fluctuations (Massman et al., 1995) associated with turbulent eddies, which are generated by the wind flow over the snow-covered surface (Massman et al., 1995, 1997; Clarke et al., 1987; Clarke & Waddington, 1991). These small scale pressure fluctuations were found to increase exponentially with wind speed (Colbeck, 1989). Therefore in an open landscape like the Bayelva catchment, which is exposed to pressure variations on all of these time scales as well as to direct ventilation of the snow pack at high wind speeds (Hirsch et al., 2004; Novak et al., 2000), it is particularly challenging to separate the influences of different atmospheric drivers. Generally, the lower the frequency of the forcing and thus of the air pressure fluctuations, the deeper their penetration into the ground (Auer et al., 1996; Massman, 2006; Laemmel et al., 2017). Some speculate that pressure pumping can in turn also intiate an uptake of CO_2 into the snow cover, especially when the snow pores are filled with CO_2-depleted air after an event of advective CO_2 emission from the ground (Lüers et al., 2014; Pirk et al., 2017; Graham & Risk, 2018). The refilling of the storage following a strong CO_2 emission would also initially supress diffusive transport to the atmosphere (Graham & Risk, 2018).

Generally the climatic and topographical conditions render it very likely that pressure pumping affects the CO_2 exchange at the Bayelva site. Therefore an attempt has to be made to quantify the potential of this phenomenon to explain the observed events of unusually high CO_2 fluxes. The strength of soil or snow ventilation depends on many parameters like the wind speed above the surface as well as inside the ground, the wavelength of pressure fluctuations, the

size of aerodynamic roughness elements, the porosity and depth of the snow pack as well as on the CO_2 source strength in the soil, to name just a few. In the absence of detailed profile measurements of snow characteristics and high-quality, high-frequency pressure observations, the effect of pressure-pumping can only be roughly estimated. The amount of CO_2 that can be stored in the snow pack constrains the maximum emission to the atmosphere or uptake by the snow cover and can be assessed as a function of snow depth δ, CO_2 concentration in the snow pores c_{CO_2} and snow porosity η, which is the ratio between air filled pores in the snow cover and the total volume of the snow pack. Since the CO_2 concentration is typically given in units of ppm, it has to be converted to molar density using the ideal gas law

$$c_{CO_2}\ [molm^{-3}] = c_{CO_2}\ [ppm] \cdot \frac{p}{R \cdot T} \cdot 10^{-6}, \tag{4.33}$$

where p denotes the atmospheric pressure in Pa, $R = 8.314\, Jmol^{-1}K^{-1}$ the ideal gas constant and T the snow temperature in K. In this study a CO_2 concentration of 782 ppm in the snow pores is assumed, which is the average value of sporadic manual measurements at the Bayelva site. The amount of CO_2 in mol n_{CO_2} that is stored below 1 m^2 of the snow pack can then be estimated via

$$n_{CO_2} = \delta \cdot \eta \cdot cCO_2\ [molm^{-3}]. \tag{4.34}$$

The snow porosity can be calculated from the measured snow density ρ_a, using

$$\eta = \frac{\rho_a - \rho_{ice} - \theta_w(\rho_{air} - \rho_w)}{\rho_{air} - \rho_{ice}}, \tag{4.34}$$

and inserting values for the density of air, ice and water $\rho_{air,ice,w}$ from the literature (Table 4.2). Adapted from Roth et al. (1990), the volumetric liquid water content θ_w of the snow cover can be estimated based on dielectric measurements, using

$$\theta_w = \frac{\tau_a^\omega - (1-\eta) \cdot \tau_{ice}^\omega - \eta \cdot \tau_{air}^\omega}{\tau_w^\omega - \tau_{air}^\omega}, \tag{4.35}$$

where τ_a denotes the snow dielectric constant, as obtained from half-hourly Time Domain Reflectometry (TDR) measurements at the Bayelva site, $\tau_{air,w,ice}$ the dielectric constants of air, water and ice, respectively, as documented in the literature (Table 4.2). Inserting equation (4.35) into (4.34) and solving for η gives

$$\eta = -\frac{-(\tau_w^\omega - \tau_{air}^\omega)(\rho_a - \rho_{ice}) + (\tau_a^\omega - \tau_{ice}^\omega)(\rho_{air} - \rho_w)}{-\left((\tau_{ice}^\omega - \tau_{air}^\omega)(\rho_{air} - \rho_w) + (\tau_w^\omega - \tau_{air}^\omega)(\rho_{air} - \rho_{ice})\right)} \approx \frac{6532.016 - 998.7\tau_a^{0.5}}{8413.807}$$

(4.36), when inserting the values, given in table 4.2 and assuming ω=0.5 (Roth et al. 1990).

Table 4.2: Approximate permittivity and density values of snow, air, water and ice. Snow permittivity is obtained from automated measurements every 30 minutes and snow density is the average value of sporadic manual measurements, while the remaining values are taken from the literature. The temperature and pressure dependency of the densities are ignored in this context.

	Permittivity τ	Density ρ [kgm^{-3}]
Snow	Measured every 30 min	~345
Air	~1	~1.3
Water	~88	~1000
Ice	~3	~918

4.5.2 CO_2 solution

It is furthermore speculated that the observed CO_2 uptake could be related to the solution of CO_2 in meltwater or in unfrozen pore water in the snow or soil (Lüers et al., 2014; Pirk et al., 2017), as it was already recorded for ice cores (Jinho et al., 2008).

According to Weiss (1974) the concentration of CO_2 in molm^{-3} in fresh water can be approximated by

$$c_{CO_2} = 10^3 \frac{l}{m^3} \cdot K_0 \cdot \frac{p_{CO_2}}{101325\ Pa}, \tag{4.37}$$

where p_{CO_2} denotes the partial pressure of CO_2 in Pa, which can be obtained from the atmospheric mass density of CO_2 using the ideal gas law

$$p_{CO_2} = c_{CO_2} \cdot R \cdot T. \tag{4.38}$$

K_0 in units mol l^{-1}atm^{-1} of is given by

$$ln(K_0) = -58.0931 + 90.5069\frac{100}{T} + 22.2940\frac{T}{100}. \tag{4.39}$$

In order to estimate the potential for CO_2 solution in the liquid water part of the snow pack, the snow temperature has to be inserted for T. Calculating the snow porosity using equation (4.34) and inserting the result into equation (4.35) gives the volumetric liquid water content of the snow cover θ_w. The amount of CO_2 in mol n_{CO_2} that can be dissolved in the liquid water below 1 m^2 of the snow pack is then given by

$$n_{CO_2} = \theta_w \cdot \delta \cdot c_{CO_2}. \tag{4.40}$$

4.5.3 Advective transport of CO_2 and storage below the measurement height

Storage and advection of CO_2 do not only occur inside the snow pack (section 4.4.1) but can also play a significant role in the atmospheric layer between the surface and the measurement height.

During calm periods, when low winds and stable stratification suppress a turbulent mixing of the surface layer, the gas exchange at the surface can be decoupled from the observations at the measurement height (Aubinet et al., 2012; Burba, 2013; Schaller et al., 2019). Under these conditions, which are typical of the Arctic winter as a consequence of intensive longwave radiative cooling of the surface, the CO_2 that is released from the ground accumulates below the measurement system (Aubinet et al., 2012). Such situations are typically interrupted by different meteorological phenomena on the mesoscale, including the passage of fronts,

atmospheric gravity waves, low-level jets, and katabatic winds (Schaller et al., 2019). Associated with an increase in horizontal wind speed, these mechanisms trigger the onset of turbulent mixing. In the absence of other influences, the CO_2 that pooled close to the ground is then transported upwards to the measuring instruments. Thus the detection of the CO_2 efflux from the soil is just delayed, leaving a longer term CO_2 budget unchanged (Aubinet et al., 2012).

However the simultaneous effect of advective transport oftentimes complicates this relationship (Aubinet et al., 2012). On the one hand, advection can remove the respired CO_2 from the ecosystem before it reaches the measurement height. It is then definitely lost to the detection by the measurement system, resulting in an underestimation of CO_2 emission (Aubinet et al., 2012). On the other hand, with the onset of higher wind speeds, further CO_2, emitted at a remote place, can be advected to the measurement site, resulting in an overestimation of the local CO_2 production (Schaller et al., 2019). Since advection can introduce a significant bias to the local CO_2 budget, it is crucial to assess whether the CO_2 recorded by the measurement system was emitted locally and just temporarily pooled near the surface or was horizontally advected from a remote region (Schaller et al., 2019).

One indicator could be the duration of a flux event, since the reservoir that feeds the CO_2 emissions is probably much larger in the case of advective transport and therefore able to sustain the increased CO_2 fluxes over a longer period of time. Furthermore the local source strength depends on the time since decoupling, the time since the last event took place, the intensity of vertical mixing and the emission rate from the ground, which determines the reaccumulation of CO_2 near the surface (Schaller et al., 2019). In the case studies the ability of the OOT (Section 4.2.2) to filter out lower-frequency flux contributions, related to advective transport, is investigated. A more detailed insight into the frequency-dependent flux contributions can be obtained from spectral and cospectral analyses.

In EddyPro the storage flux SF_{CO_2} is calculated following Aubinet et al. (2001) as

$$SF_{CO_2} = \int_0^{h_m} \frac{\partial c_{CO_2}}{\partial t} dz, \tag{4.41}$$

performing an integration of the temporal change of the CO_2 concentration from the ground to the measurement height h_m. CO_2 concentration profile measurements are key to detect CO_2 accumulation below the sensor height and thus to reliably quantify the gas flux storage (Burba, 2013). Since such data is not available at the Bayelva site, the storage flux is approximated by one-point time derivatives, assuming that all gradients nullify at ground level and that the profile is linear from the measurement point to the ground. This extreme assumption is probably not true in most cases, which is why one should be very cautious when interpreting the storage flux term (LI-COR Inc., 2020).

5 Results

In the following chapter the research results obtained in this study will be presented. First of all, in section 5.1, an overview of the detected events, their distribution over the study period as well as an estimate of their role in the annual carbon exchange will be given. These results will briefly be compared to the ones obtained by Lüers et al. (2014) for 2008/2009. Section 5.2 then analyzes the overall characteristics of the events, including different event types, their typical duration and magnitude. Following, the events will be related to characteristic meteorological conditions in section 5.3. Subsequently section 5.4 evaluates the usability of the fluxes during the events as compared to the data outside the events on the basis of several quality criteria. The spectral and cospectral analyses performed in section 5.5 serve as additional tools to assess the performance of the measuring instruments. Section 5.6 comprises two case studies, in which the environmental conditions as well as the quality of the individual flux estimates during two distinct events will be assessed in more detail. Subsequently the possible contributions of physical drivers as well as methodological aspects to these events will be discussed.

5.1 Overview

Based on the methodology explained in section 4.4.2, 52 events could be identified during the study period (Figure 5.1). A detailed overview of the individual events is provided in Appendix A.2.

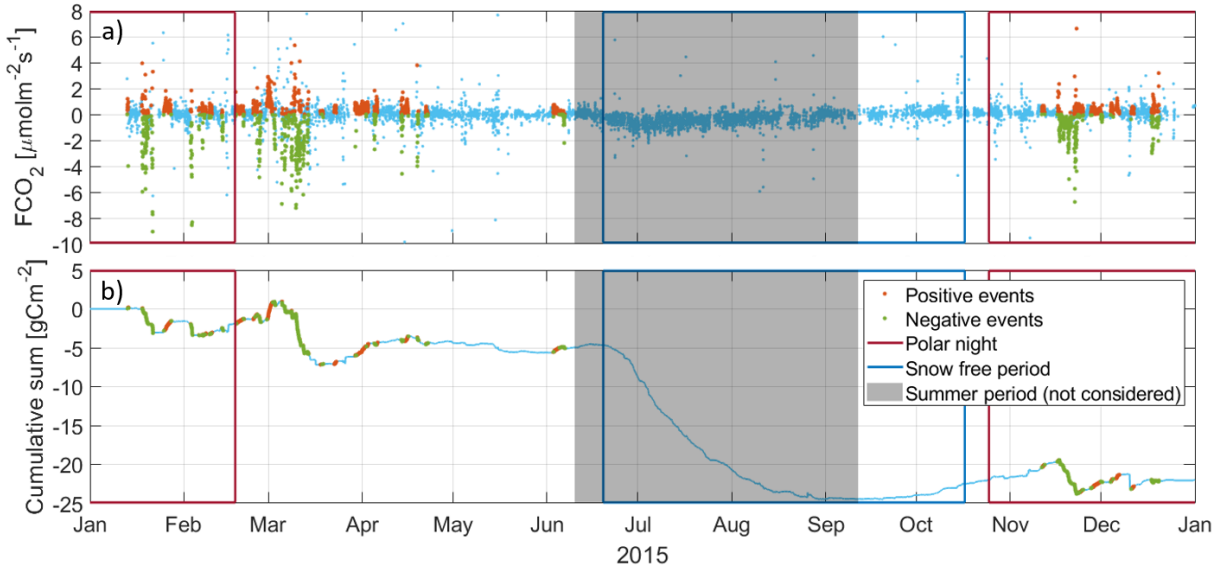

Figure 5.1: (a) Flux time series 2015 with the detected events. Positive fluxes during the events are marked in red, negative ones in green. **(b)** Event times superimposed on the cumulative sum of the flux time series.

In total the events cover about 20 % of the study period and amount to a net CO_2 uptake of -6 gCm^{-2}. Therefore the events account for about 30 % of the annual net uptake of -21 gCm^{-2}. Table 5.1 compares the carbon budgets for several time periods to the ones published by Lüers et al. (2014) for the one-year period between March 2008 and March 2009. Since the focus of this study is on the flux events, carbon budget calculations only serve a rough estimation of their contribution to the annual carbon balance. Therefore in contrast to the study by Lüers

et al. (2014) no elaborated gap filling has been performed, but the smaller gaps in the filtered time series are just bridged by linear interpolation while the fluxes during the larger data gap, which lasts until the 13 January 2015 are simply set to zero. Therefore the budget calculations in this study should be considered as purely indicative. Nonetheless the large deviation between the two annual carbon budget values is worth mentioning, since it does most likely not arise from methodological differences alone. Looking at the individual budgets for the sub-periods utilized by Lüers et al. (2014), it appears, that the much larger carbon uptake in 2015 is both caused by a larger impact of uptake events in the winter time and by a much larger CO_2 uptake during the summer months. The former can partly be explained by the larger CO_2 uptake associated with flux events of -6 gCm^{-2} in 2015 compared to about -2 gCm^{-2} in 2008/2009. Furthermore Lüers et al. (2014) document only three events, which could be related to a less sensitive detection technique as well as to an increase in the frequency of specific event triggers between 2008 and 2015. The much larger CO_2 uptake of -23 gCm^{-2} between May and August 2015 compared to -12 gCm^{-2} in 2008 could, next to methodological differences, be related to an increased biotic uptake due to a spread of more productive vegetation related to global warming. However I would consider it as unlikely that vegetation responds this strongly to warming in only seven years and would therefore assume that increased photosynthetic uptake alone cannot explain the observed deviation. Furthermore a large interannual variability of the total CO_2 uptake can generally be expected, depending among others on the thickness and duration of the snow cover, thermal conditions of the soil and vegetation characteristics (Humphreys & Lafleur, 2011). Particularly the larger CO_2 uptake between May and June 2015 could in this context be related to the generally shallower snow cover which thaws away about two weeks earlier than in 2008.

Despite the significant deviation from the study by Lüers et al. (2014), the net annual uptake of -21 gCm^{-2} still lies within the range of annual carbon budgets documented from EC measurements across the Arctic tundra. Except for a small net annual loss of +14 gCm^{-2}, detected by Oechel et al. (2014) for Alaskan tussock tundra, most studies find that the Arctic tundra is a net annual sink for CO_2. Consistent with the expected low productivity of the sparsely vegetated Bayelva site (Lüers et al., 2014), its sink strength is on the lower end of the carbon uptake recorded at Arctic sites. Depending on the characteristics of the landscape, annual net CO_2 assimilation was found to add up to -21 gCm^{-2} in a dry heath in Northeast Greenland (Lund et al., 2012), -38 gCm^{-2} in a wet tussock grassland in Northeast Siberia (Corradi et al., 2005), -64 gCm^{-2} in a wet fen in Northeast Greenland (Soegaard & Nordstroem, 1999) and -71 gCm^{-2} in the wet polygonal tundra of the Lena Delta (Kutzbach et al., 2007).

Table 5.1: Comparison of the net carbon exchange to the one derived by Lüers et al. (2014) for several time periods

	Net carbon exchange [gCm^{-2}]	
Time period as defined by Lüers et al. (2014)	2015 (this study)	2008/2009 (Lüers et al., 2014)
January - February	-0.5	0.4
November – April	-2.5	6.5
Winter (November – December)	0.9	2.0
Spring (May - June)	-6.0	-1.5
Summer (July - August)	-17.2	-10
Autumn (September – October)	4.4	4.5
Whole year	-21.4	0
Study period (12 September – 10 June)	0.6	

5.2 Event statistics

The following section analyzes the overall characteristics of the events. Therefore the events will first of all be classified concerning the specific sequence of their consecutive 30 min fluxes. In the remaining subsections, the typical duration of the events, their spacing as well as peak fluxes and the net carbon exchange during the events will be examined.

5.2.1 Event classification

Three distinct structural types of events appear from the time series, concerning the temporal development of the CO_2 fluxes during an individual event. Since these different event types might be caused by different triggers, the events are consequently classified into “single peak events”, “bidirectional events” and “clusters”, following Schaller et al. (2019) (Figure 5.2).

Events are labelled as single peak events, if they roughly show the following pattern: the CO_2 fluxes increase regularly until they reach a maximum peak or a plateau, then drop back to their starting values. These single peak events can further be distinguished with respect to the direction of the involved fluxes. Events/fluxes, showing an apparent CO_2 uptake into the ground will in the following be referred to as negative and events/fluxes, indicating CO_2 emission to the atmosphere as positive events/fluxes. The terms of uptake and emission will in contrast be avoided since they imply physical mechanisms, which are not verified yet. Bidirectional events feature a sequence of two consecutive single peak events with different flux direction. They can further be classified into “up-down” and “down-up” events, depending on the order of the two peak events. During the course of the remaining events the fluxes were found to change sign more than once. Since this pattern might arise from a close succession and probably overlapping of several single peak events, this class is termed “cluster events”. An overview of the occurrence of the different event types during the study period is given in table 5.2.

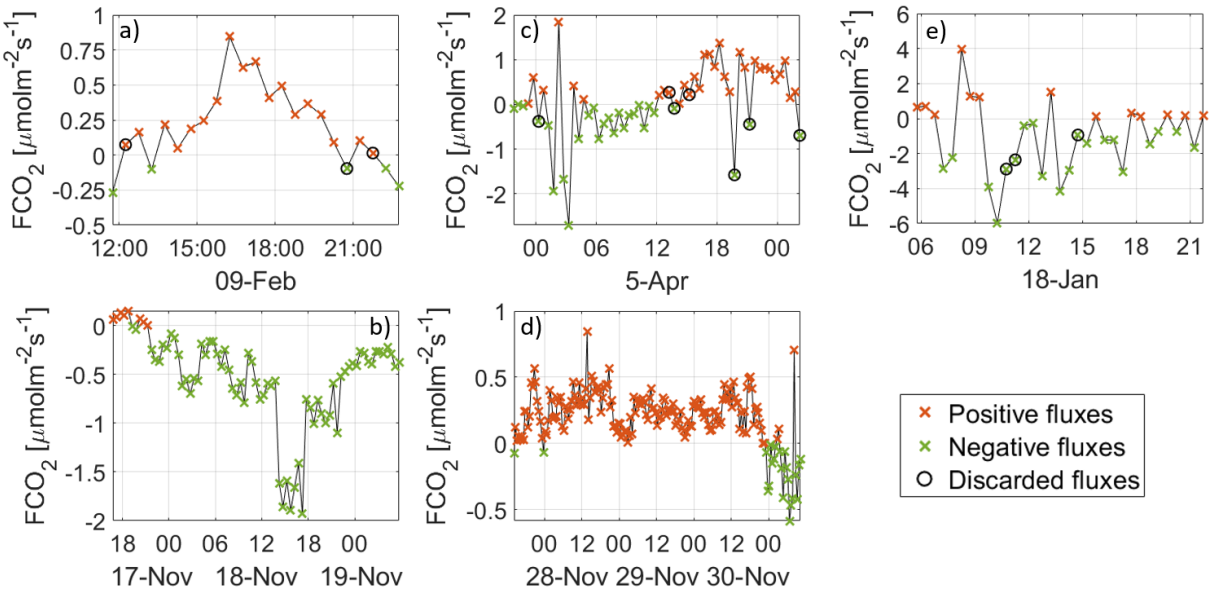

Figure 5.2: Examples for a **(a)** positive, **(b)** negative single peak event, **(c)** down-up, **(d)** up-down bidirectional event and **(e)** cluster event. Fluxes marked with a black circle are discarded in the filtered time series due to quality issues.

Table 5.2: Numbers of specific event types, identified during the study period.

Single peak events		Bidirectional events		Cluster events
29		13		10
Up	Down	Up-down	Down-up	
19	10	8	5	

5.2.2 Event duration and spacing

The duration of the events ranges between several hours and four days (Figure 5.3 a). On average an event persist for 24.5 hours. Events, which involve at least one change in flux direction, namely bidirectional and cluster events, on average last ten hours longer than single peak events and account for the four longest events.

When analysing the time spans between two consecutive events, it has to be kept in mind that between some events, fluxes of low quality were filtered out prior to the event detection. In some instances environmental conditions in the meantime show patterns similar to those typically present during events (section 5.3). Therefore it has to be assumed that further events might have occurred in this timespan, which were not detected due to instrument failures or violations of EC principles. When excluding time intervals with a large number of discarded values, the average time between two consecutive events amounts to 23.5 hours (Figure 5.3 b). In 80% of the cases, after one event, less than one day passes, before the next one occurs.

5.2.3 Magnitude of the events

Peak CO_2 fluxes during the events range between -9.0 and 3.2 $\mu molm^{-2}s^{-1}$ (Figure 5.3 c). Thus the variation in fluxes during the events by far exceeds the variation of about 2 $\mu molm^{-2}s^{-1}$, introduced by the seasonal cycle (Figure 4.9). The peak fluxes of -2.3 $\mu molm^{-2}s^{-1}$ and 1.9

µmolm^{-2}s^{-1} during the events identified by Lüers et al. (2014) fall within the most frequently attained ranges of peak values in this study.

The total net carbon exchange during an individual event ranges between an uptake of -3.6 gCm^{-2} and an emission of 2.2 gCm^{-2} (Figure 5.3 d). The average absolute net exchange of 0.56 gCm^{-2} per event is thus much smaller than the 2 to 3 gCm^{-2} documented by Lüers et al. (2014). However since the study by Lüers et al. (2014) did not focus on the flux events, the authors probably only mentioned the largest and thus most obvious events, while further smaller events might have remained undetected.

No clear differences between the characteristics of the different event types can be identified.

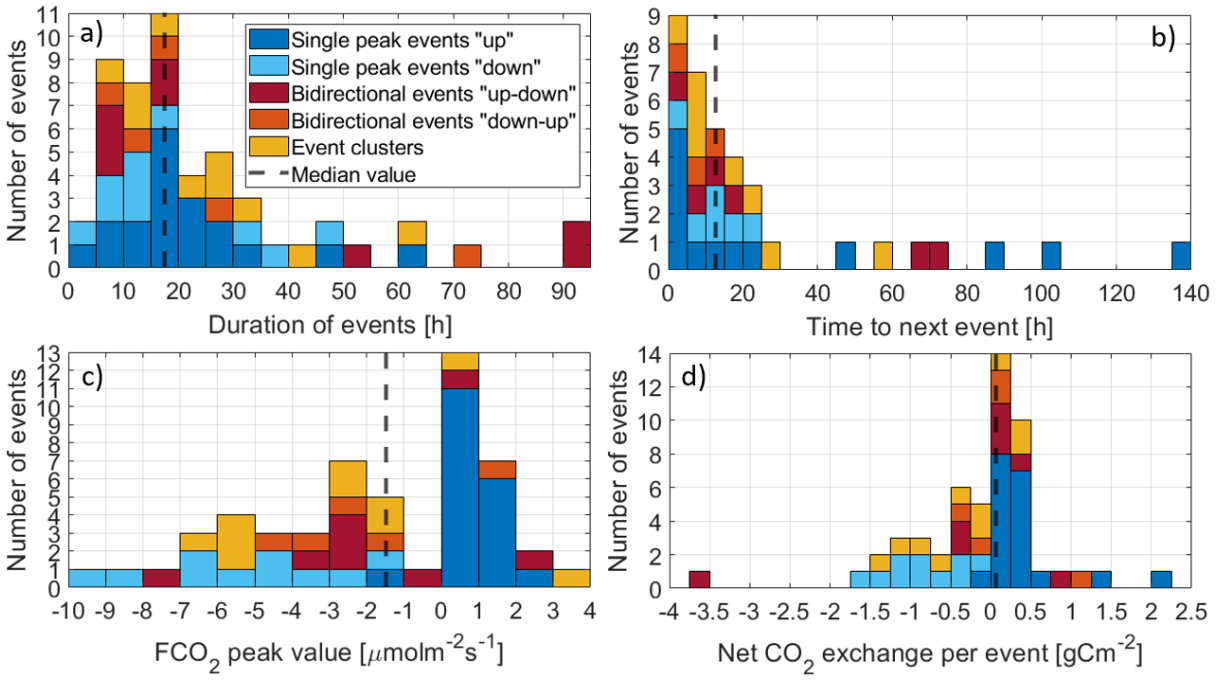

Figure 5.3: Overview of the distributions of **(a)** durations, **(b)** time spans between two consecutive events, **(c)** peak CO_2 fluxes and **(d)** the total net exchange of CO_2 on the different event types.

5.3 Meteorological conditions during the events

The durations of the events determined in section 5.2.2 suggest a meso- or synoptic-scale driver of the periods of unusually high absolute CO_2 fluxes. The following section therefore searches for repetitive patterns in the meteorological conditions during the flux events. For this purpose a detailed analysis of the meteorological data obtained from the Bayelva weather station is performed involving synoptic phenomena, wind regimes, turbulence characteristics, the atmospheric stratification and energy fluxes at the study site.

5.3.1 Events and synoptics in the annual cycle

Figure 5.4 reveals large variations in meteorological parameters at the study site, particularly during the winter months. This is related to the location of Svalbard in the border zone between a mostly anticyclonic circulation of cold artic air in the north and cyclonic movement of mild maritime air in the south (Førland et al., 1997). Related to the varying extension of these air masses, Svalbard is in turns under the influence of moist atlantic air, associated with relatively warm air temperatures and overcast skies and dry polar air masses with cold air

temperatures and clear skies, respectively (Førland et al., 1997, Westermann et al., 2009). The largest fluctuations in weather conditions occur in winter, when the contrast in temperature between the two air masses is most pronounced (Førland et al., 1997). The exchange of air masses is further stimulated by a maximum in cyclone frequency and intensity during the winter time (Zhang et al 2004; Isaksen et al., 2016; Wei et al., 2017) with four to six cyclones per month (Orvig 1970) or 20 to 40 extreme cyclone events in the Arctic North Atlantic per winter season (Rinke et al., 2017). In figure 5.4 the advection of southern air masses is marked by a simultaneous occurrence of relatively high air temperatures, high absolute humidity as well as high absolute values of incoming and outgoing longwave radiation, the latter indicating cloudy conditions. Under the influence of northern air masses the study site is on the contrary subject to relatively low air temperatures, low absolute humidity and reduced incoming as well as outgoing longwave radiation, indicating clear sky conditions. Except for the one in June, all CO_2 events occur in the time between January and April as well as in November and December, simultaneous to the largest variations of the atmospheric quantities.

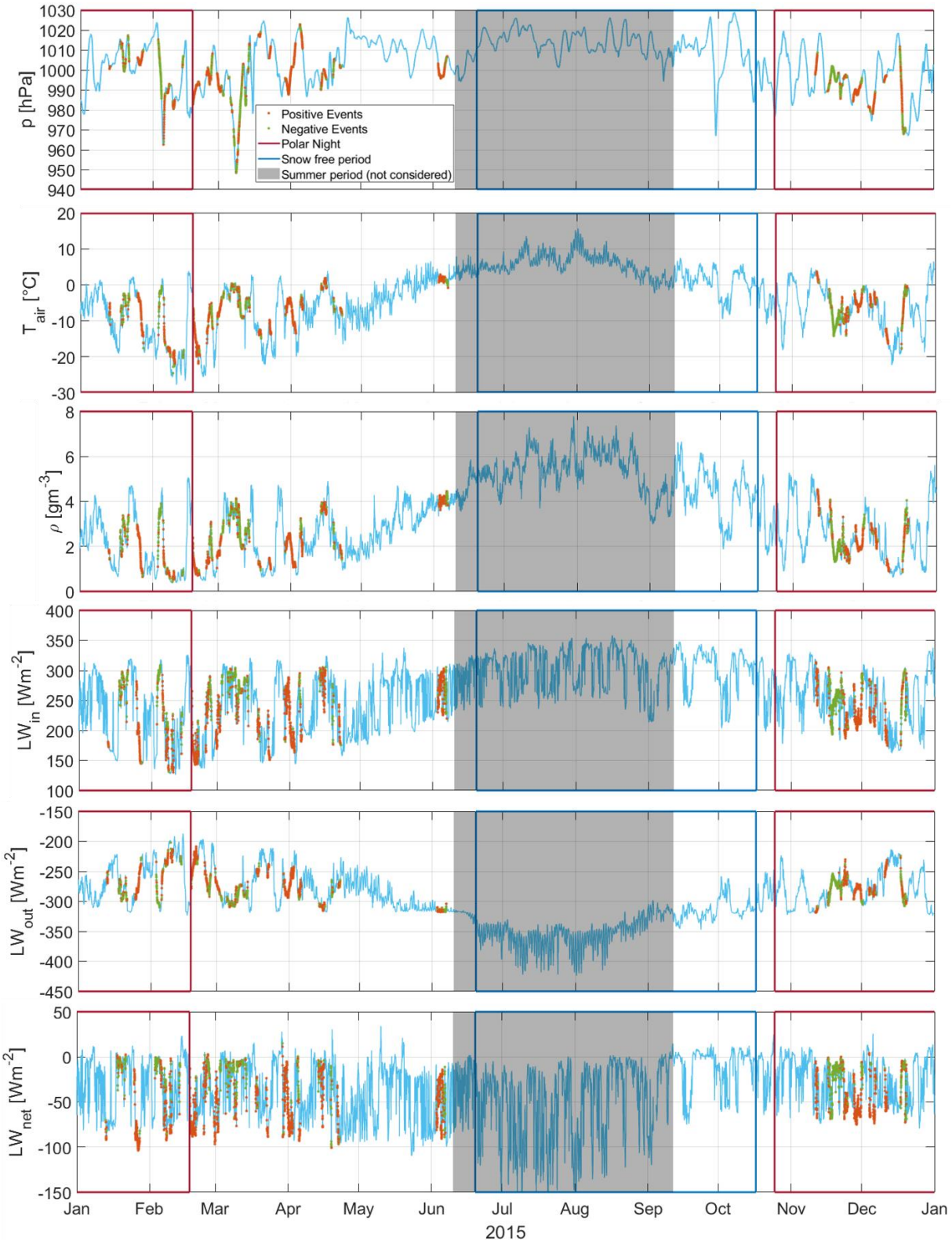

Figure 5.4: The annual cycle of atmospheric pressure, air temperature, absolute humidity, incoming, outgoing and net longwave radiation as obtained from the Bayelva meteorological station. Times of positive FCO_2 values during the CO_2 events are marked in red and negative ones in green, respectively. The direction of the radiation is defined inversely to the one of the surface flux, according to the convention, with negative radiation values indicating that the surface loses energy to the atmosphere and vice versa.

In the following the behaviour of the meteorological variables, which are directly affected by the exchange of different air masses will be assessed in detail for the event periods.

46 of the 52 events occur during distinct changes in atmospheric pressure. During 23 of these events there is an increase in atmospheric pressure while 11 events occur during a pressure decrease. Both increases and decreases of atmospheric pressure on average amount to 8 hPa per event with a mean rate of change of 0.5 $hPah^{-1}$. On average the pressure change starts 14 h before the beginning of the event and abates 19 h after the end of the event, in total comprising a mean difference of 19 hPa between minimum and maximum pressure. During ten events the atmospheric pressure reaches a local minimum and during two events a maximum, respectively. Four of the remaining six events occur on a maximum pressure plateau and two on a minimum plateau. Together with the usually intermediate pressure levels of between 990 and 100 hPa during the events (Figure 5.5) this indicates that the occurrence of CO_2 events is more strongly correlated to distinct changes in atmospheric pressure than to absolute pressure values or the direction of pressure change.

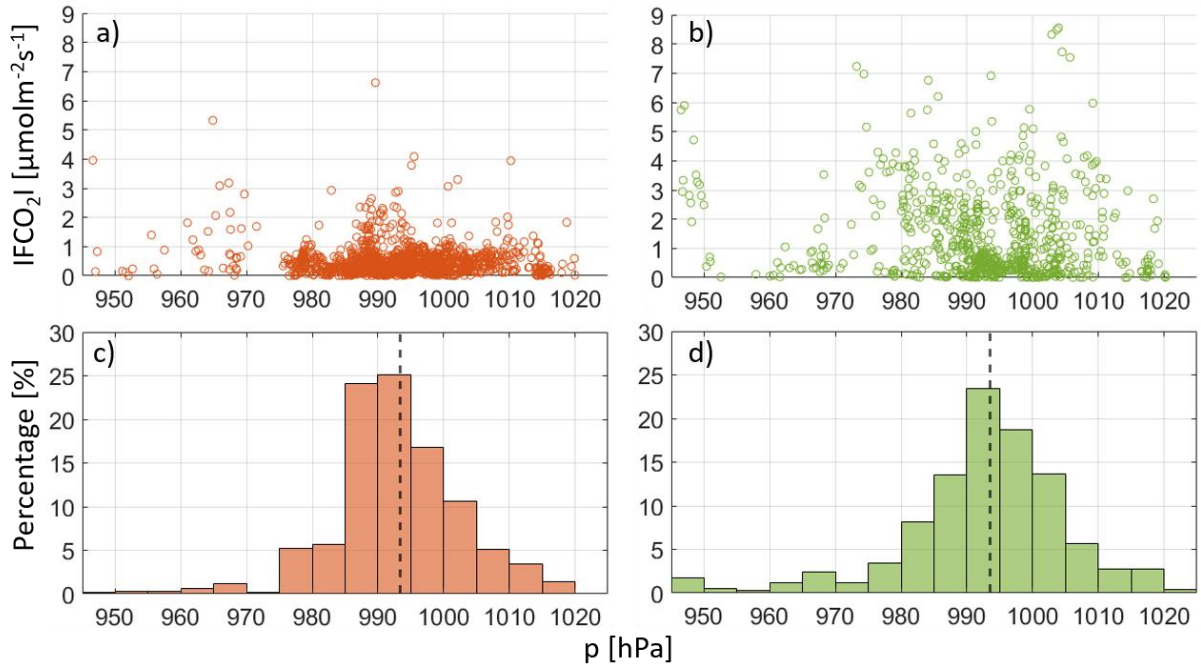

Figure 5.5: Absolute CO_2 flux as a function of atmospheric pressure (a, b) and frequency distribution of atmospheric pressure classes (c, d) during event times with (a, c) positive and (b, d) negative FCO_2. The dashed line in the histograms marks the respective median value.

Air temperatures during the events are similarly representative of the general temperature distribution during the winter months, with most events and the ones with the largest magnitude occurring at intermediate temperatures of between -10 °C and 0°C (Figure 5.6).

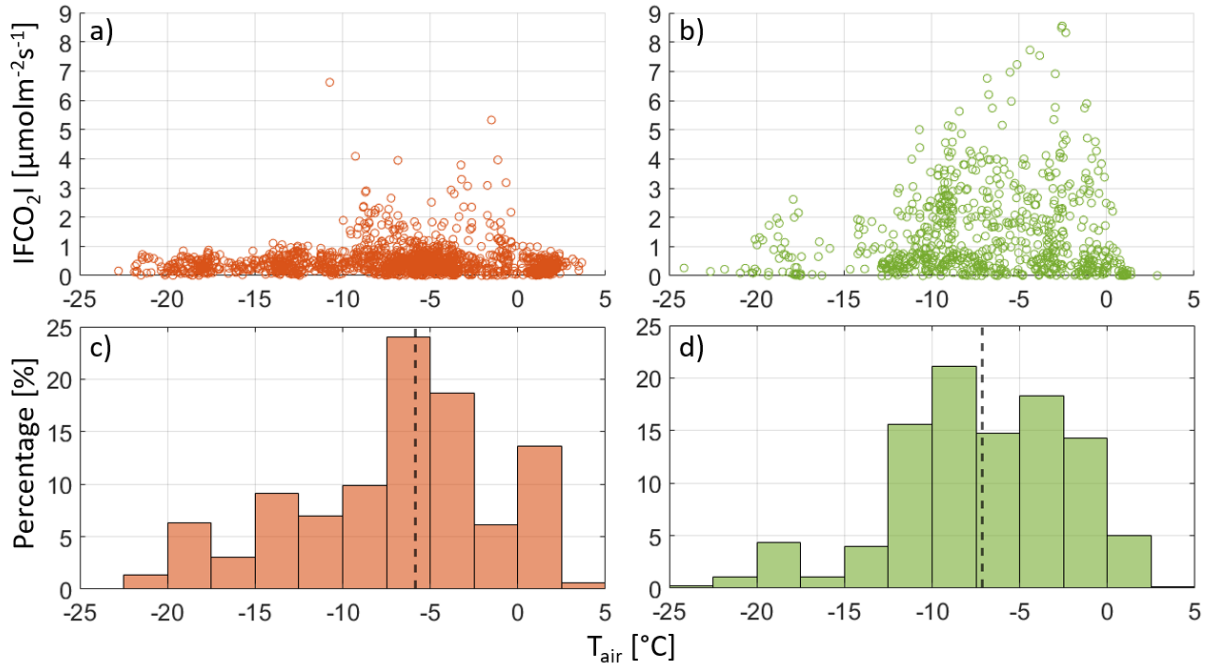

Figure 5.6: Absolute CO_2 flux as a function of air temperature (a, b) and frequency distribution of air temperature classes (c, d) during event times with (a, c) positive and (b, d) negative FCO_2. The dashed line in the histograms marks the respective median value.

While the same applies for absolute humidity, relative humidity shows a clearly tendency towards higher values during negative event fluxes with the largest absolute fluxes occurring at the highest humidity levels (Figure 5.7).

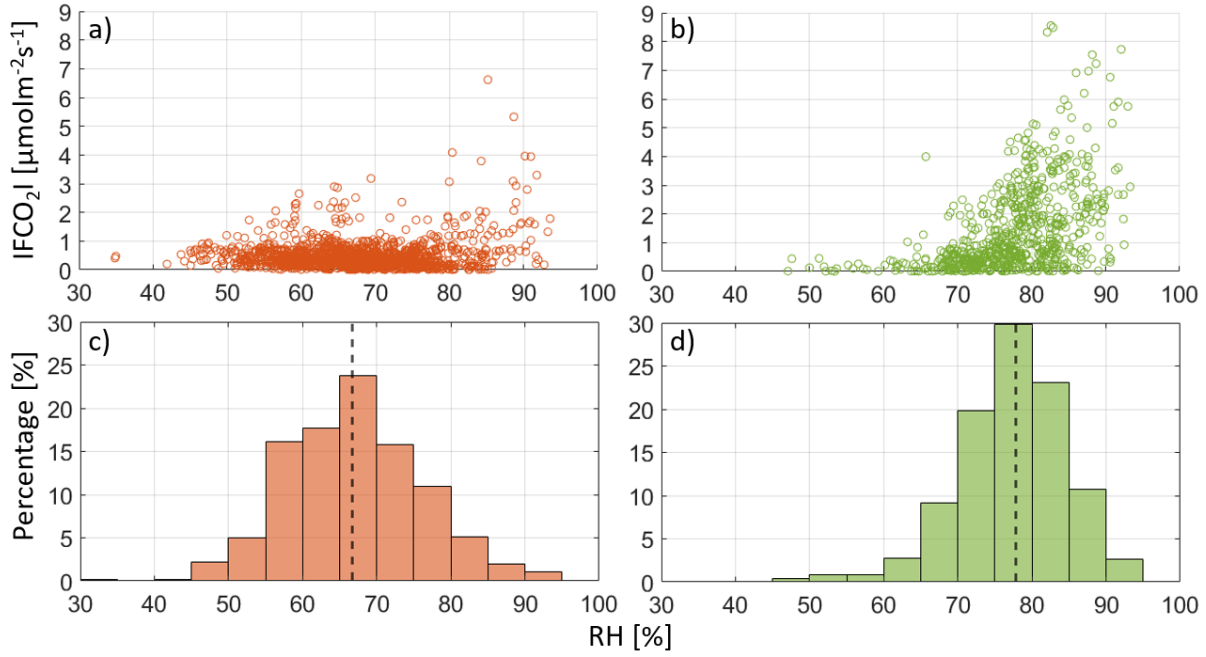

Figure 5.7: Absolute CO_2 flux as a function of relative humidity (a, b) and frequency distribution of relative humidity classes (c, d) during event times with (a, c) positive and (b, d) negative FCO_2. The dashed line in the histograms marks the respective median value.

During the winter period, when the influence of incoming shortwave radiation is low, either due to polar night conditions or due to the high albedo of the snow covered surface, long-

wave radiation becomes the main forcing of the system (Westermann et al., 2009). During the entire study period the outgoing exceeds the incoming longwave radiation, rendering the net longwave radiation the dominant energy loss term during the winter.

The occurrence of positive events is approximately evenly distributed over the whole range of incoming (Figure 5.8), outgoing (Figure 5.9) and net longwave radiation values (Figure 5.10), attained during the study period. Negative event fluxes, and especially the ones of larger magnitude, on the contrary predominantly occur during periods of large absolute incoming as well as outgoing longwave radiation, resulting in a net longwave radiation close to zero. Together with the generally increased relative humidity, this might indicate a frequent occurrence of low level clouds or fog during negative event fluxes.

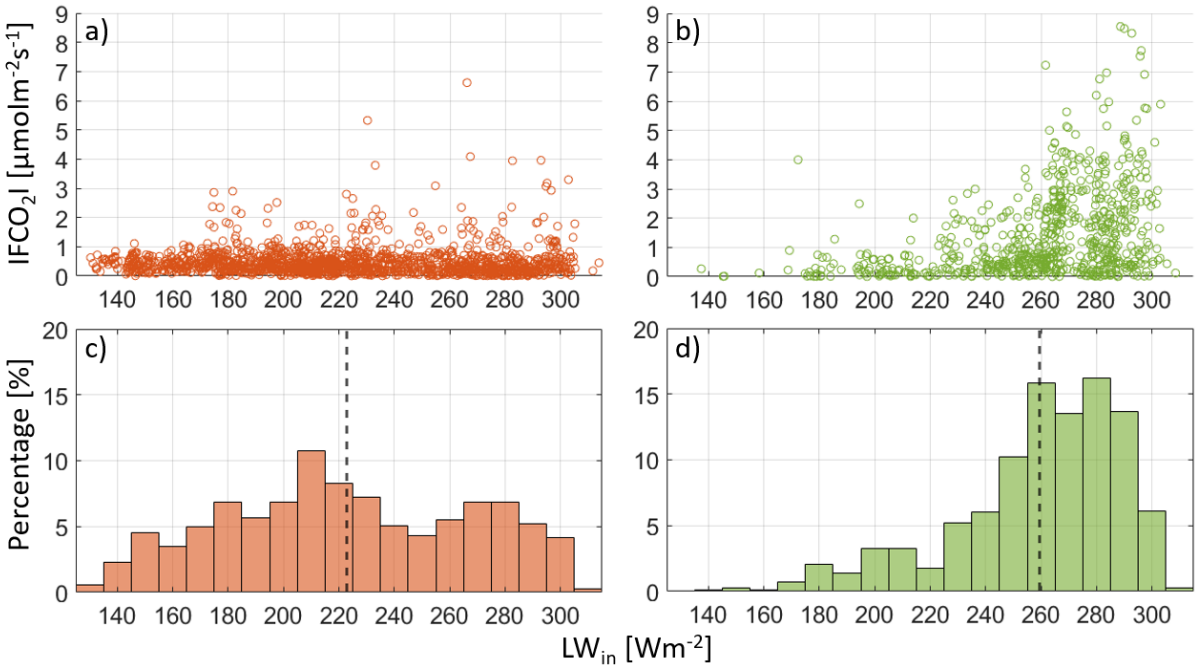

Figure 5.8: Absolute CO_2 flux as a function of incoming longwave radiation (a, b) and frequency distribution of incoming longwave radiation classes (c, d) during event times with (a, c) positive and (b, d) negative FCO_2. The dashed line in the histograms marks the respective median value.

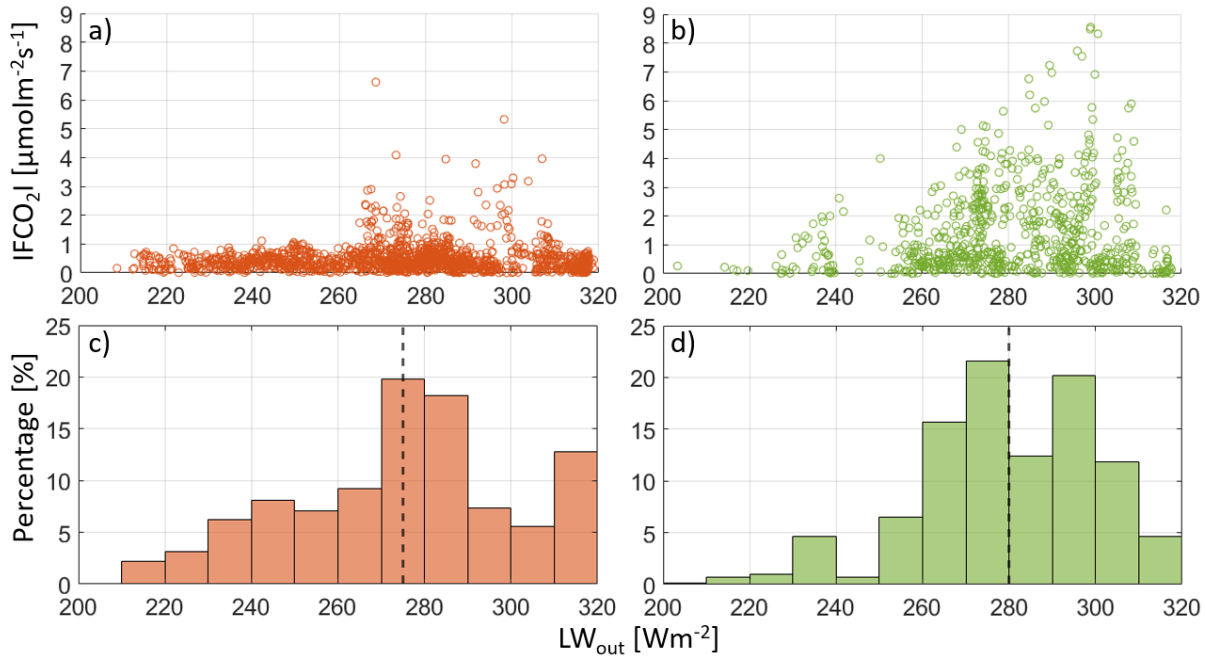

Figure 5.9: Absolute CO_2 flux as a function of absolute outgoing longwave radiation (a, b) and frequency distribution of absolute outgoing longwave radiation classes (c, d) during event times with (a, c) positive and (b, d) negative FCO_2. The dashed line in the histograms marks the respective median value.

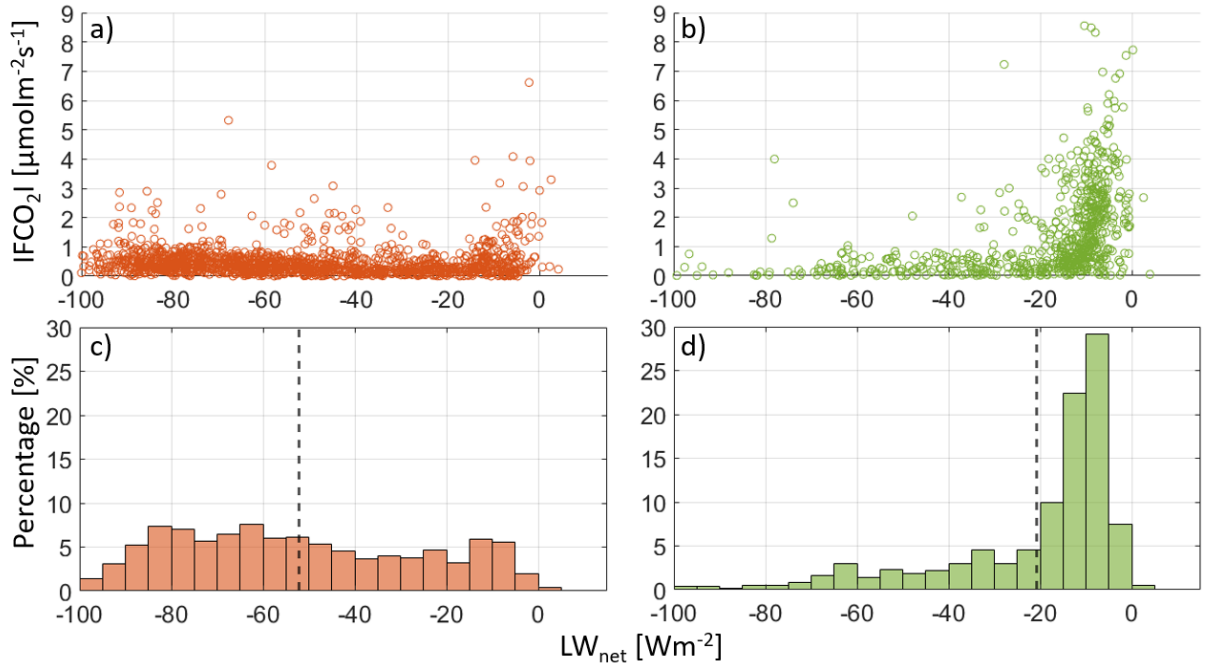

Figure 5.10: Absolute CO_2 flux as a function of net longwave radiation (a, b) and frequency distribution of net longwave radiation classes (c, d) during event times with (a, c) positive and (b, d) negative FCO_2. The dashed line in the histograms marks the respective median value.

5.3.2 Wind regimes during the events

The shift of air masses is moreover directly related to distinct changes in the wind regimes. The following section therefore investigates the characteristic wind directions and wind speeds at the study site in general as well as during the events.

5.3.2.1 Wind direction

In order to evaluate the wind directions during the CO_2 events, first of all the typical wind conditions at the Bayelva site have to be identified. An overview of the wind conditions during the winter months is provided in figure 5.11 a and contextualized within the local topography. The wind directions can generally be subdivided into three prevailing wind sectors, in total representing 73 % of the study period. The frequency of occurrence of the different wind sectors is listed in table 5.3. During most of the time, a southerly flow, advects air masses descending along the eastern branch of the Brøggerbreen glacier. This wind sector is related to katabatic outflow from the Brøggerbreen glacier, which is channelled along the slopes of the Zeppelin mountain range and is characterized by wind speeds typically lower than 5 ms^{-1}. The two other prevailing wind directions are related to the mountains channelling the large scale wind field in a west-east direction along the fjord (Hanssen-Bauer et al., 1990). During the second most frequent conditions the wind enters the Bayelva catchment from inner Kongsfjorden in the east. Next to the large scale wind field this wind direction can also be related to drainage winds transporting cold, heavy air from the inland glaciers to the warmer sea (Hanssen-Bauer et al., 1990). Winds coming from the outer Kongsfjorden, north-west of the study site, are recorded the least frequently. The prevailing wind directions at the Bayelva site thus mainly result from the channelling of the wind by the local topography. Therefore the large scale wind field cannot directly be derived from the local wind direction. Nonetheless figure 5.12 reveals some connections to the large scale synoptic situation. Local easterly flows mainly occur during the passage of anticyclones or large scale winds from the east to south and are thus associated with a slight shift of the frequency distribution towards higher air temperatures (Figure 5.13). North-westerly winds are primarily associated with large scale advection from the north, leading to a more frequent occurrence of very low air temperatures. For the southerly wind sector on the other hand no clear relation to the large scale wind field could be identified. Measurements between 2007 and 2017 at the Eddy tower as well as data recorded at the meteorological station on Leirhaugen hill between 1998 and 2017 furthermore reveal that the pattern observed during the study period is representative of the overall wind conditions at the Bayelva site (Westermann et al. 2009, Boike et al. 2018). If excluding the events from the analysis, the distribution of wind directions is further shifted to the most frequently occurring southern wind sector at the expense of the two remaining main wind sectors. Due to the typical low-wind conditions an increased percentage of intermediate wind directions outside of the prevailing wind sectors is recorded. During the events the main wind sectors are on the contrary further pronounced with a predominant occurrence of easterly and north-westerly flows.

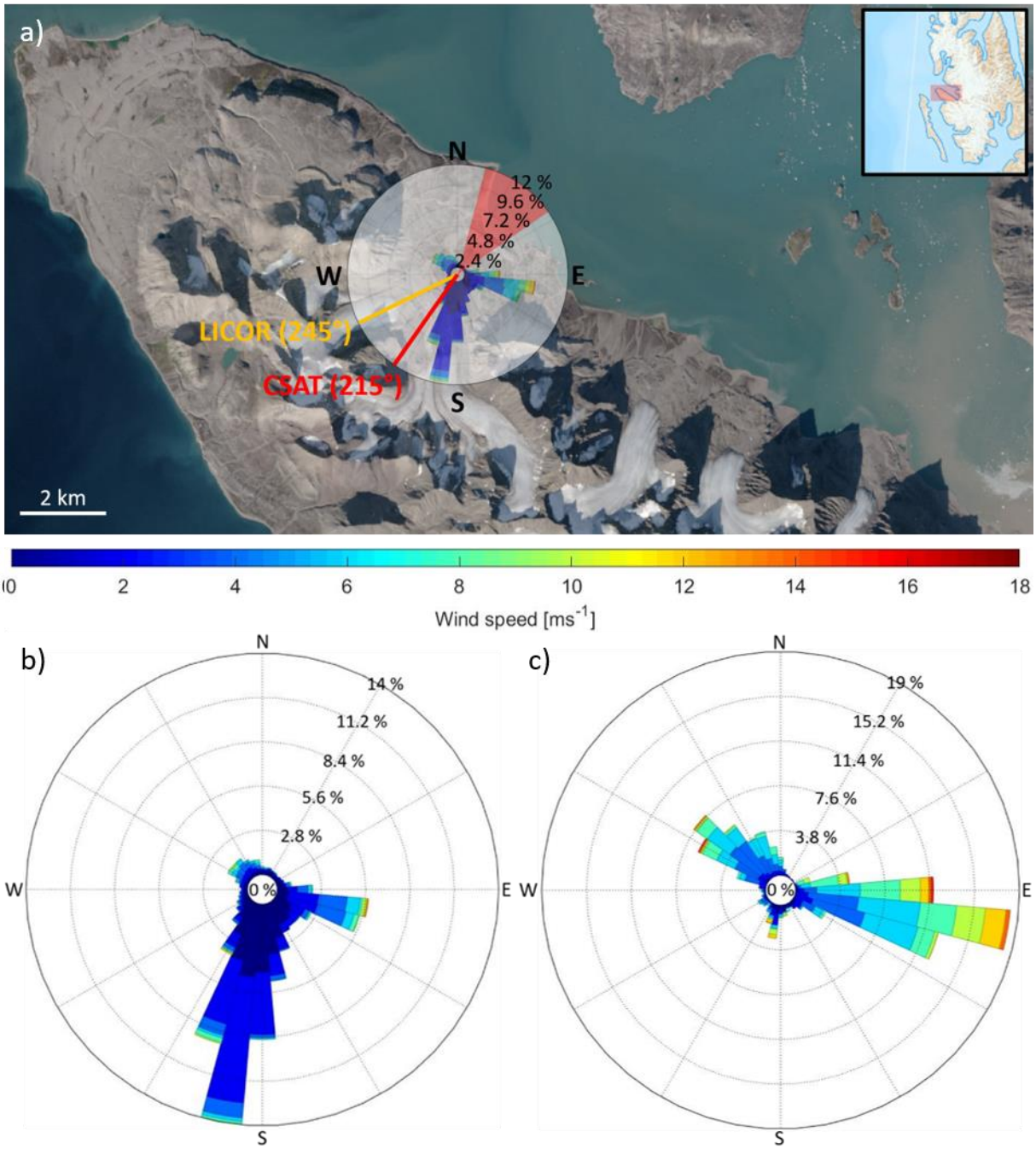

Figure 5.11: Wind rose for **(a)** the whole study period, **(b)** the study period, excluding the events and **(c)** the events. For each wind rose wind directions are depicted with a resolution of 10°. In (a) the wind rose is centred at the Eddy tower. Its size does not represent the footprint of the measurement setup, which does only extent up to approximately 100 m into the prevailing wind directions (Background image: Norwegian Polar Institute n.d.).

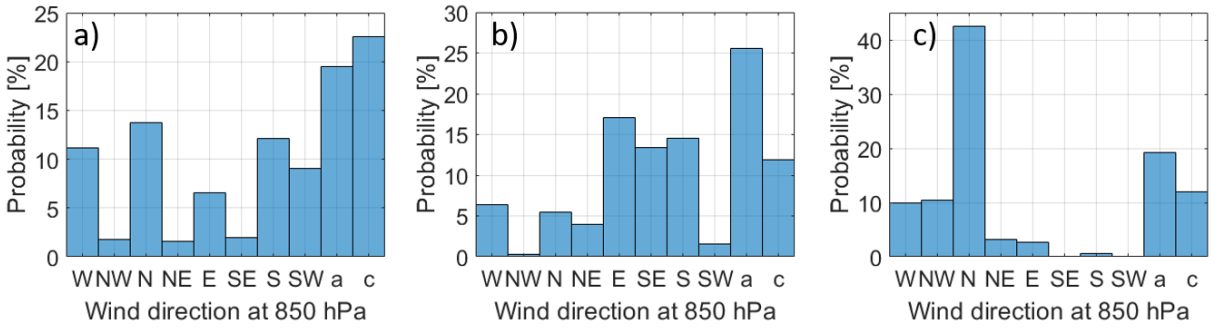

Figure 5.12: Probability distribution of the prevailing large scale wind directions based on the CWT classification using the ERA-Interim 850 hPa geopotential during local wind directions from **(a)** south, **(b)** east and **(c)** north-west. The labels a and c on the x-axis of the histograms stand for times where the centre of an anticyclone or cyclone is close to Ny Ålesund and are assigned based on shear-vorticity.

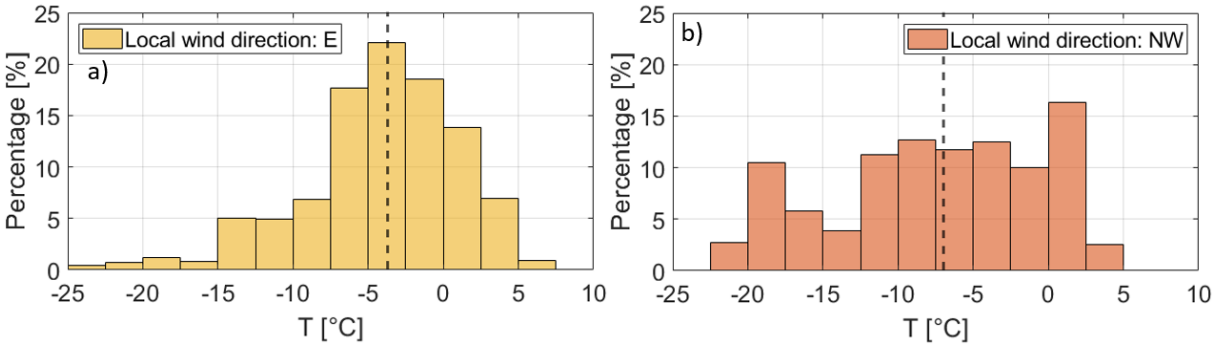

Figure 5.13: Frequency distributions of air temperatures during local **(a)** easterly and **(b)** a north westerly wind directions during the study period.

Table 5.3: Frequency of occurrence of the main wind directions as well as of wind directions outside the main sectors during the whole study period, the study period excluding the CO_2 events and during the events.

Local wind sector	Whole study period	No events	Events
S	36 %	43 %	8 %
E	23 %	17 %	50 %
NW	13 %	8 %	32 %
other	27 %	31 %	10 %

Over the course of an individual event the wind direction typically changes twice between the main wind sectors (Figure 5.14). The first turn on average occurs 1.5 hours before the beginning of the event and the second one on average follows five hours after its end. Consistent with the frequency distributions of the local wind sectors during and outside the events, the most common changes involve a turn from a southerly to an easterly or north-westerly and back to a southerly flow. Between the distinct event types no obvious difference in the wind characteristics could be identified.

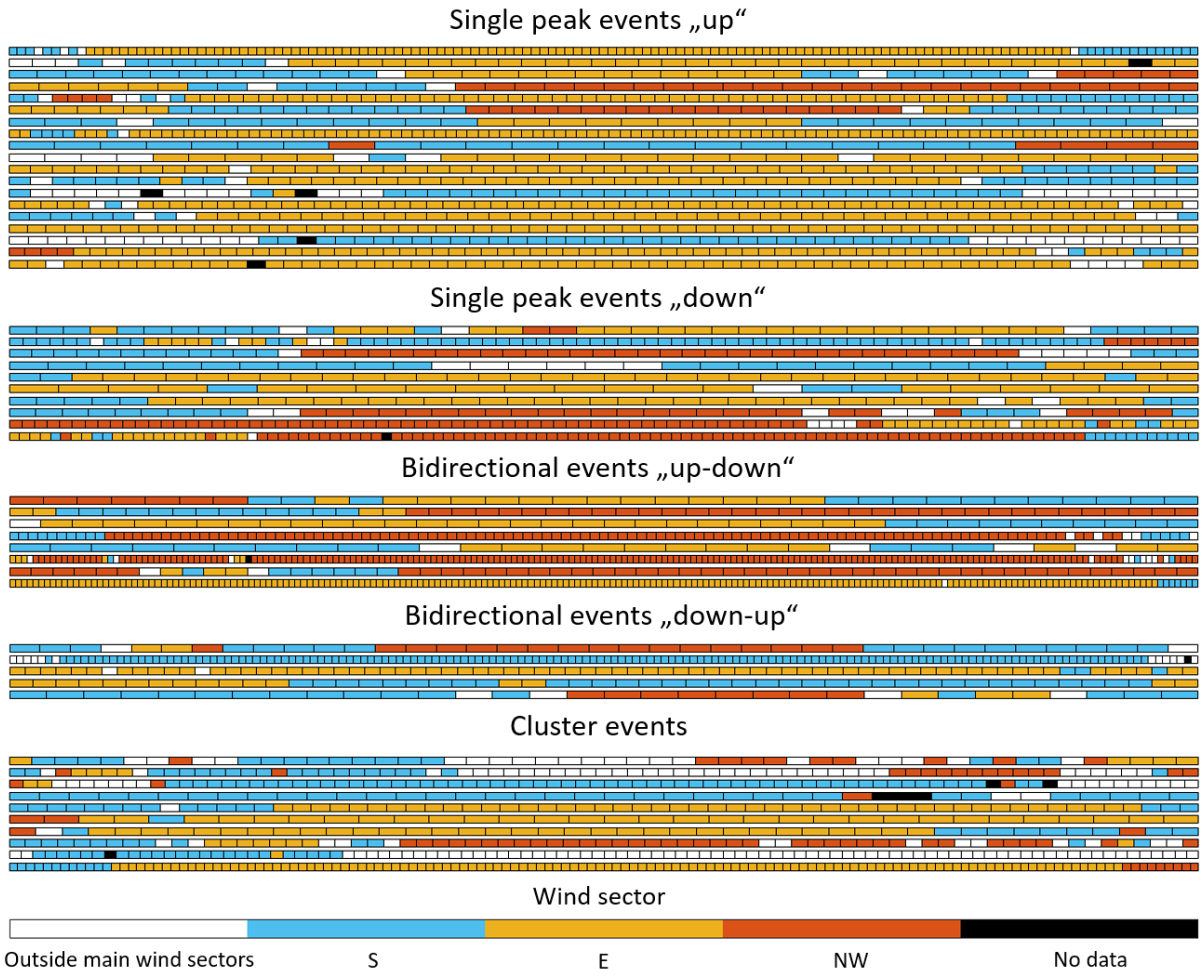

Figure 5.14: Each horizontal line shows the development of the local wind direction between five hours before the beginning and five hours after the end of a single FCO_2 event. In every line each box represent one half-hourly mean wind direction measurement. On the colour scale the prevailing wind sectors of between 155° and 225° (S), between 65° and 135° (E) and between 285° and 5° (NW) are marked.

All in all the events are associated with distinct changes in the wind direction, most frequently involving a turn from a southerly flow to a wind direction along the fjord. However they cannot be related to the advection of a specific air mass since they are found to occur both under the influence of northern and southern air masses.

5.3.2.2 Wind speed

More obviously, associated with the increased pressure gradient between the passage of cyclones and anticyclones, the FCO_2 events are typically characterized by high wind speeds. This relation could already been seen from figure 5.11, and is further clarified by the histograms in figure 5.15. During the events the median wind speed is increased by 4 ms^{-1} compared to rest of the study period.

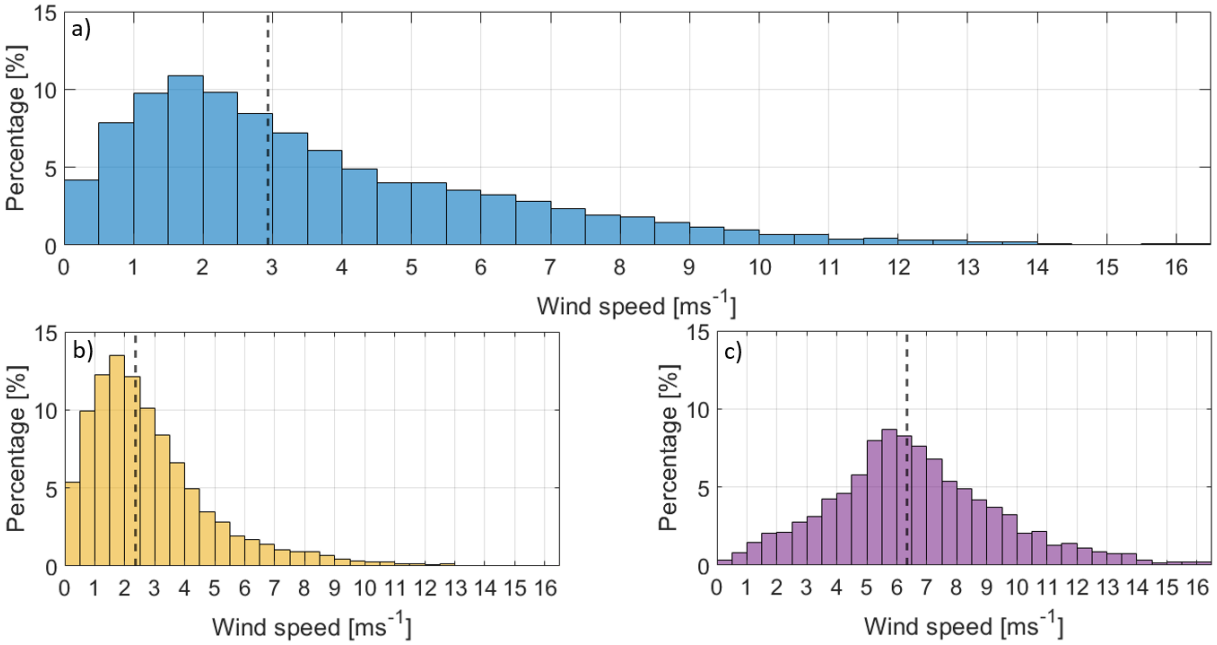

Figure 5.15: Frequency distributions of the wind speeds during **(a)** the whole study period, **(b)** the study period excluding the FCO_2 events and **(c)** the FCO_2 events. Dashed lines mark the respective median values of the distributions.

Figure 5.16 furthermore reveals a positive correlation between the magnitude of the CO_2 fluxes and the wind speed for both positive and negative event fluxes, particularly at wind speeds exceeding 8 ms^{-1}. Due to the larger share of higher absolute flux values, this relation is more pronounced in the case of negative event fluxes. This correlation was also identified by Pirk et al. (2017), who suggest an exponential increase of absolute CO_2 fluxes with increasing wind speed.

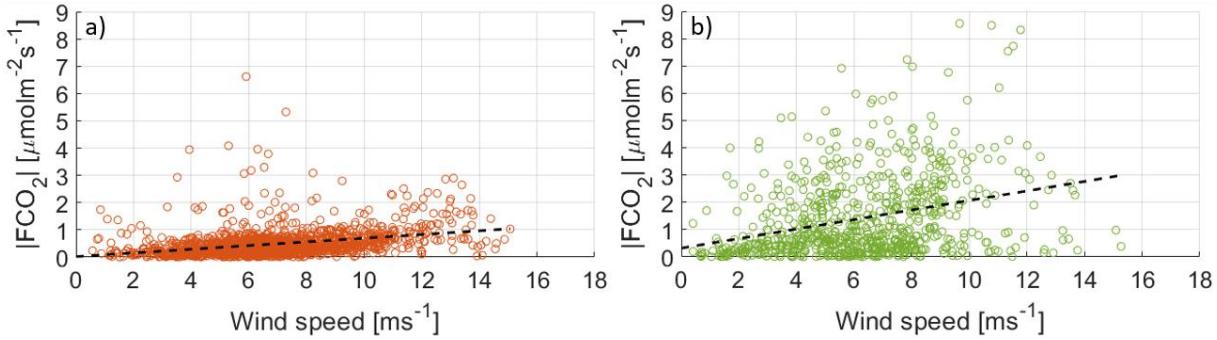

Figure 5.16: Correlation between the wind speed and the absolute CO_2 flux for **(a)** positive and **(b)** negative event fluxes. The dashed line marks the least-squares fit.

49 of the 52 individual events feature an abrupt increase in wind speed around the beginning of the event, followed by a peak or plateau of high wind speeds and a return of the wind speed to its starting level close to the end of the event (Figure 5.17). On average the wind speed starts to increase 1.5 h before the beginning of the event, reaches a maximum of approximately 9.4 ms^{-1}, following an increase by 8.2 ms^{-1}, and is back at its starting level 2.5 h after the end of the event.

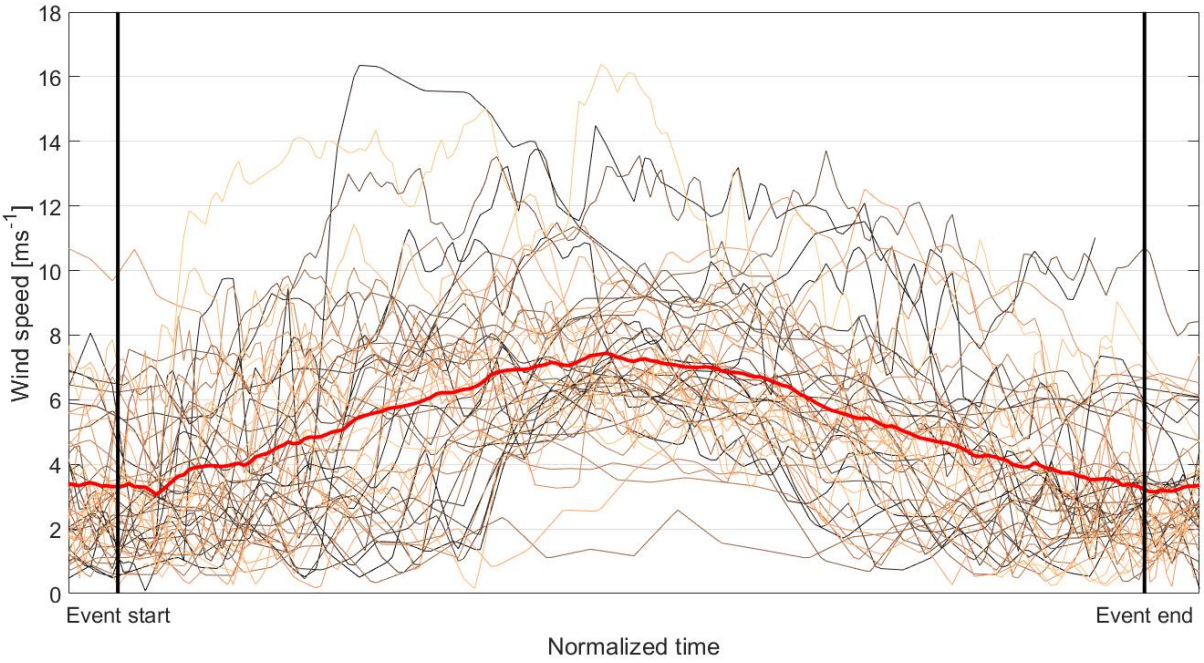

Figure 5.17: Evolution of the wind speed between five hours before and five hours after the 52 individual FCO_2 events. The red line shows the average development of the wind speed, derived through the interpolation of the individual time series to the time grid of the longest event.

5.3.3 Turbulence intensity and atmospheric stability

Wind shear is the dominant source of turbulence during the Arctic winter. Therefore the friction velocity can be interpreted as a measure of the turbulence intensity. According to a Pearson correlation coefficient of 0.8 during the study period, the friction velocity is primarily controlled by the wind speed, resulting in a similar behaviour of the two quantities. The events can thus be seen as time periods of enhanced turbulent transport within the otherwise very stable stratification of the winterly Arctic boundary layer. This onset of turbulence during periods of high wind speeds is also reflected in the stability of the atmospheric stratification during the events. When the wind speed is low, a stable stratification forms due to the intense longwave radiative cooling, supporting strong near-surface temperature inversions. In these situations turbulent fluxes between the surface and the atmosphere are reduced significantly. At high wind speeds, when atmospheric turbulence is mechanically induced, a neutral stratification forms. 43 of the 52 events thus coincide with an extended period of neutral stratification. Before as well as after the events atmospheric stability changes more frequently between unstable, neutral and stable conditions (Figure 5.18 a). This behaviour is also reflected in the general distribution of stability regimes over the study period (Figures 5.18 b to d), revealing a mostly neutral stratification during the events and more stable conditions during the remaining part of the study period.

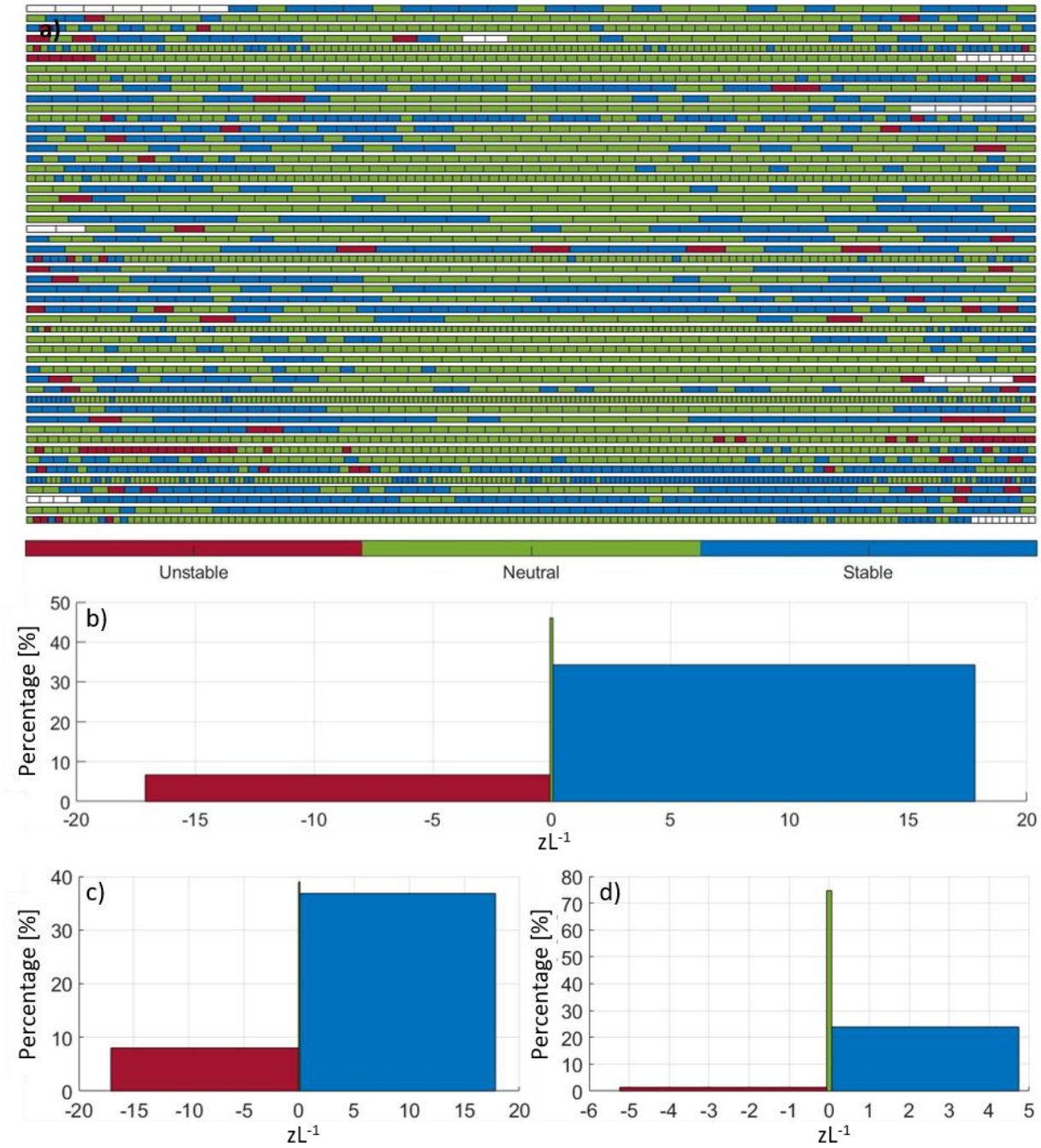

Figure 5.18: (a) Each horizontal line shows the development of the atmospheric stability between five hours before the beginning and five hours after the end of a single FCO_2 event. From the top to the bottom of the diagram the events are displayed chronologically. In every line, each box represents one half-hourly value of the Monin-Obukhov stability parameter zL^{-1}, with $zL^{-1} < -0.0625$ indicating unstable, $-0.0625 \leq zL^{-1} \leq 0.0625$ indicating neutral and $zL^{-1} > 0.0625$ indicating stable conditions (Schaller et al. 2019). Frequency distributions of zL^{-1} during **(b)** the whole study period, **(c)** the study period excluding the events and **(d)** the events.

5.3.4 Energy fluxes

Until the shortwave radiation gains more importance, the energy loss through intense longwave radiative cooling is mainly compensated by a negative average sensible heat flux, corresponding to a warming of the surface and a cooling of the atmosphere (Westermann et al., 2009). At high wind speeds the mechanical generation of turbulence facilitates the exchange of energy and gases between the surface and the atmosphere. Along with the CO_2 fluxes, the energy fluxes are therefore increased during the events (Figure 5.19). Strong downward latent heat fluxes of up to -160 Wm^{-2} then result in an increased heating of the surface at the expense of the warmer atmosphere, while considerable latent heat fluxes of up to 143 Wm^{-2} at the same time indicate a cooling of the surface through the sublimation of snow or, if present, the evaporation of water (Westermann et al., 2009). During negative event fluxes, the energy fluxes deviate less from zero (Figures 5.19 and 5.20). This can be explained by the finding of Westermann et al. (2009) that the influence of wind speed on the sensible heat flux is clearly less pronounced at high incoming longwave radiation. They suggest that due to the reduced gradient between air and surface temperature these conditions prevent a strong exchange of energy independent of the formation of turbulence. The typically high relative humidity during negative event fluxes could similarly reduce the positive correlation between wind speed and upward latent heat flux. Figure 5.20 a furthermore reveals an increase of positive event CO_2 fluxes with increasingly negative sensible heat fluxes.

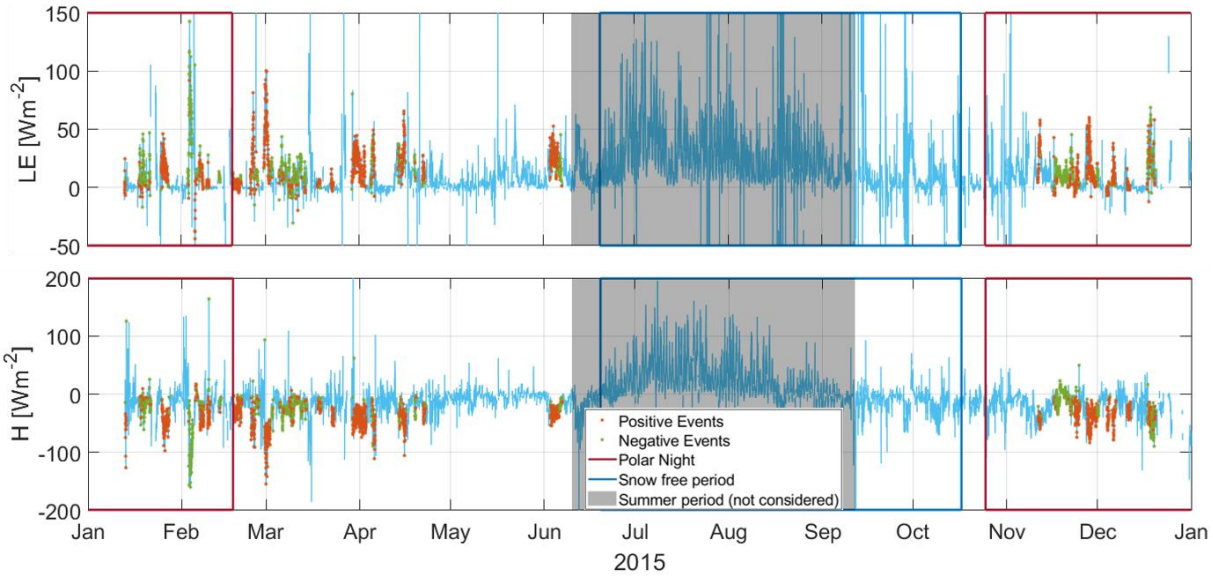

Figure 5.19: The annual cycle of latent and sensible heat flux. Times of positive FCO_2 values during the CO_2 events are marked in red and negative ones in green, respectively.

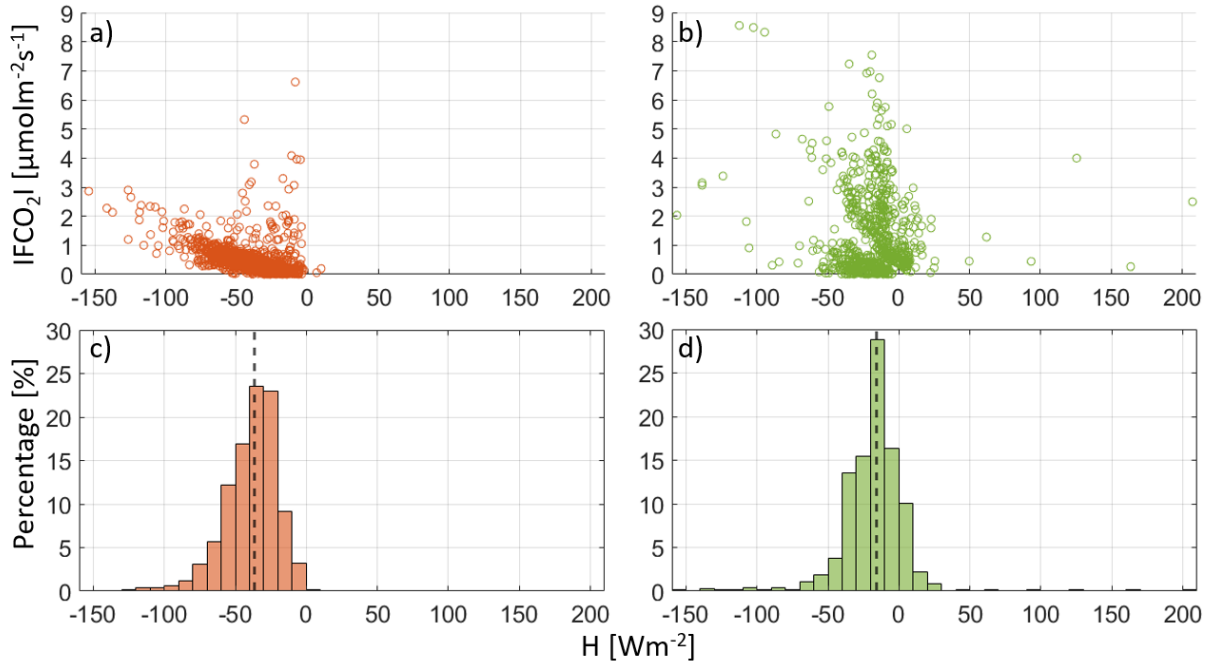

Figure 5.20: Absolute CO_2 flux as a function of sensible heat flux (a, b) and frequency distribution of sensible heat flux classes (c, d) during event times with (a, c) positive and (b, d) negative FCO_2. The dashed line in the histograms marks the respective median value.

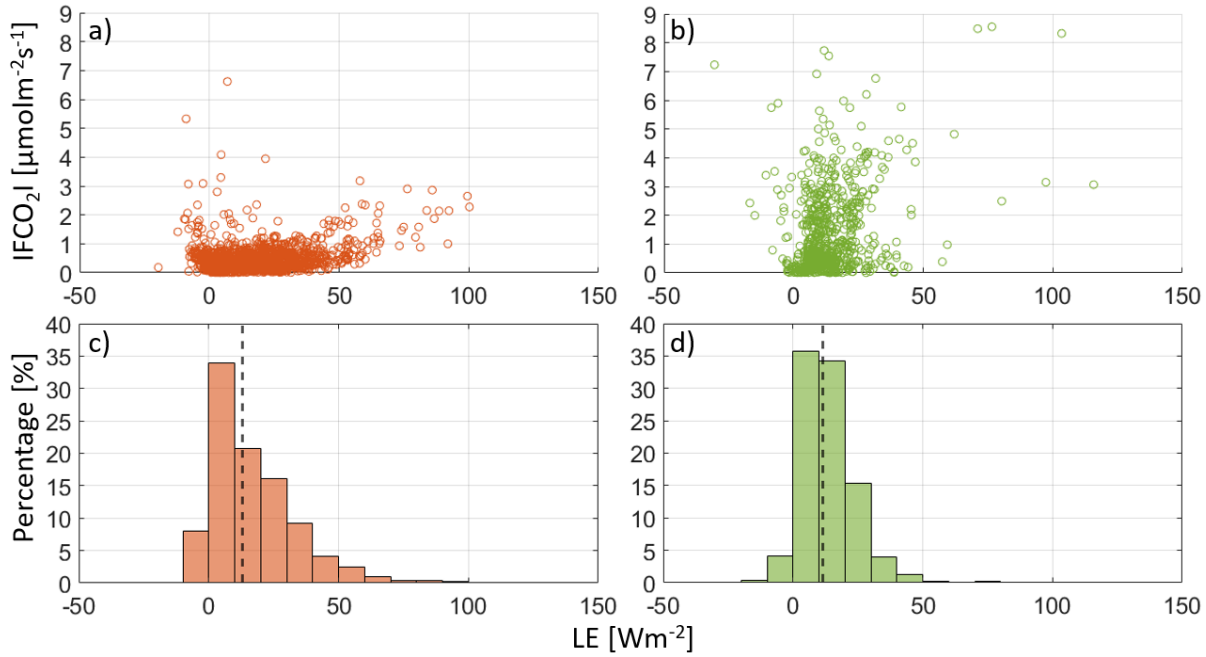

Figure 5.21: Absolute CO_2 flux as a function of latent heat flux (a, b) and frequency distribution of latent heat flux classes (c, d) during event times with (a, c) positive and (b, d) negative FCO_2. The dashed line in the histograms marks the respective median value.

5.3.5 Summary of characteristic meteorological conditions during the events

The FCO_2 events generally occur during distinct changes in atmospheric pressure, air temperature, absolute humidity and longwave radiation, associated with large scale shifts of air masses during the winter months. The most obvious connection is the one between the unusually high absolute CO_2 fluxes and increased wind speeds along the fjord axis, initiating turbulent transport. This also leads to intensified upward latent and downward sensible heat fluxes during the events. No clear differences between the meteorological conditions during

different types of events could be identified. However the negative fluxes during the events most frequently occur during situations of high relative humidity and high incoming and outgoing longwave radiation, resulting in a net longwave radiation close to zero.

5.4 Flux quality during the events

Table 5.4 provides an overview of the significance of various quality criteria during the study period. In order to investigate whether the events are more strongly affected by specific quality issues, the study period is separated into the time outside and during the events. During the events it is moreover distinguished between positive and negative CO_2 fluxes. For most flux criteria a larger share of fluxes outside the events is affected by quality issues than during the events. Exceptions are spikes, skewness and kurtosis of the CO_2 time series as well as absolute limits of the CO_2 concentration and the vertical wind speed. Furthermore negative fluxes during the events are generally much stronger affected by quality issues than positive ones.

Table 5.4: Percentage of quality-flagged CO_2 flux data points during the study period outside the events and during the events, according to different quality criteria. The flux estimates during the events are moreover distinguished according to their sign. Ratios of flagged data exceeding 50 % are marked in red. Quality criteria from top to bottom: Fluxes flags: Overall quality flags for FCO_2, LE and H. Flags are furthermore assigned if the wind direction is between 15° and 55° (wdir) and if the friction velocitiy is below 0.1 ms^{-1} (u* min). Raw data flags: Hard (hf) and soft flags (sf) according to spike test and statistical tests for amplitude resolution (amp res), drop outs, absolute limits (abs lim), skewness and kurtosis (s&k), discontinuities (discont), angle of attack, steadiness of the horizontal wind and CO_2 signal strength, if applicable for CO_2 concentration (CO_2) and vertical wind velocity (w).

Quality criterion	Outside the events	Events	Positive fluxes during events	Negative fluxes during events
FCO_2 hf	18	4	1	10
FCO_2 sf	63	44	41	51
LE hf	16	5	4	6
LE sf	59	43	43	43
H hf	18	4	1	8
H sf	61	41	39	43
wdir	2	0	0	1
u* min	38	2	2	3
spikes CO_2	2	9	4	17
spikes w	0	0	0	0
amp res CO_2	30	17	12	25
amp res w	2	3	2	4
drop out co2	0	0	0	0
drop out w	0	0	0	0
abs lim co2	9	12	5	25
abs lim w	0	2	1	4
s&k co2 hf	22	37	19	68
s&k co2 sf	32	40	23	71
s&k w hf	6	2	1	3
s&k w sf	39	20	15	28
discont CO_2 hf	1	0	0	0
discont CO_2 sf	1	0	0	0
discont w hf	56	11	9	13
discont w sf	70	19	18	22
attack angle	1	0	0	0

stat wind	54	19	15	26
CO_2 sig str hf	13	1	1	0
CO_2 sig str sf	18	2	2	2

5.5 Spectral analysis

In the following section the spectra and cospectra of the vertical wind speed and CO_2 concentration fluctuations will be analyzed. The proportion of noise-contaminated spectra is then used as an additional criterion to evaluate the performance of the anemometer and the gas analyzer in addition to the standard quality flagging policy. The rationale is that if at least one of the spectra of w' or $cCO2$' is affected by excessive noise-contamination, the covariance of the two variables yields unphysical flux estimates, which should be discarded from the time series. According to Kaimal and Finnigan (1994), unacceptably high noise levels usually appear as a rise in the spectrum, approaching a +1 slope and stretching over a decade or more at the high-frequency end, where the spectrum should normally be dropping at a rate of -2/3. Therefore spectra are herein rated as being affected by excessive white noise, if they show an increase in spectral energy between about 1 and 4 Hz as well as between 4 and 10 Hz, representing the major part of the inertial subrange.

In figure 5.22 a all spectra of $cCO2$' during the study period, corresponding to fluxes retained in the filtered time series, are depicted. It is found that 56 % of the spectra are affected by excessive white noise in the inertial subrange. While comparable ratios of 56 % of the fluxes outside the events and 40 % of positive fluxes during the events are strongly affected by white noise, with 90 % the majority of the negative fluxes during the events has to be discarded due to excessive noise contamination. In figure 5.22 b it can be seen that the remaining spectra approximately follow the ideal decline by -2/3 in the inertial subrange up to a non-dimensional frequency of about 10, while white noise affects the majority of the spectra at higher frequencies. The influence of this minor noise contamination at very high frequencies on the final flux estimates is in the following assumed to be negligible. Thus a filtering of the spectra for excessive white noise results in an almost ideal behaviour of the mean spectrum to the right of the spectral peak, which occurs at a frequency of about 0.5. However to its left, the spectral density stays approximately on the level of the spectral peak until a frequency of about 0.05. Towards lower frequencies the individual spectra spread over a wide range and the ensemble mean shows a slight increase until reaching a second maximum at about $3 \cdot 10^{-3}$ on the frequency scale. This indicates a strong overlap of very high frequency turbulent and probably non-local lower frequency contributions, obscuring the spectral gap required for the conventional EC method.

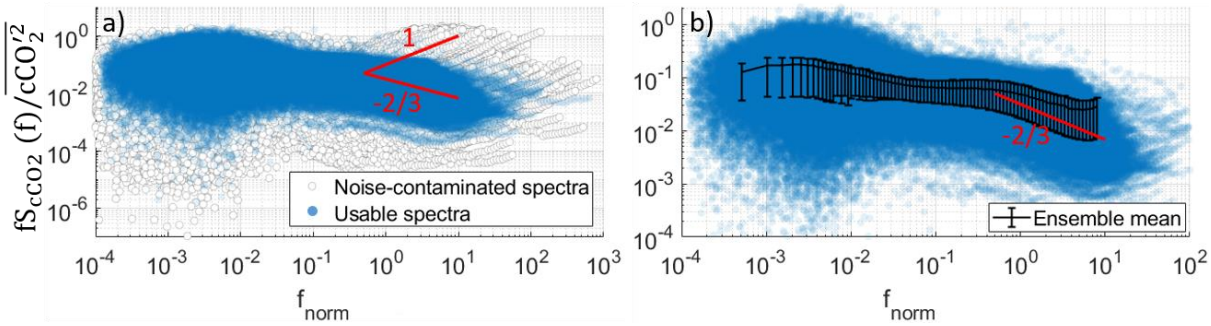

Figure 5.22: (a) All normalized spectra of CO_2 concentration fluctuations corresponding to the fluxes retained for the study period after general quality filtering. The red lines mark the ideal decrease by -2/3 in the inertial subrange as well as the increase by 1, associated with white noise. **(b)** Remaining spectra and their ensemble mean after filtering out noise-contaminated spectra. The error bars show the 25th and 75th percentiles, respectively. By normalizing the spectra by the total variance, all spectra are brought to approximately the same level on the intensity scale. At the same time, the frequency is multiplied by the measurement height and then normalized by the wind speed, so that the spectra coincide in the inertial subrange.

Figure 5.23 a reveals a connection between the proportions of noise-contaminated and usable spectra and the mean wind speed. Between wind speeds of 0 and 3.5 ms^{-1}, the ratio of noise-affected spectra strictly decreases with increasing wind speed. Above the threshold of 3.5 ms^{-1}, the percentage of noise-contaminated spectra increases with increasing wind speed until at wind speeds exceeding 12.5 ms^{-1}, all spectra are discarded due to an unacceptably high noise contribution. This distribution indicates that especially at very low and at very high wind speeds the signal drops below the gas analyzer's noise threshold or the sensor noise rises above signal levels, respectively (Kaimal & Finnigan, 1994). The events, typically occurring at high wind speeds, are thus particularly prone to be affected by white noise. Figures 5.23 b, c and d furthermore explain the enhanced vulnerability of negative events to the impact of white noise, since they predominantly occur during situations where longwave incoming and outgoing radiation approximately balance each other, accompanied by a high relative humidity and oftentimes temperatures close to the freezing point. This problem could be related to the presence of low level clouds or fog, which might lead to riming on the gas analyzer window. However no general decline of CO_2 signal strength is observed under these conditions. Thus it has to be further investigated to what extent small water droplets in the humid air could affect the concentration readings just by drifting through the measurement path.

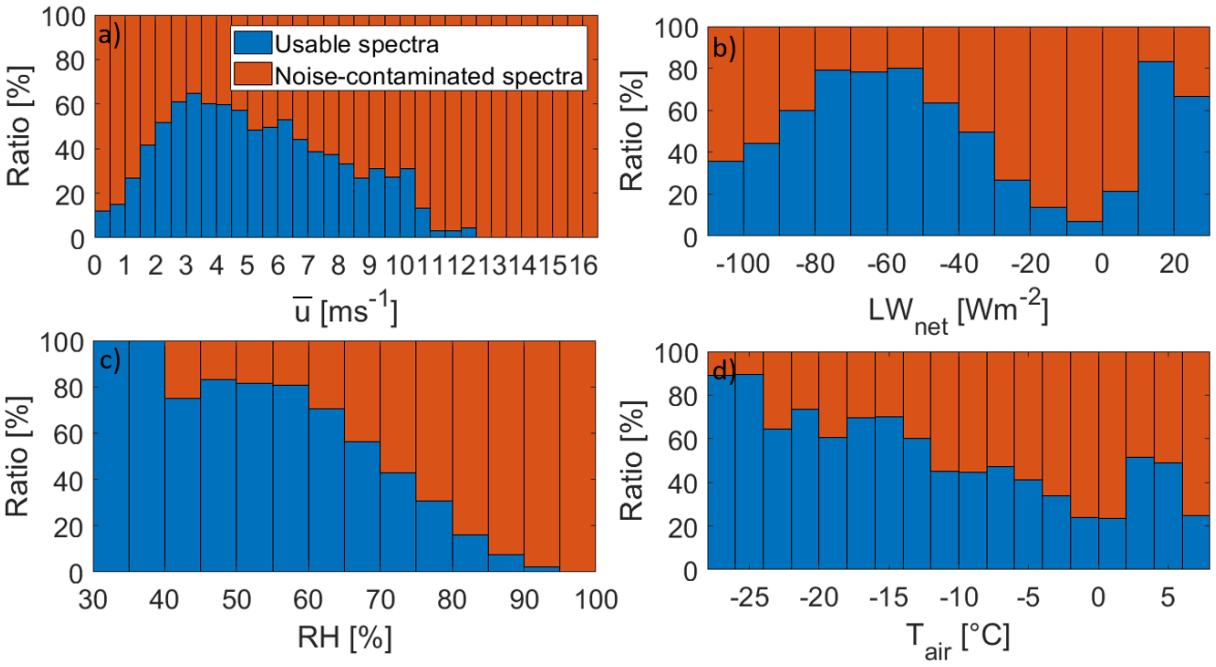

Figure 5.23: Ratio of noise-contaminated versus usable spectra as a function of **(a)** mean wind speed, **(b)** net longwave radiation, **(c)** relative humidity and **(d)** air temperature classes.

Figure 5.24 a shows that the spectra of the vertical wind speed are on the contrary well-defined, featuring an increase in power spectral density in the energy-containing range and a subsequent decrease in the inertial subrange. Only 0.2 % of the spectra are subject to excessive noise contamination, all but one occurring outside the events and all at times where the CO_2 concentration spectrum is noise-contaminated as well.

Figure 5.24 b depicts the cospectra of vertical wind speed and CO_2 concentration fluctuations, which remain after excluding the times where at least one of the power spectra is affected by excessive white noise. In total 56 % of the cospectra were discarded from the study period following this criterion. In the cospectra the characteristics of both spectra are combined: while the cospectrum is well-defined in the inertial subrange, it does not decline towards the lower-frequency end due to the influence of the longwave contributions to the CO_2 concentration fluctuations. Due to the latter, depending on the desired application, either a longer averaging period should be chosen in order to include all influences contributing to the fluxes observed at the study site or a shorter averaging period to effectively exclude non-local influences. To this end the performance of the ogive optimization method as well as the effect of simply adjusting the averaging interval on spectra and flux estimates will be evaluated in the case studies (Section 5.6).

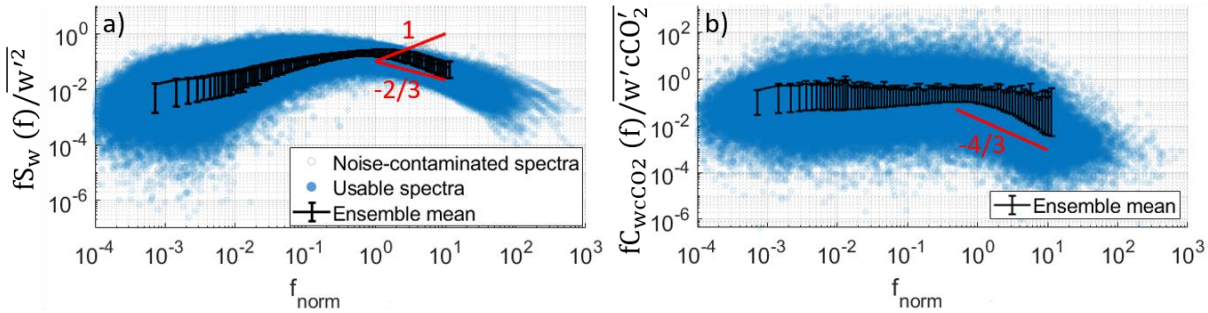

Figure 5.24: (a) All normalized spectra of vertical wind speed fluctuations corresponding to the fluxes retained for the study period after general quality filtering. Noise-contaminated spectra are excluded from the ensemble mean. **(b)** Remaining cospectra and their ensemble mean, when excluding all times, where at least one of the spectra is affected by excessive white noise. See figure 5.22 for further information on the illustration.

Figures 5.25 a to c depict the power spectra of w' and $cCO2$' as well as their cospectrum as a function of the natural frequency instead of the normalized frequency. By averaging over wind speed classes, the dependency of the behaviour of the spectra and cospectra on the wind speed can thus be illustrated. Generally a shift of the (co)spectral peak to higher frequencies and higher (co)spectral densities as well as a decrease of low-frequency influence can be observed with increasing wind speed. The former might lead to the fact that the very high-frequency fluctuations, dominating the (co)spectra at high wind speeds, cannot be resolved by the gas analyser under certain circumstances, leading to white noise. Furthermore an irregular peak in the CO_2 spectrum appears between frequencies of about 3 and 4 Hz, which gains importance as the wind speed increases. Further investigations would be necessary to explain the origin of this artefact.

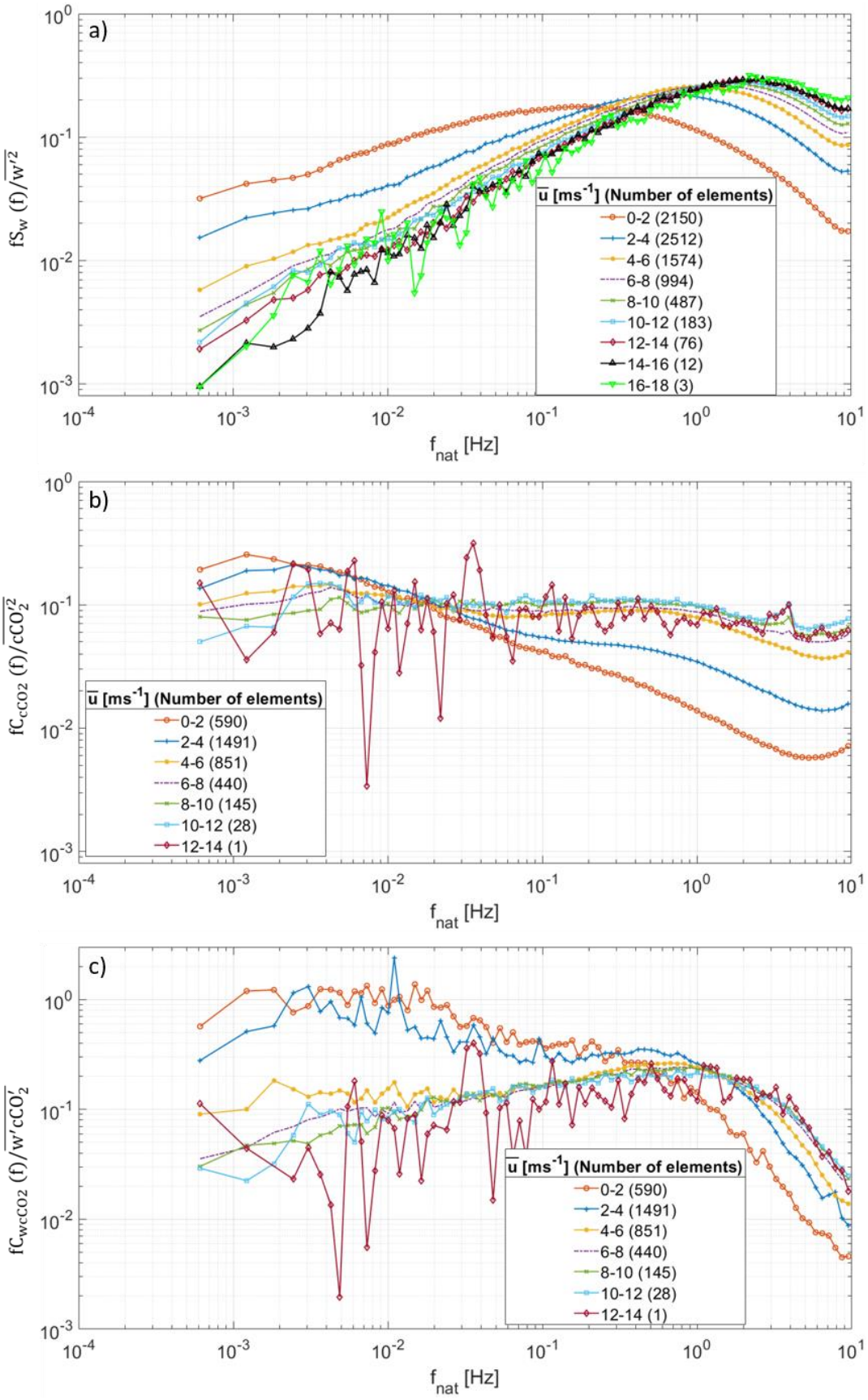

Figure 5.25: Average behaviour of all **(a)** w', **(b)** cCO_2' spectra and **(c)** cospectra, excluding the ones strongly affected by white noise, for different classes of mean wind speed. In the legend the number of spectra inside the respective wind speed class is given in parentheses.

5.6 Case studies

In the following chapter two individual events will be analysed in great detail. With the aim of representing a major part of the detected events, two events with very different characteristics were chosen for these case studies. Both case studies start with a detailed analysis of the event characteristics and meteorological, snow and soil conditions during, as well as shortly before and after the event. Subsequently the quality of the individual flux estimates is discussed. A methodological section then makes suggestions on how the detected quality issues could be prevented and quantifies the sensitivity of the flux estimates to methodological adjustments. This section intends to identify possible methodological explanations for the specific flux events. Finally the possible contribution of physical drivers will be estimated in order to quantify their explanatory power with respect to still unexplained flux behaviour.

5.6.1 A negative single peak event

The following section involves a detailed analysis of a negative single peak event, observed during the snow covered period but outside the polar night. The event starts at 21:30 UTC on March 2, persist for about nine hours over the night and abates around sunrise at 7:00 on March 3. During the event negative fluxes reach values of up to -2.69 $\mu molm^{-2}s^{-1}$ and amount to a total net uptake of -0.50 gCm^{-2} (Figure 5.26).

The case study follows the general structure outlined above. Furthermore this event is used to exemplary evaluate the performance of the time lag detection algorithm.

5.6.1.1 Meteorological, soil and snow conditions during the event

In figure 5.26 an overview is given over the development of meteorological, soil and snow conditions between five hours before the beginning and five hours after the end the event. The meteorological conditions are primarily determined by the passage of an occluded front originating from a low pressure system located between Iceland and Svalbard in the early morning of March 3 (Figure 5.27). Before the frontal passage the atmospheric pressure decreases by 6 hPa starting 9.5 h before the beginning of the events. With the passage of the front it reaches its minimum of 985 hPa at about 5 UTC and increases afterwards by 13 hPa until 25.5 hours after the end of the event. After a slight decrease by 0.7 °C during the first hours of the event, the air temperature increases by 1.8 °C to a maximum, attained simultaneously with the minimum in atmospheric pressure. The temperature decrease after the frontal passage is interrupted by the sunrise, which is indicated by the steep rise in incoming shortwave radiation at the end of the event. Simultaneously with the temperature increase there is a rise in absolute humidity, indicating the advection of warm, moist air mass from the south. This hypothesis is supported by the south-easterly wind direction both at 500 and 850 hPa, which changes to a southerly direction between 0 and 6 UTC on March 3. Close to the ground the wind is channelled to a more easterly direction and turns to south with a decrease in wind speed at the end of the event. The wind speed starts to increase 5 hours before the beginning of the event, stays at an average maximum level of about 8 ms^{-1} during most of the event with peak values of more than of 15 ms^{-1}. After the passage of the front the wind speed abates to a low level of about 2 ms^{-1} at the end of the event. The high wind speeds during the event trigger mechanical turbulence which is revealed in an increased friction

velocity and breaks up the mostly stable atmospheric stratification observed prior to event. Thus an enhanced exchange of heat and water vapour is enabled, showing itself in amplified absolute sensible and latent heat fluxes by on average about 20 Wm^{-2}. During the event the net longwave radiation stays at a low level of -10 Wm^{-2}. This reduction in radiative cooling could be related to the presence of low level clouds, while the further decrease to values around zero is related to the formation of fog between 7 and 8 UTC, associated with a further increase in absolute humidity (Figure 5.28). The atmospheric CO_2 concentration decreases by about 0.5 $mmolm^{-3}$ during the event. Except for a slight increase of the temperature in the upper soil levels following the rise in atmospheric temperature, no significant changes in soil and snow properties occur during the event.

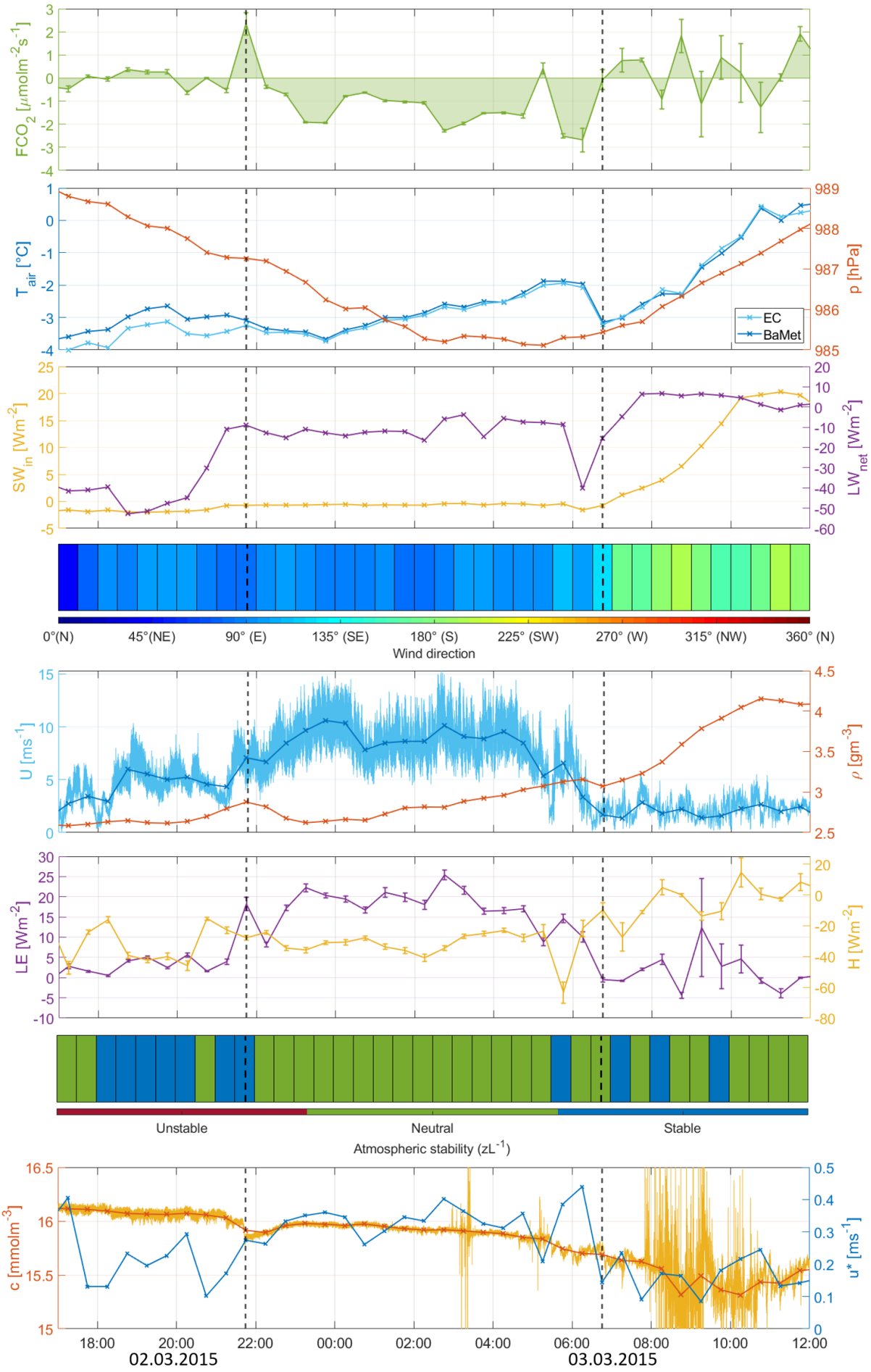
FCO2 [μmolm-2s-1]
Tair [°C]
p [hPa]
EC
BaMet
SWin [Wm-2]
LWnet [Wm-2]
0°(N)
45°(NE)
90° (E)
135° (SE)
180° (S)
225° (SW)
270° (W)
315° (NW)
360° (N)
Wind direction
U [ms-1]
ρ [gm-3]
LE [Wm-2]
H [Wm-2]
Unstable
Neutral
Stable
Atmospheric stability (zL-1)
c [mmolm-3]
u* [ms-1]
18:00
20:00
22:00
00:00
02:00
04:00
06:00
08:00
10:00
12:00
02.03.2015
03.03.2015

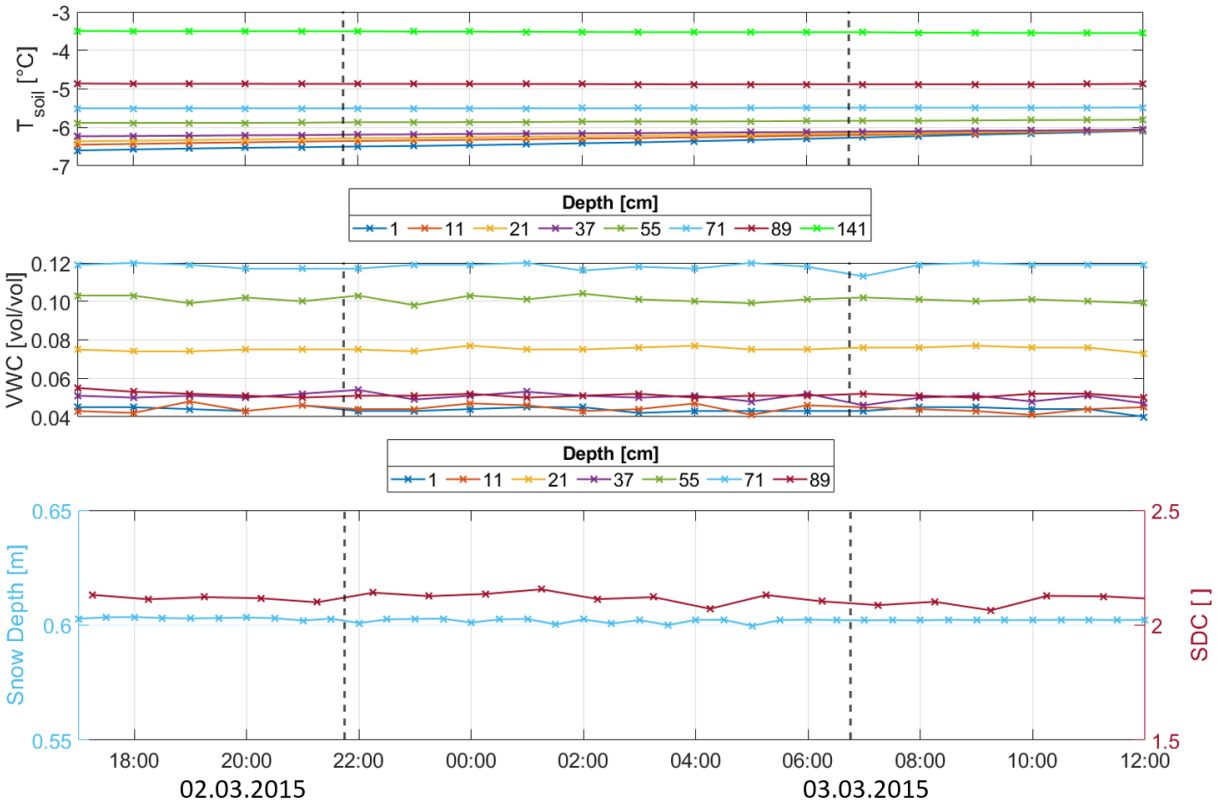

Figure 5.26: Overview of the development of meteorological, soil and snow conditions during the event. The beginning and the end of the event are marked by the dashed lines. The illustration includes the CO_2 flux and its random error, the air temperature at 2 m (as recorded at the EC tower and the meteorological Bayelva station (BaMet)), atmospheric pressure, shortwave incoming and longwave net radiation. The direction of the radiation is defined inversely to the one of the surface flux, according to the convention, with negative radiation values indicating that the surface loses energy to the atmosphere and vice versa. Furthermore depicted are the wind direction, average (30 min) and raw (20 Hz) wind speed, absolute humidity, latent and sensible heat flux, atmospheric stability, average and raw atmospheric CO_2 concentration, friction velocity, soil temperature and soil volumetric water content (VWC) at various depths, snow depth and snow dielectric constant (SDC).

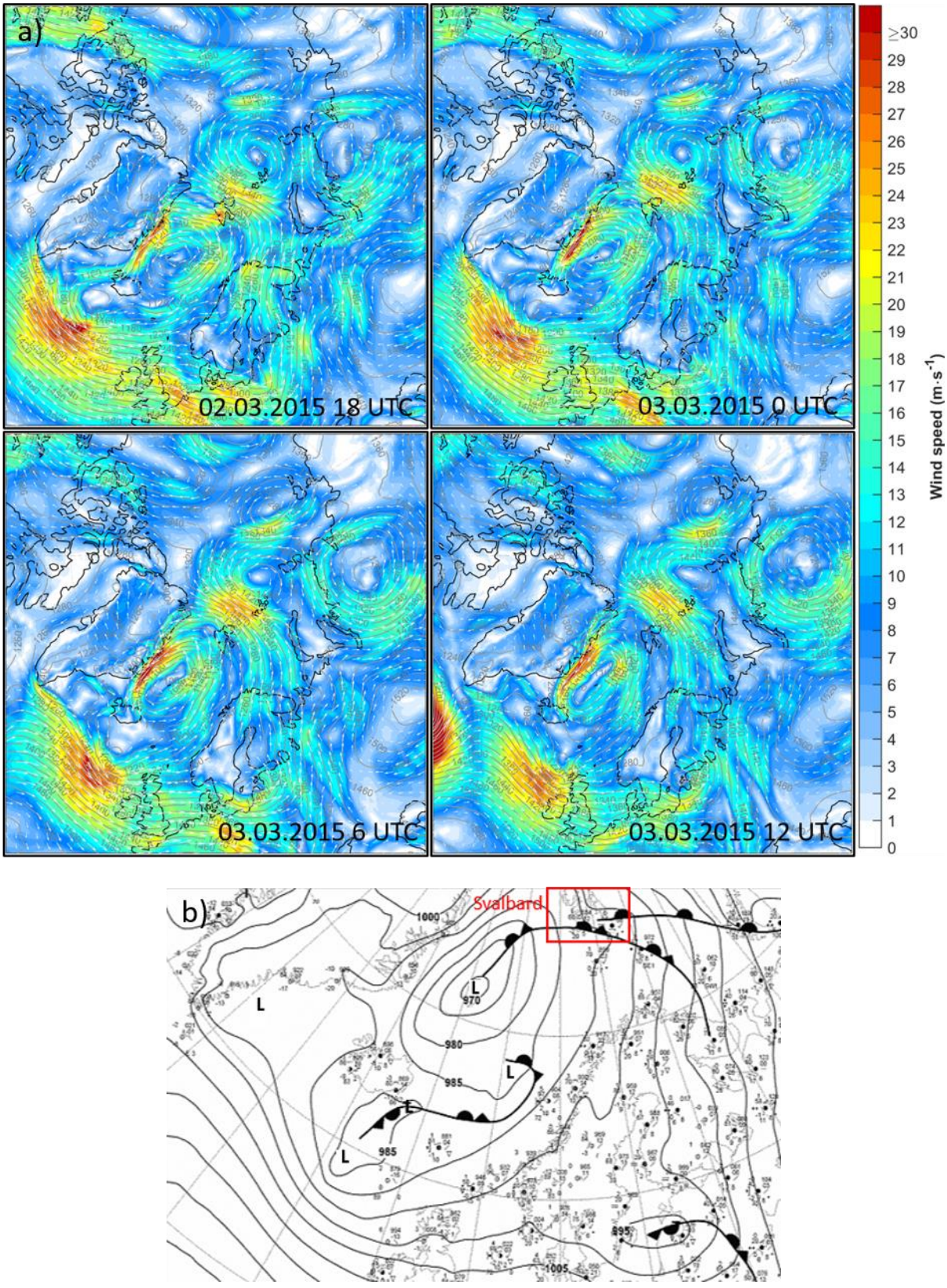

Figure 5.27: Synoptic situation during the event. **(a)** ERA5 geopotential height (contour lines) and horizontal wind speed (colors) and direction (arrows) at the 850 hPa level. The data was obtained from the Climate Data Store (https://cds.climate.copernicus.eu/cdsapp#!/home). **(b)** Surface analysis for 6 UTC on 3 March (DWD, 2015). The contour lines indicate the pressure at ground level.

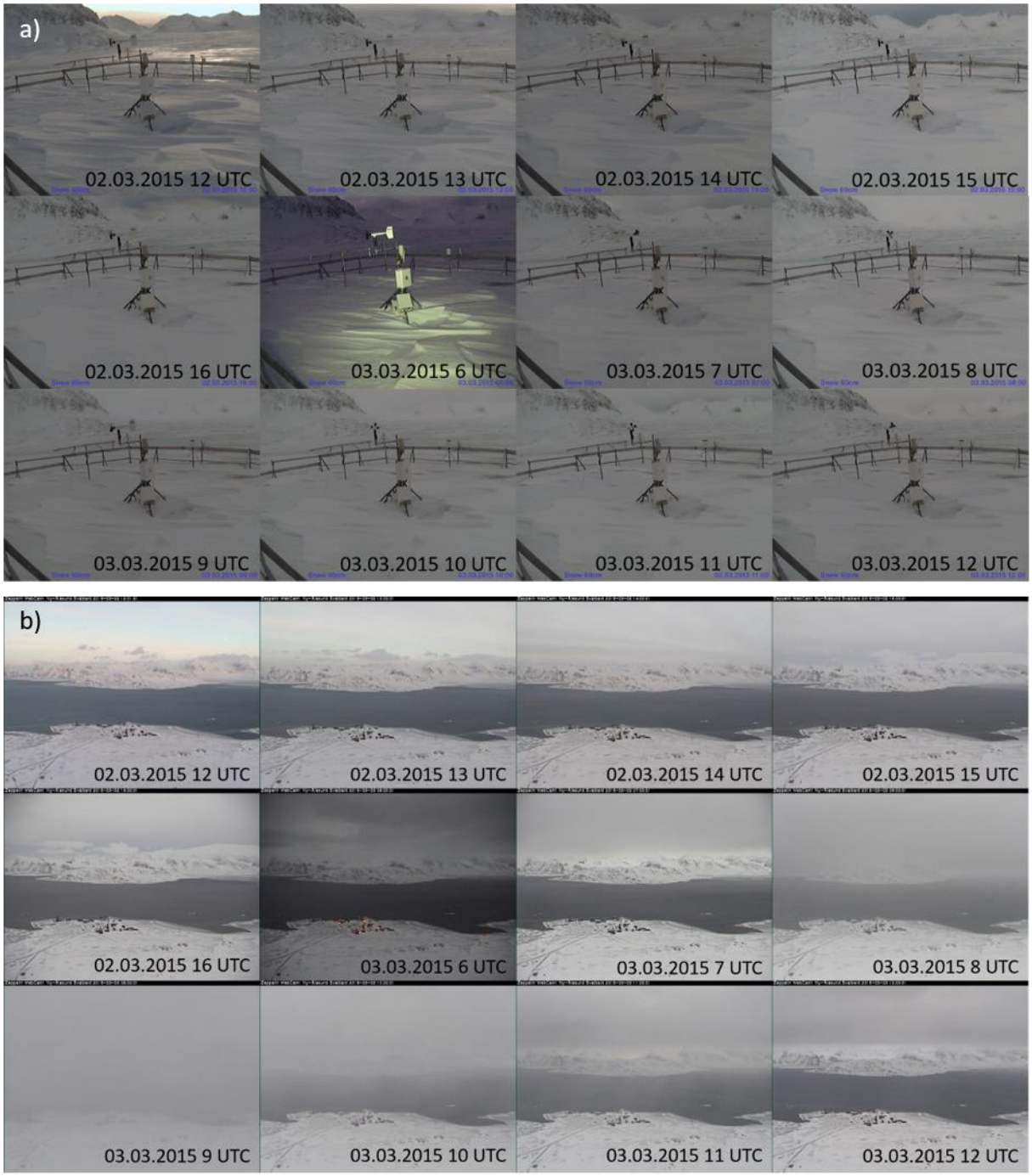

Figure 5.28: Pictures of **(a)** the Bayelva weather station obtained from an automatic camera, taking pictures every hour and run by AWI and **(b)** Ny Ålesund from the automatic webcam on the Zeppelin Mountain (Pedersen, 2013).

5.6.1.2 Quality assessment

Figure 5.29 provides an overview of quality issues arising during the event. Between the beginning and the end of the event, only one flux estimate is hard-flagged according to the overall flagging system by Foken and Mauder (2004) related to instationarity of the CO_2 concentration time series. The remaining flux estimates would thus typically be included in long-term studies and annual budget calculations. However many more flux estimates are affected by serious quality issues, which should not be ignored. Most importantly, 76 % of the

CO_2 spectra during the event are subject to an unacceptably high noise level, which is also indicated by the hard flags assigned for an insufficient amplitude resolution.

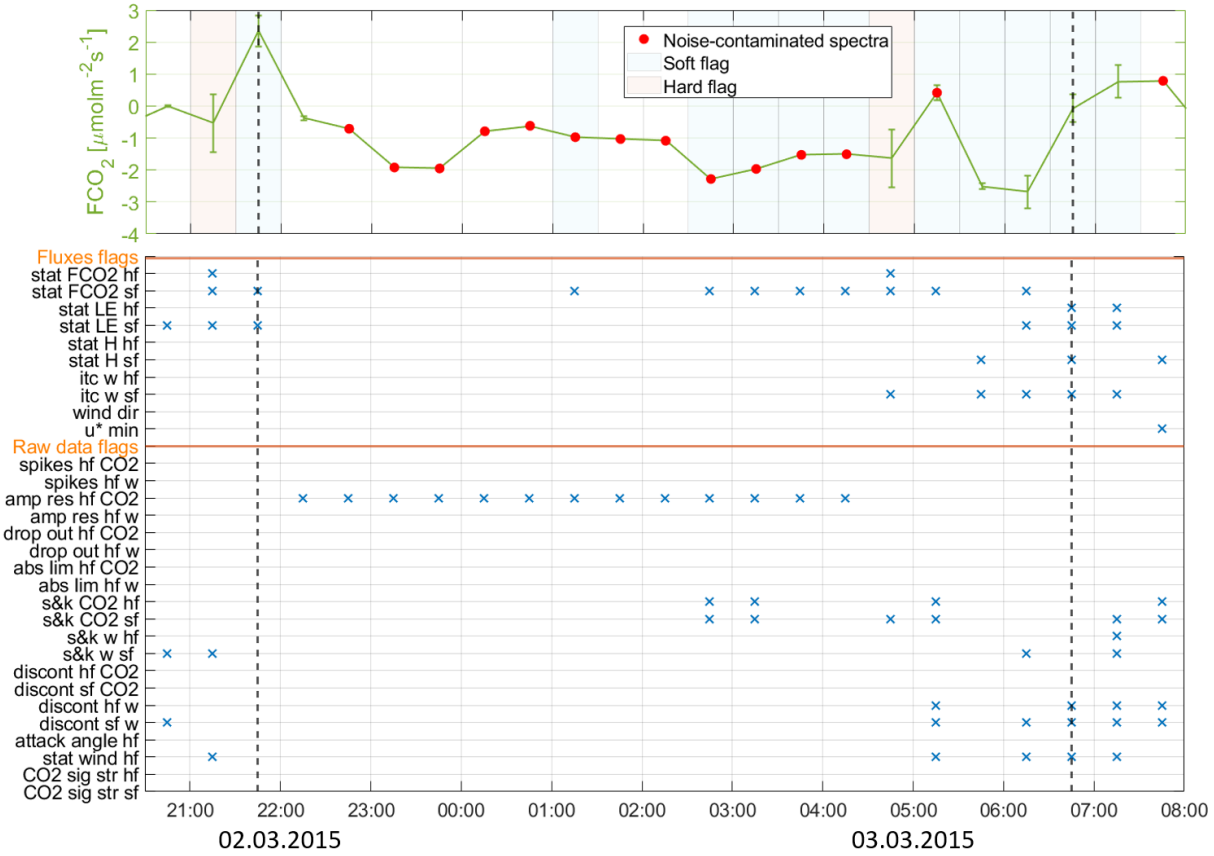

Figure 5.29: Top: CO_2 flux time series between two hours before and two hours after the event. Averaging intervals where the CO_2 flux is hard or soft flagged according to the flagging policies after Foken and Mauder (2004) are shaded red and blue, respectively. Red points mark fluxes, retained after standard quality filtering, at times where spectra are affected by excessive white noise. **Bottom:** From top to bottom: Fluxes flags: Details on steady state (stat) and developed turbulence test (itc) for FCO_2, LE and H. Flags are furthermore assigned if the wind direction is between 15° and 55° (wdir) and if the friction velocitiy is below 0.1 ms^{-1} (u* min). Raw data flags: Hard (hf) and soft flags (sf) according to spike test and statistical tests for amplitude resolution (amp res), drop outs, absolute limits (abs lim), skewness and kurtosis (s&k), discontinuities (discont), angle of attack, steadiness of horizontal wind and CO_2 signal strength, if applicable, for CO_2 concentration (CO_2) and vertical wind velocity (w). In both figures dashed lines mark the beginning and the end of the event.

5.6.1.3 Methodology of the event

Vascular plants have been found to photosynthesize until below -3 °C under the snow (Bate and Smith, 1983) and lichens and mosses even down to below -10 °C under the snow (Sveinbjörnsson and Oechel, 1981; Walton and Doake, 1987; Kappen, 1993). Nonetheless I consider it highly unlikely that the large uptake event under 60 cm of snow, during the night, where photosynthesis is not stimulated by solar irradiation, could be related to biotic uptake. Most of all, since mechanisms controlling night fluxes are normally solely linked to plant and soil respiration, there should generally be no dependence between CO_2 fluxes and wind speed or friction velocity (Aubinet et al., 2012). The possibility that such a relationship is induced by pressure pumping will be investigated in section 5.6.1.3.3. Furthermore no significant changes in soil or snow properties were observed during the event. Thus there would be no reason for

a sudden solution of CO_2 in meltwater or unfrozen pore water in the soil. This renders it likely that the negative event is caused by methodological rather than physical particularities.

This section hence aims to explain how the observed consistently negative fluxes, which together show the typical sequence of a negative peak event, originate from the strongly noise-affected CO_2 concentration signal. Furthermore it will be investigated if the methodology can also explain the few negative fluxes during the event that at first sight are not subject to significant quality issues.

First of all this case study is used to exemplarily evaluate the performance of the fully automatic time lag detection. Subsequently an overview of the sensitivity of the flux estimates to changes in flux correction and computation methods will be given in section 5.6.1.3.2, including several subsections discussing the most relevant methodological implications. After a brief investigation of the possible physical effect of pressure pumping, conclusions will be drawn from the findings of this case study in section 5.6.3.4.

5.6.1.3.1 Time lags

Visual inspection of the time lags, applied to synchronize the raw w and CO_2 concentration time series, reveals that the delay, determined via covariance maximization, at times varies unrealistically (Figure 5.30 a). The problem is that at low absolute covariance, secondary cross-covariance optima might hinder the detection of the actual time lag (Pirk et al. 2017) which often results in flux overestimations (LI-COR Inc., 2020).

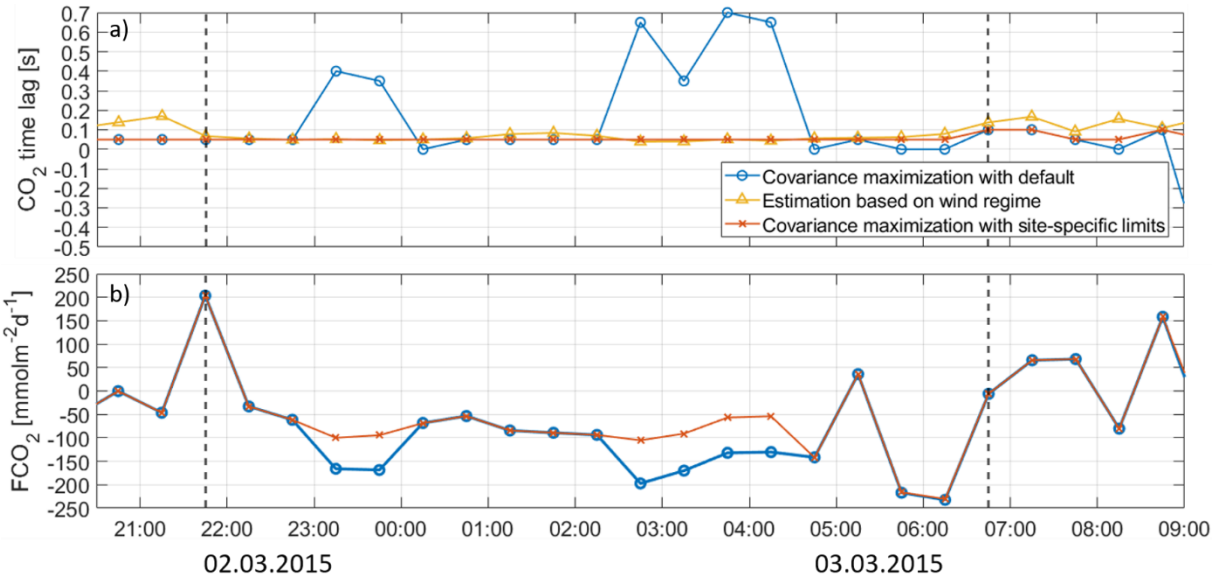

Figure 5.30: (a) Time lags used to synchronize the raw CO_2 time series with the anemometric measurements using covariance maximization with default or site-specific limits between one hour before and two hours after the CO_2 flux event with a resolution of 0.05 s. Also shown are the time lags estimated based on current wind speed and direction. **(b)** Resulting CO_2 fluxes applying either method.

Therefore typical, minimum and maximum expected time lags are in the following estimated based on the specific instrument setup at the Bayelva site as well as the wind speeds and directions during the event in order to narrow down the range of plausible time lags. For each averaging period the projection of the mean wind vector onto the imaginary line connecting the respective path middle of anemometer and gas analyser, given the horizontal sensor separation of 0.22 m, is used to calculate the expected time delay between the instruments

(Figure 5.31). The resultant mean, maximum and minimum values during the event are then employed as default value and limits for the covariance maximization.

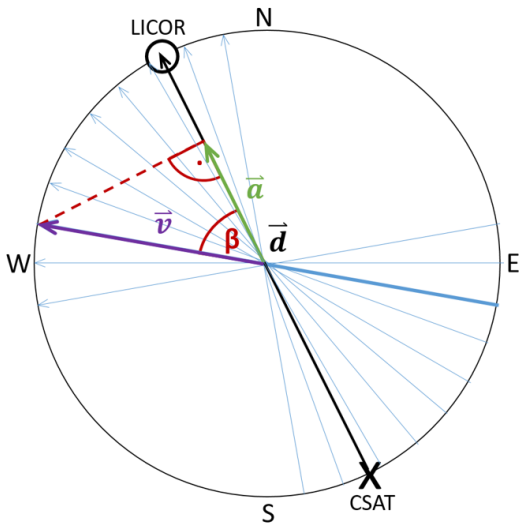

$$time\ lag = \frac{|\vec{d}|}{|\vec{a}|}$$

with

$$|\vec{a}| = |\vec{v}|\cos(\beta)$$

$$\beta = i \cdot |dir(\vec{d}) - wdir + 180°|$$

$$i = \begin{cases} -1\ if dir(\vec{d}) - 90° < wdir < dir(\vec{d}) + 90° - 360° \\ 1\ if\ dir(\vec{d}) + 90° - 360° < wdir < dir(\vec{d}) - 90° \end{cases}$$

$$dir(\vec{d}) = 333°$$

$$|\vec{d}| = 0.22\ m$$

Figure 5.31: Calculation scheme of the expected time lag between gas analyser and anemometer measurements for each averaging period, given the direction wdir and wind speed $|\vec{v}|$ of the mean horizontal wind vector $\vec{v}$, as well as the length $|\vec{d}|$ and direction $dir(\vec{d})$ of the hypothetic line connecting the middles of the measurement paths of anemometer (CSAT) and gas analyser (LICOR). The blue arrows show the range of wind directions observed during the event. Positive time lags correspond to times where the anemometer is reached first by the wind field and vice versa.

Figure 5.30 compares the final time lags resulting from either method. All formerly unrealistic time lags are eliminated by setting site-specific limits to the covariance maximization. Considering reasonable site-specific time lags reduces the unexpected total apparent CO_2 uptake during the event by 0.12 gCm^{-2}, that is 24 % of the original net uptake. Since in this example all of the fluxes affected by an unrealistic time lag are already rated as unphysical due to noise-contamination of the spectra, the time lag correction is not very meaningful in this case. Nonetheless the time series based on time lags adjusted to the site conditions, from now on serves as a baseline run for the further investigations. Furthermore the significant change in the final flux estimates, which is at times introduced by adjusting the time lags, reveals the general importance of assessing the plausibility of the delay times derived from the covariance maximization method. Thus the method described in this section will also be used in the second case study to determine a site- and wind-specific time lag.

Besides, this time lag detection technique is more similar to the one implemented in the OOT, leading to a reduced deviation of the fluxes obtained from EddyPro and OOT when using the conventional EC method.

5.6.1.3.2 Sensitivity of the event fluxes to methodological changes

Figure 5.32 illustrates the influence of different corrections and computation methods on the resulting flux estimates during the given negative peak event. In order to quantify the sensitivity of the final fluxes to methodological changes, single adjustments are made compared to the standard settings used for the entire study period (section 4.2.1), while all other settings are maintained.

The effects of the individual modifications are listed in table 5.5. Together, all corrections applied in the base run lead to an average downward shift of the time series by -1.25 $\mu molm^{-2}s^{-1}$ compared to the uncorrected fluxes, changing the total CO_2 exchange during the event from a net release of 0.08 gCm^{-2} to a net uptake of -0.38 gCm^{-2}. This shift to the negative range is caused by the WPL correction, which, in the absence of other corrections would lead to an even larger average flux reduction of -1.30 $\mu molm^{-2}s^{-1}$ (Details in section 5.6.1.3.2.1).

Changes to the baseline run settings slightly counteract this large downward shift introduced by the WPL correction, featuring a reduction of the net uptake by 37 % when applying planar fit instead of double rotation, by 42 % when upscaling fluxes calculated for one minute averaging intervals to periods of 30 minutes and by 26 % when accounting for possible instrument self-heating.

While details on the former two adjustments are outlined sections 5.6.1.3.2.4 and 5.6.1.3.2.3 respectively, the latter should not play a role, considering the instrumentation at the Bayelva site (section 4.2.1.2.2). Nonetheless its effect is briefly discussed for the sake of completeness, since the correction is controversially debated and not applying it was the main point of criticism regarding the interpretation of negative flux events by Lüers et al. (2014). However figure 5.32 confirms that even if instrument self-heating took place, its effect would be well beyond a level that could explain the peculiar negative CO_2 fluxes. This is despite the fact that correction factors might well be overestimated already due to erroneously assuming a vertical orientation of the gas analyzer. Furthermore the negative flux events without exception occur at high wind speeds, where heat is more effectively removed from the sensor surface, which further reduces the influence of instrument self-heating (Burba et al., 2008). In the second case study it is therefore not considered as a possible explanation for the event fluxes anymore.

Using the OOT instead of EddyPro for flux calculation, does not have a significant impact on the net CO_2 exchange during the event. Instead the fluxes derived from the OOT fluctuate around the baseline run, mostly irrespective of whether applying the ogive optimization technique or the conventional EC method. The deviations between the results obtained from either flux processing software should thus largely be related to minor differences in time lag correction and coordinate rotation schemes. The ogive optimization results are discussed in detail in section (5.6.1.3.2.2).

From the small deviation between uncorrected fluxes and the ones obtained without WPL correction, it can be seen that spectral corrections bear only a negligible influence on the final fluxes estimates during the event. Thus they will not be further investigated at this point.

All in all most deviations from the baseline settings introduce a shift in the flux estimates which exceeds the range of random uncertainty due to sampling errors. Nonetheless, taking into account the manifold other sources of uncertainty, the individual time series correspond surprisingly well.

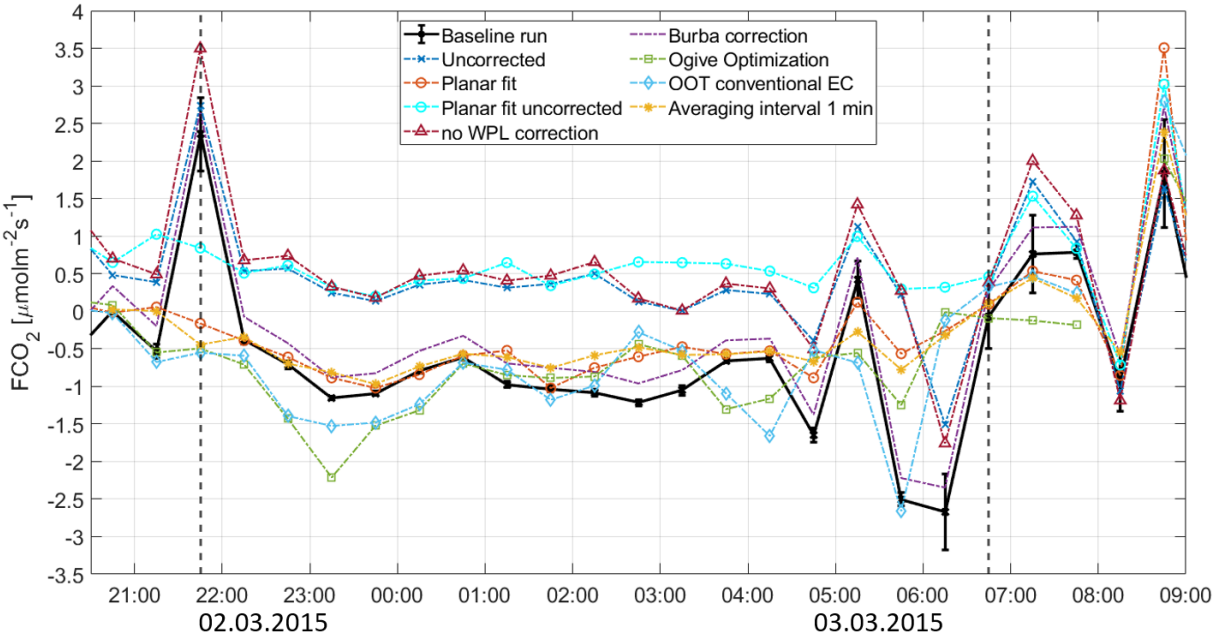

Figure 5.32: CO_2 fluxes resulting from applying different corrections and computation methods. The settings applied for the whole one year time series as described in section 4.2.1 with adjusted time lag detection are denoted as baseline run. The error bars display the associated random uncertainty due to sampling errors. The uncorrected fluxes are the ones obtained prior to WPL and spectral corrections. Fluxes labelled OOT conventional EC show the results obtained from the ogive optimization toolbox when using the conventional eddy covariance method with averaging intervals of 30 minutes. Fluxes obtained using an averaging interval of one minute are averaged to the 30 minute intervals.

Table 5.5: Overview of the net CO_2 exchange during the event and the absolute and relative average deviation of the individual flux estimates from the base run for the different correction and computation methods.

Computation method	Total net CO_2 exchange during the event [gCm^{-2}] and deviation from the baseline run ([%])	Mean deviation of the individual flux estimates from the baseline run [$\mu molm^{-2}s^{-1}$] ([%])
Baseline run	-0.38	
Planar fit	-0.24 (+37)	+0.39 (+27)
1 min averaging interval	-0.22 (+42)	+0.44 (+21)
Burba correction	-0.28 (+26)	+0.28 (+69)
Ogive optimization	-0.36 (+5)	+0.08 (-26)
OOT conventional EC	-0.38 (0)	+0.02 (-28)
uncorrected	0.08 (+121)	+1.25 (+134)
without WPL correction	0.10 (+126)	+1.33 (+147)

5.6.1.3.2.1 WPL correction

The WPL correction is to a large extent responsible for the negative fluxes observed during the event. Generally, if H and LE have the same magnitude, H affects the final WPL term about five times as much as LE (Webb et al., 1980). In addition to that, the magnitude of LE is on average about half the one of H during the event (Figure 5.26). Thus the positive LE reduces the impact of the negative H on the final WPL term by less than 8 % (Figure 5.33). Therefore the negative peak event in sensible heat fluxes is largely imprinted on the sequence of mostly slightly positive raw CO_2 fluxes affected by serious high-frequency noise. In order to validate the sensible heat fluxes obtained from the EC method, they are additionally estimated using the bulk approach (Figure 5.34). When using the measurements from the EC system as input data, both methods correspond surprisingly well. Employing the data obtained at the

meteorological station results in a slightly larger negative sensible heat flux. This pattern can generally be observed during the FCO_2 events. Hence a serious overestimation of the absolute WPL term as a consequence of an overestimation of the negative sensible heat flux can most likely be excluded.

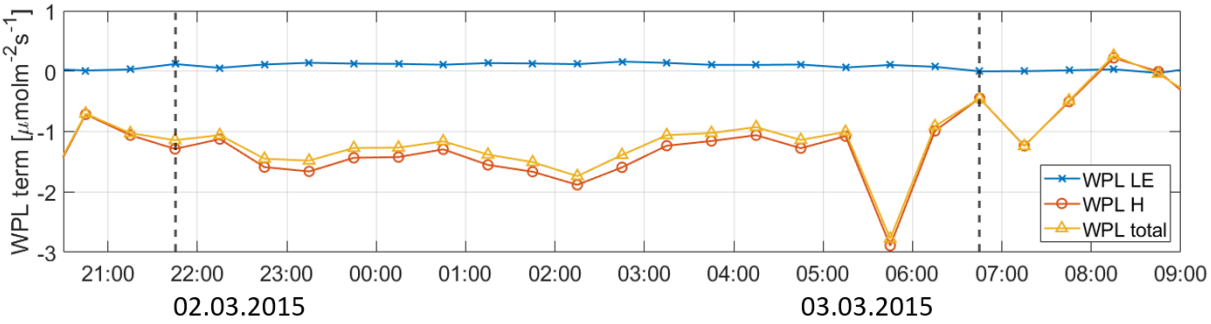

Figure 5.33: Contribution of the water dilution term (WPL LE) and the thermal expansion term (WPL H) to the total WPL correction.

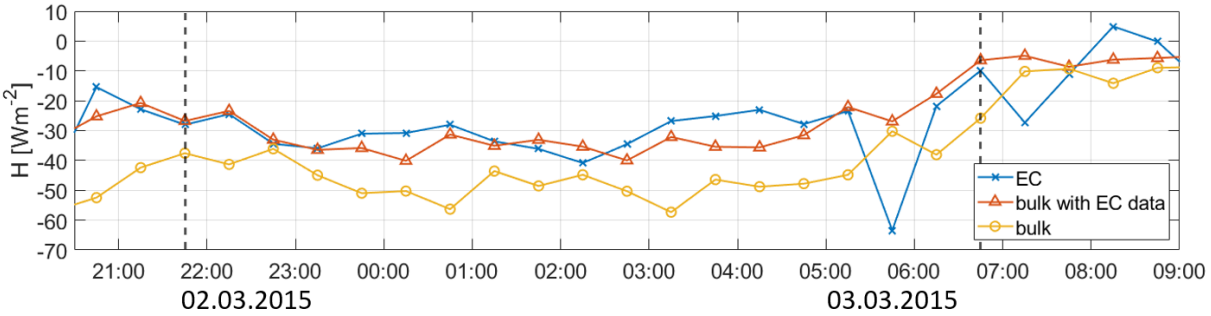

Figure 5.34: Sensible heat fluxes during the event as obtained from the EC method and the bulk method using the data recorded at the EC system (bulk with EC data) and at the Bayelva meteorological station (bulk).

Since the strongly negative sensible heat fluxes are triggered by the high wind speeds, the WPL correction induces the positive correlation observed between absolute CO_2 fluxes and wind speed or friction velocity, respectively (Figure 5.35). The negative correlation between CO_2 fluxes and wind speed prior to the WPL correction could possibly be related to a non-negligible contribution of pressure fluctuations which are not accounted for by the classical WPL terms. The generally negative pressure flux, which is strongly correlated with friction velocity (Zhang et al., 2011), could thus result in an overestimation of the downward CO_2 flux. For a mixed forest in a Chinese mountain region, Zhang et al. (2011) found the pressure correction term to reach values of up to 0.8 $\mu molm^{-2}s^{-1}$ in its ensemble average diurnal course during the winter time. Although they expect the pressure flux to be much smaller at low-vegetation sites, it might nonetheless bear a non-negligible influence on the low absolute Arctic flux estimates. In order to investigate this effect in further detail, reliable high frequency pressure measurements would be needed.

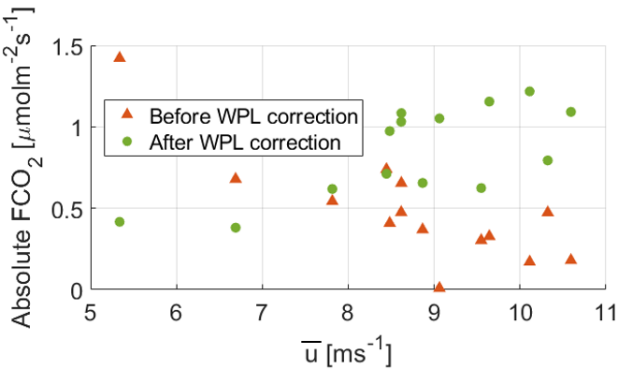

Figure 5.35: Correlation between wind speed and CO_2 fluxes at event times that are flagged for an insufficient amplitude resolution of the CO_2 concentration.

Figure 5.33 furthermore reveals that the large negative CO_2 flux between 5:30 and 6:00 UTC is caused by the transfer of a negative peak in H to the CO_2 flux time series via the WPL correction. This is likely caused by a strong low-frequency influence on the cospectrum of vertical wind speed and temperature fluctuations. Figure 5.36 illustrates how the ogive optimization removes this non-local contribution by reducing the averaging time to about 10 minutes. Furthermore a high-frequency dampening relative to the ideal decrease of the cospectrum by -4/3 in the inertial subrange is visible. For this reason the high-frequency bound on the optimization is shifted towards lower frequencies in order to avoid the influence of the dampened frequencies. Together both adjustment results in a reduction of the negative sensible heat flux by 8 Wm^{-2}.

With the remaining sensible heat flux of 30 Wm^{-2} the total WPL term is reduced by 45 % compared to the original EddyPro estimate of -60 Wm^{-2}. However since the positive water dilution term is also overestimated when using the conventional EC method due to a significant low-frequency contribution also to the latent heat flux, the effective reduction of the total WPL term is slightly lower. Nonetheless the net reduction of the WPL term due to the exclusion of low-frequency influences on sensible and latent heat fluxes contributes to the lower CO_2 flux magnitude obtained from the ogive optimization compared to the conventional EC method. This is an example of how, under low-flux conditions, where the WPL terms frequently exceed the raw gas fluxes, errors may propagate directly from the energy fluxes to the CO_2 fluxes via the WPL correction. It underlines the importance of thoroughly considering quality issues also in the energy fluxes when evaluating the usability of CO_2 flux estimates.

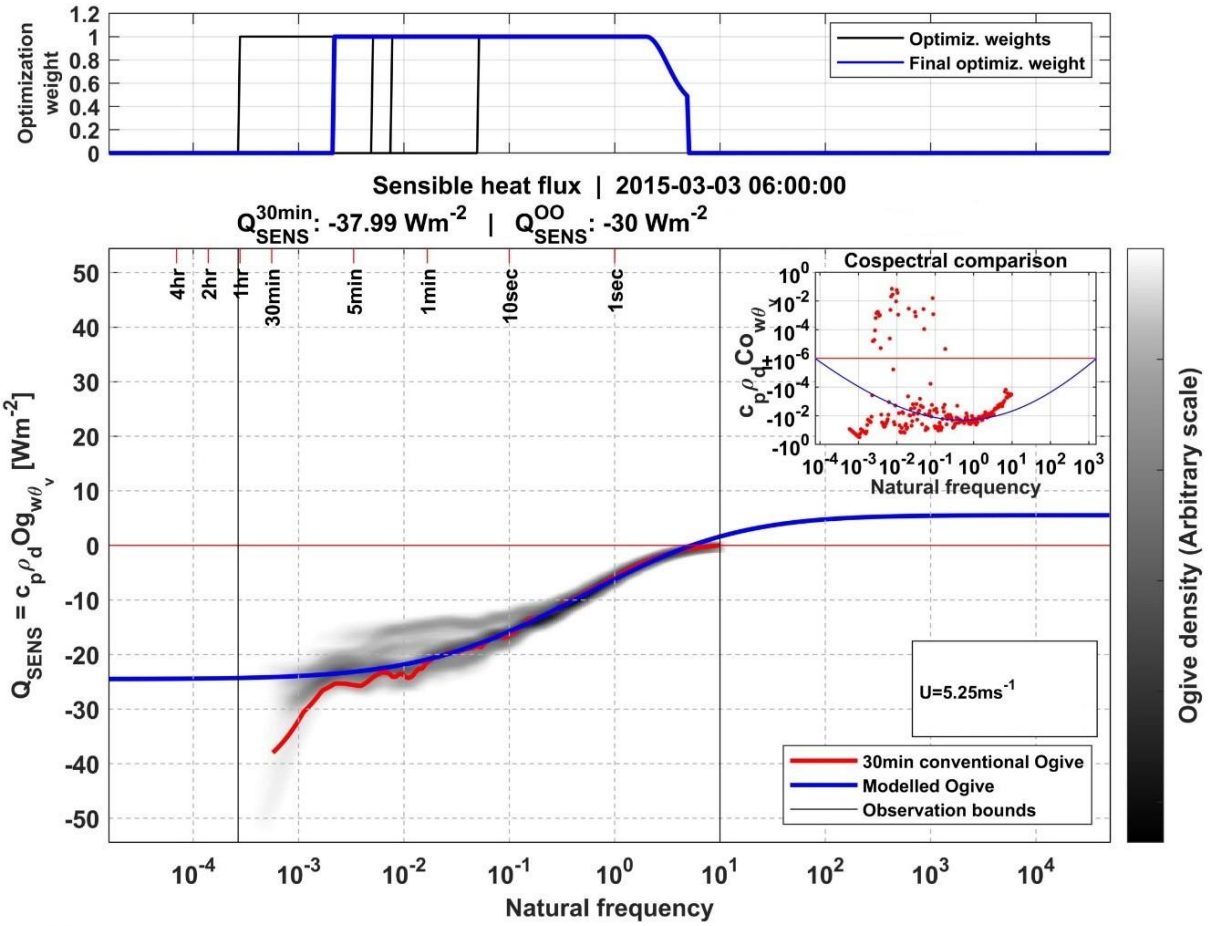

Figure 5.36: Visualization of the ogive optimization of the sensible heat flux between 5:30 and 6:00 UTC on March 3 2015, produced by the OOT.

5.6.1.3.2.2 Ogive optimization

As demonstrated in the previous section, the ogive optimization is a valuable tool to keep non-local, low-frequency contributions from influencing the final fluxes. However in low-flux environments, a high ratio of cospectral variance to actual turbulent flux contribution at times even obstructs the flux calculation by the ogive optimization (Sievers et al., 2015). The excessive cospectral variance then prohibits an unambiguous evaluation of the similarity between observed and theoretical cospectra, as well as a proper placing of the cospectral peak (Sorensen & Larsen, 2010). Figure 5.37 a exemplarily demonstrates how this issue impedes a reliable flux estimation by the ogive optimization method during the present event. In the cospectrum a positive peak appears at a frequency of about 3 to 4 Hz. On the contrary, for frequencies below approximately 1 Hz the contributions to the flux estimate are mostly negative. This phenomenon was already observed on Spitsbergen, at the Adventdalen site and termed “bi-directional fluxes” by Pirk et al. (2017). Under these circumstances the fundamentally different conceptual definition of turbulent fluxes between ogive optimization and conventional EC has a decisive impact on the flux estimates. While the ogive optimization assumes a unidirectional flux, the conventional EC method includes all flux contributions regardless of their direction (Pirk et al., 2017). In the study by Pirk et al. (2017) the ogive optimization was therefore able to better capture a consistent CO_2 release reflected in high frequency range of the spectrum while excluding the CO_2 uptake showing at lower

frequencies. They suggest that the controversial flux contributions might be caused by a layering of air masses with different CO_2 concentrations. While smaller eddies, associated with high frequency fluctuations represent only one air mass, the larger, low frequency eddies circle through two air masses featuring different CO_2 concentrations. As proposed for the Adventdalen site, such a layering might similarly be caused by the intrusion of CO_2-depleted air close to the ground from the surrounding mountains by katabatic winds or by sea breeze circulations from the Kongsfjorden fjord (Esau and Repina, 2012).

During the present event at the Bayelva site, the break point between positive and negative flux contributions is located at a much higher frequency of about 1 Hz, compared to the time scale of about one minute, documented by Pirk et al. (2017). In contrast to their observations, during the event the modelled cospectrum peaks in the lower frequency range, deciding for a questionable negative final flux estimate.

One could hypothesize that the locally meaningful fluxes are actually represented only by the very high-frequency range above 1 Hz. The problem of excessive cospectral variance, prohibiting an unambiguous placing of the modelled cospectrum, could then explain the fact that the cospectral peak is erroneously shifted to lower frequencies. In this case applying the ogive optimization method would impair the final flux estimate since the unidirectional flux definition would further reduce the influence of the “true” positive high-frequency contributions. However the cospectrum presented in figure 5.37 a does not correspond to the average cospectrum for the relevant wind speed range between 4 and 6 ms^{-1} (Figure 5.25 c). According to the ensemble average, the cospectrum would be expected to peak at a frequency of approximately 1 Hz, while the peak observed at higher frequencies might rather correspond to the irregular peak-like structure occurring in the average CO_2 spectra at high wind speeds.

Furthermore between 22:30 UTC on March 2 and 00:30 on March 3 as well as between 3:30 and 4:00 UTC the high-frequency cospectral peak adds a negative contribution to the final fluxes. This is depicted exemplarily in figure 5.37 b.

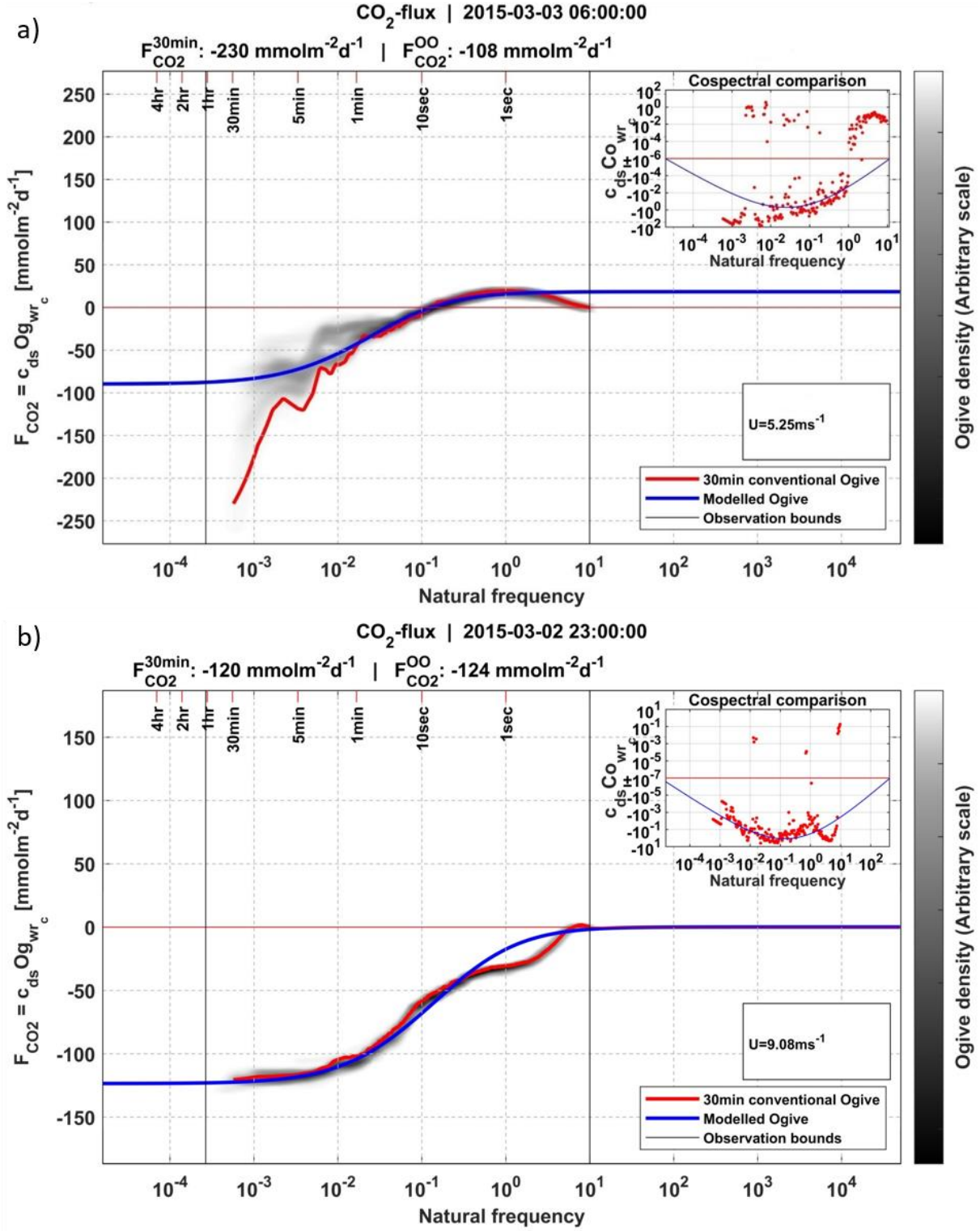

Figure 5.37: Ogive optimization and the corresponding cospectra for the time period **(a)** between 5:30 and 6:00 UTC on 3 March 2015 and **(b)** between 22:30 and 23:00 UTC, as obtained from the OOT.

A counterexample, where the ogive optimization is better suited to capture the locally meaningful flux, is given in figure 5.38. In this low wind situation the cospectral peak is identified at the expected frequency of about 1 Hz. By effectively filtering out the large negative and positive lower-frequency contributions, the ogive optimization provides a slightly positive final flux estimate, matching the low CO_2 emission typical of this time of year.

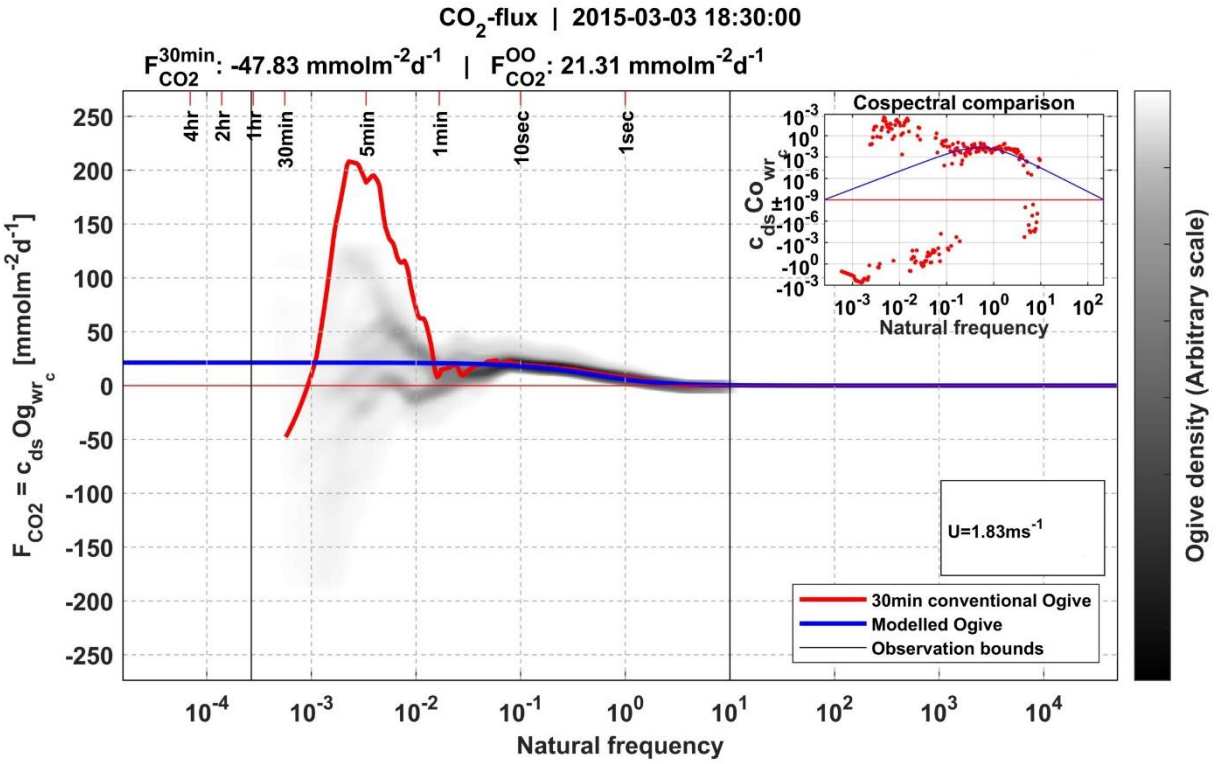

Figure 5.38: Performance of the ogive optimization method in the time period between 18:00 and 18:30 UTC.

All in all it has to be concluded that a thorough evaluation of the performance of the ogive optimization at individual flux estimations is indispensable. Most importantly a deviation of the fluxes obtained using the ogive optimization of those resulting from the conventional EC method does not always indicate a superiority of the ogive optimization technique. Instead, even though an exclusion of lower frequency contributions is particularly important in low-flux environments, especially under these conditions the ogive optimization might at times wrongly force the cospectrum to a unidirectional flux estimate.

5.6.1.3.2.3 Alternative averaging intervals

In order to assess the suitability of the standard 30 minutes averaging interval, the shortest possible averaging period in EddyPro of one minute as well as a longer interval of four hours have been tested for the duration of the event.

While the shorter averaging interval of one minute was not able to remove strong high-frequency noise from the CO_2 spectrum (Figure 5.39 a), sporadic one minute spectra during an only slightly noise-affected 30 minute averaging period display a behaviour close to the ideal -2/3 decrease in the inertial subrange (Figure 5.39 b). In such cases a reasonable flux estimate could possibly still be approximated from one minute intervals, although the 30 minute period results in unphysical flux values associated with white noise.

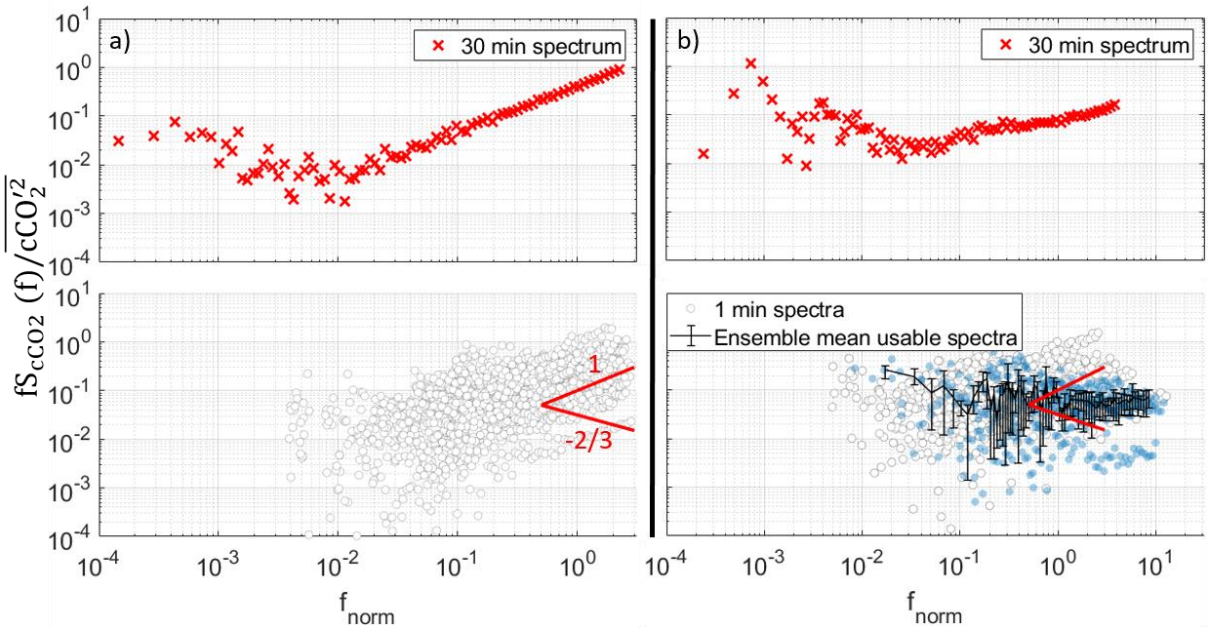

Figure 5.39: Noise-affected CO_2 spectra using a 30 min averaging interval and the corresponding spectra derived for 1 min averaging intervals between **(a)** 3:00 and 3:30 UTC and **(b)** 5:00 and 5:30 UTC. White circles mark noise-contaminated 1 min spectra, while blue spectra might still be usable. Error bars depict the 25 and 75 percentiles, respectively.

While reducing the averaging time to one minute cannot remove serious high-frequency noise in most cases, it often effectively cuts off strong non-local low-frequency contributions to the CO_2 spectrum. At the times that are not flagged for a resolution problem, a shorter averaging time can therefore limit the flux estimates to the locally relevant contributions (Figure 5.40).

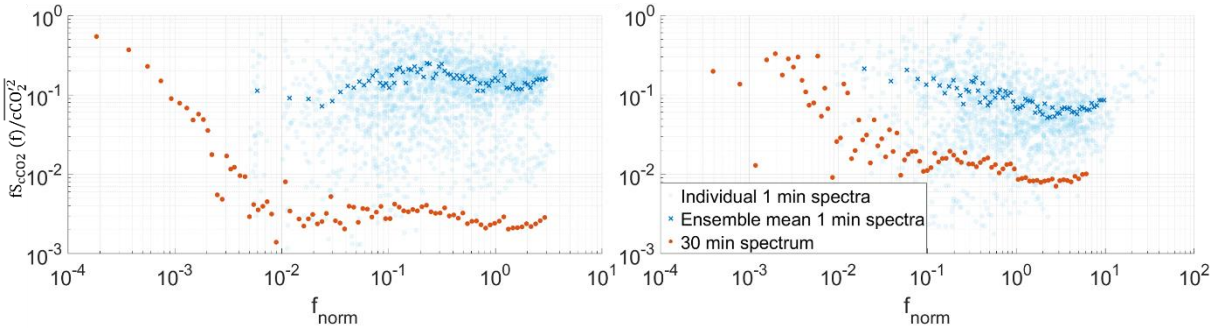

Figure 5.40: Individual spectra and their ensemble mean for an averaging period of one minute as well as the spectrum for the 30 minutes averaging interval for the time periods between **(a)** 21:30 and 22:00 UTC and **(b)** 6:00 and 6:30 UTC. The shift in spectral density between the one and 30 minute spectra is caused by the normalization by the absolute covariance which is larger for the 30 minute interval due to the inclusion of low frequency contributions.

Next to the shortening of the averaging period, calculations were also performed on an extended computation interval to investigate whether the often missing minimum in the cospectral energy, associated with the spectral gap is reached at larger scales. However, as figure 5.41 reveals, there is no clear drop of the cospectrum on time scales between 30 minutes and four hours, either.

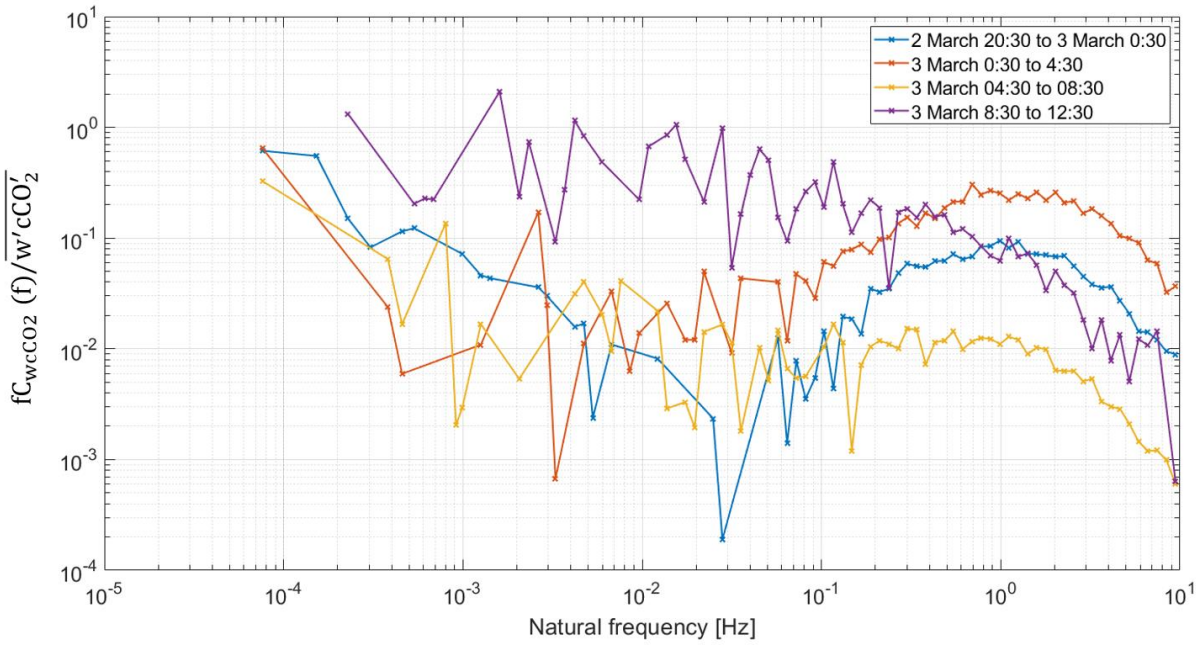

Figure 5.41: Normalized cospectrum of w and CO_2 concentration fluctuations during the event for averaging periods of four hours.

5.6.1.3.2.4 Coordinate rotation

While the fluxes obtained using the planar fit method at most times do not deviate significantly from the baseline run, the large peaks in the corrected as well as in the uncorrected flux time series between 21:30 and 22:00 UTC and between 6:00 and 6:30 UTC appear to be primarily related to the double rotation method. These two time periods mark the beginning and the end of the event, respectively, which are both associated with pronounced changes in wind speed and at the end of the event also in wind direction. The latter case is furthermore soft-flagged for instationarity of the horizontal wind. This suggests that when there is a strong change in the wind regime over a 30 minute period, a single set of rotation angles might not be representative of the whole time span. This could explain the more reasonable fluxes obtained when using one minute averaging intervals with more variable rotation angles particularly at the end of the study period (Figure 5.42). At the beginning of the study period the rotation angles show less variation over the 30 minute interval. Nonetheless the pronounced change in wind speed might render the flux estimates very sensitive to variations in the rotation angles, since changing wind velocities might result in very different stream lines due to a changed overflow of topographical elevations and obstacles. This can furthermore lead to a strongly varying vertical wind velocity over the standard 30 minutes averaging period. Therefore during changing wind speeds it might be inappropriate to force the mean vertical wind velocity to zero for every single 30 minute interval, as performed by the double rotation method. Hence the planar fit method is probably the better choice during pronounced changes in the wind regime. When using the double rotation scheme, shorter averaging intervals, could reduce spurious flux contributions resulting from inappropriate rotation angles.

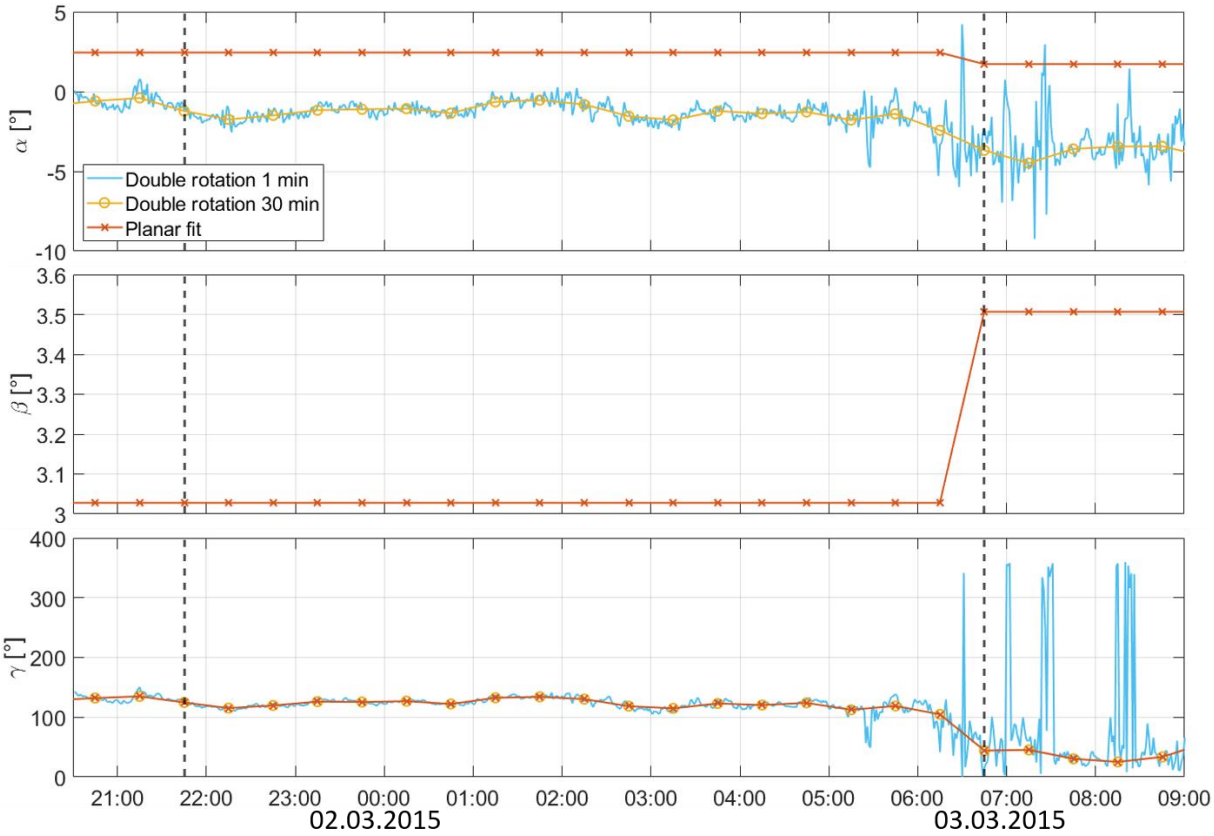

Figure 5.42: Coordinate rotation angles when using the planar fit method as opposed to the double rotation method for 1 min and 30 min averaging intervals.

5.6.1.3.3 The possible effect of pressure pumping

Although the negative fluxes already appear to be largely related to methodological issues, this section, for the sake of completeness, investigates the explanatory power of the pressure pumping phenomenon. With a snow dielectric constant of 2.1, a snow porosity of 0.6 results from equation 4.34. Together with the snow depth of approximately 0.6 m, this provides a pore volume of 0.36 m^3 below one m^2 of the snow surface. Assuming that the snow pores are filled with completely CO_2-depleted air and that all of this air is exchanged with atmospheric air due to barometric pumping, associated with the large scale pressure fluctuations, a total amount of 0.07 gCm^{-2} could be taken up by the snow pores. Even under these strict assumptions this makes up less than one fifth of the effective uptake indicated by the CO_2 fluxes and can therefore not explain the observed uptake event.

5.6.1.3.4 Conclusions for the negative events

As expected, this negative event is most likely caused by methodological rather than physical features. Most importantly the initially slightly positive uncorrected fluxes are transformed into large negative ones, via the WPL correction. The sequence of strongly negative sensible heat fluxes, triggered by the onset of mechanical turbulence associated with high wind speeds, is then directly imprinted onto the CO_2 fluxes. This furthermore introduces the observed positive correlation between the absolute CO_2 fluxes and wind speed or friction velocity, respectively.

There is only one negative peak event in November, which occurs simultaneously to an event of upward sensible heat flux, resulting in a positive WPL term. However the CO_2 fluxes during this event are strongly affected by white noise, and most of the flux estimates are hard-

flagged for spikes in the CO_2 concentration time series as well as excessive skewness and kurtosis. These quality issues result in CO_2 fluxes that are already strongly negative prior to the WPL correction. Therefore the negative WPL correction of unphysical raw flux estimates that are close to zero can generally be assumed as an explanation for the negative flux events. Furthermore this case study underlines the importance of inspecting the automatically detected time lags for plausibility and of limiting its range to realistic values.
Concerning the coordinate rotation, the planar fit method appears to be a more suitable choice, particularly during pronounced changes in wind regimes in the sloping terrain of the Bayelva site. For averaging periods shorter than the standard 30 minutes, this issue becomes less relevant.
The often missing spectral gap between high and lower frequency spectral contributions could neither be found at larger time scales. Instead, a shorter averaging time of one minute in several cases effectively extracted the locally meaningful part from the signal. However due to the frequency shift of the spectrum with changing wind speed, the appropriate averaging interval varies in time. Therefore the ogive optimization is better suited for longer term studies because it automatically determines the optimal averaging period for every individual time interval. The ogive optimization is thus a valuable tool for flux computation in low-flux environments, where already small non-local influences can have a large relative effect on the final flux estimates. However its implementation might still need some refinement, especially regarding low-flux conditions. In particular it would be desirable to achieve a more accurate detection of the break point between local and lower-frequency contributions in the case of bidirectional fluxes.

5.6.2 A positive single peak event

The following case study deals with a positive single peak event, which occurred during polar night conditions between 23:30 UTC on 5 December and 2:30 UTC on 7 December 2015, thus lasting for approximately one day. During the event the positive CO_2 fluxes reach values of up to 1.25 $\mu molm^{-2}s^{-1}$ and together amount to a net CO_2 emission of 0.47 gCm^{-2} (Figure 5.43).

5.6.2.1 Meteorological, soil and snow conditions during the event

During the event the atmospheric pressure strictly rises by 11 hPa. This increase already starts 9 h before the beginning of the event at 972 hPa and the pressure reaches a maximum 34 h after its end at a by 35 hPa enhanced level of 1007 hPa. This pronounced pressure change as well as the amplified wind speed of up to 12 ms^{-1} during the event are related to the connection of a formerly stationary low pressure system over Svalbard to a stronger low pressure system passing south of Svalbard on its way from Iceland over Scandinavia to Russia (Figure 5.44). Simultaneously to the development of the absolute humidity, the air temperature decreases by about 4 °C, to a minimum of -6 °C at 14:00 UTC, followed by an increase by 2 °C towards the end of the event. This course is similarly reflected in the snow temperatures at a by constantly 2 °C lower temperature level. The magnitude of H, LE and u* are clearly positively correlated with the wind speed. Wind speeds exceeding approximately 10 ms^{-1} furthermore resolve the mostly stable stratification of the lower atmosphere. The CO_2 concentration increases by about 0.5 $mmolm^{-3}$ during the event. The wind mainly comes from the south-easterly wind sector, becoming more variable with the decreasing wind speed after

the end of the event. The shortwave incoming radiation is negligible due to the polar night conditions and the longwave net radiation approaches zero during the second half of the event. During the event no precipitation was recorded and no snow fall can be seen from the hourly photographs of the study site. This implies that the slight increase in snow height during the first hours of the event is caused by snow advection associated with the high wind speeds. The remaining snow and soil parameters do not change significantly during the event either.

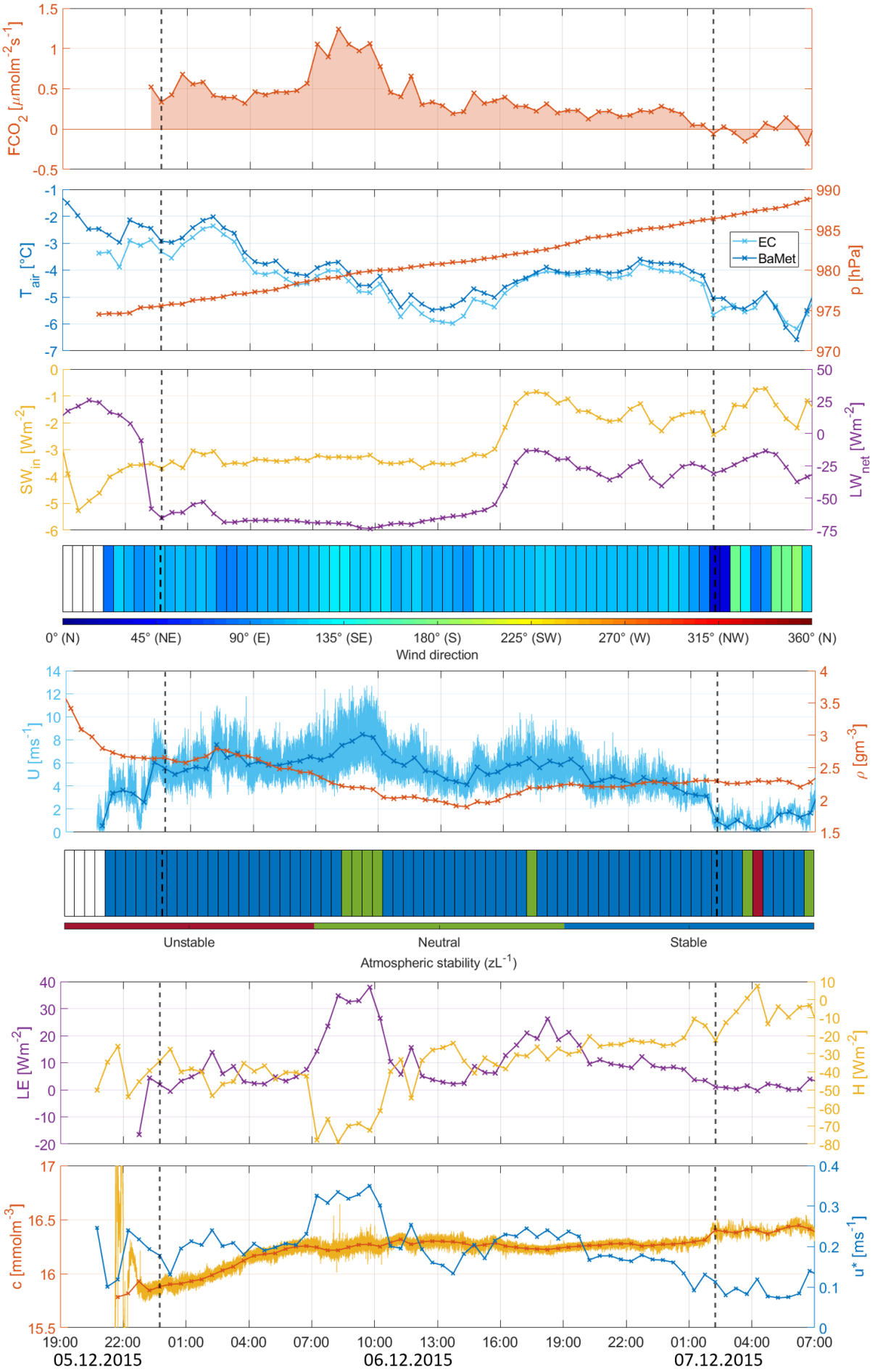
FCO2 [μmolm-2s-1]
Tair [°C]
p [hPa]
EC
BaMet
SWin [Wm-2]
LWnet [Wm-2]
0° (N)
45° (NE)
90° (E)
135° (SE)
180° (S)
225° (SW)
270° (W)
315° (NW)
360° (N)
Wind direction
U [ms-1]
ρ [gm-3]
Unstable
Neutral
Stable
Atmospheric stability (zL-1)
LE [Wm-2]
H [Wm-2]
c [mmolm-3]
u* [ms-1]
19:00
22:00
01:00
04:00
07:00
10:00
13:00
16:00
19:00
22:00
01:00
04:00
07:00
05.12.2015
06.12.2015
07.12.2015

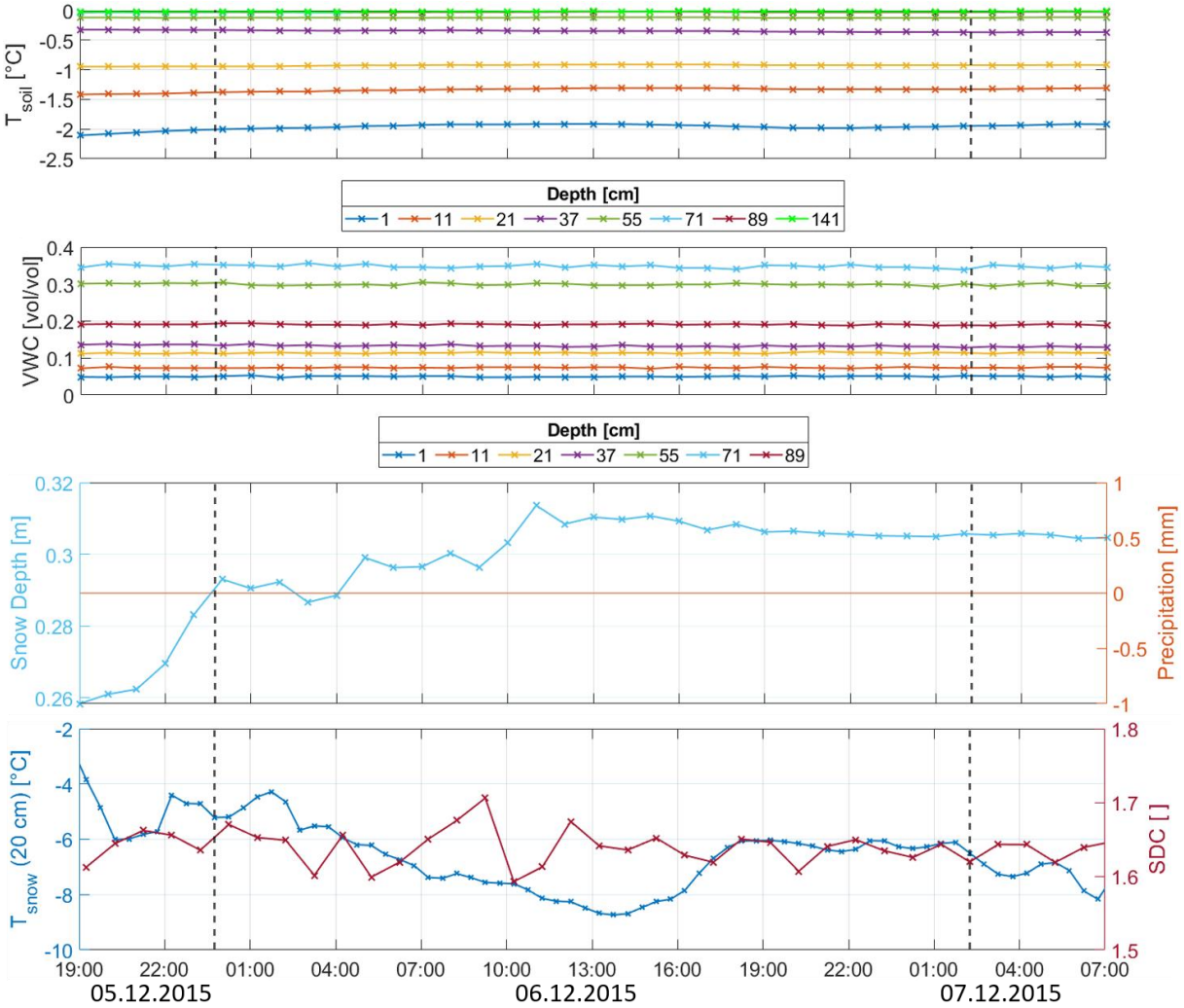

Figure 5.43: Overview of the development of meteorological, soil and snow conditions during the event. The variables are the same as depicted in the first case study, supplemented with liquid precipitation and the snow temperature at 20 cm above the ground.

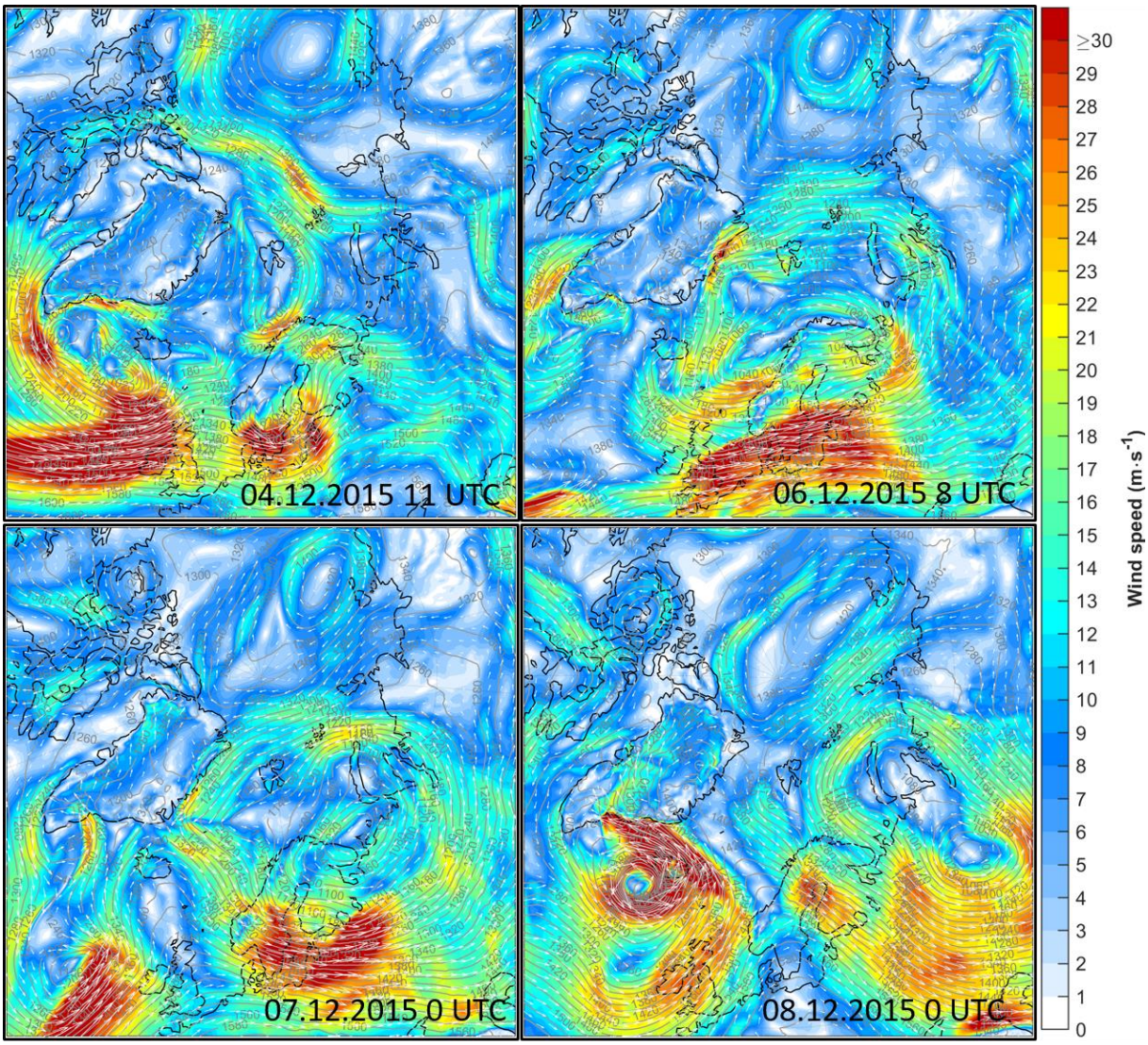

Figure 5.44: ERA5 geopotential height (contour lines) and horizontal wind speed (colors) and direction (arrows) at the 850 hPa level. The illustration is based on data from the Climate Data Store (https://cds.climate.copernicus.eu/cdsapp#!/home).

5.6.2.2 Quality assessment

During the event no flux estimates are hard flagged according to the overall flagging policy (Figure 5.45). Only sporadic combined soft flags and raw data flags as well as one noise contamination flag indicate quality issues of some flux values. However the affected values still integrate well into the time series. Thus, as opposed to the negative flux event, there is no obvious quality issue, which would suggests an unphysical reason for the unusually large CO_2 fluxes.

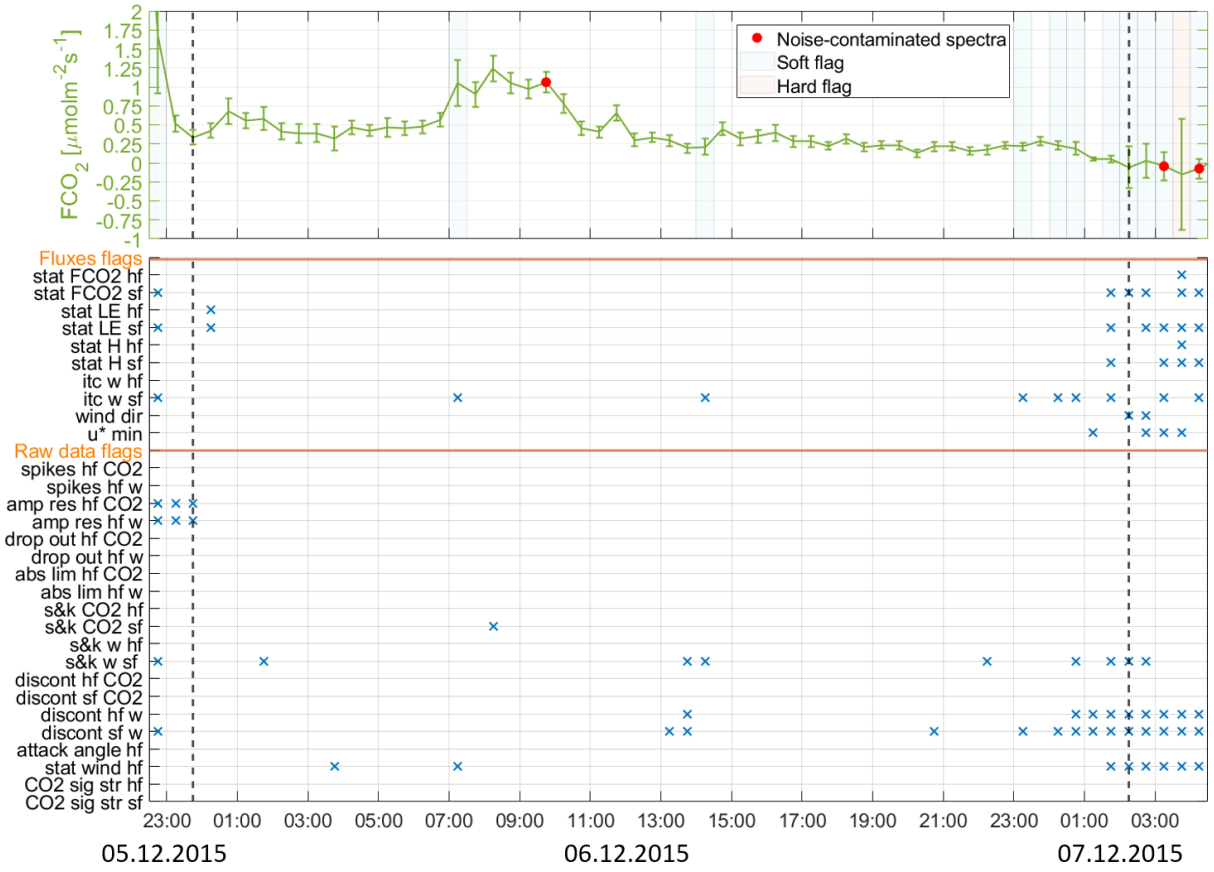

Figure 5.45: CO_2 flux time series between two hours before and two hours after the event and quality flags similar to the ones in figure 5.29.

5.6.2.3 Methodology of the event

As opposed to the first case study, the automatically determined time lags were found to stay within a reasonable range. Thus the application of site- and wind-specific limits to the time lag detection algorithm had no effect on the final flux estimates.

Due to larger negative sensible heat fluxes during the event, the WPL term is increased compared to the first case study. At the same time the spectral correction factors are amplified as well, so that the final deviation between the individual flux estimates of the baseline and the uncorrected run stays similar to the first case study (Figure 5.46; Table 5.6).

Over the whole event the fluxes derived using the planar fit rotation method stays within the range of random error of the baseline run. The results obtained from the OOT do not differ significantly depending on the application of the conventional EC or the ogive optimization technique. However both time series exceed the baseline run by about 50 % at its maximum plateau.

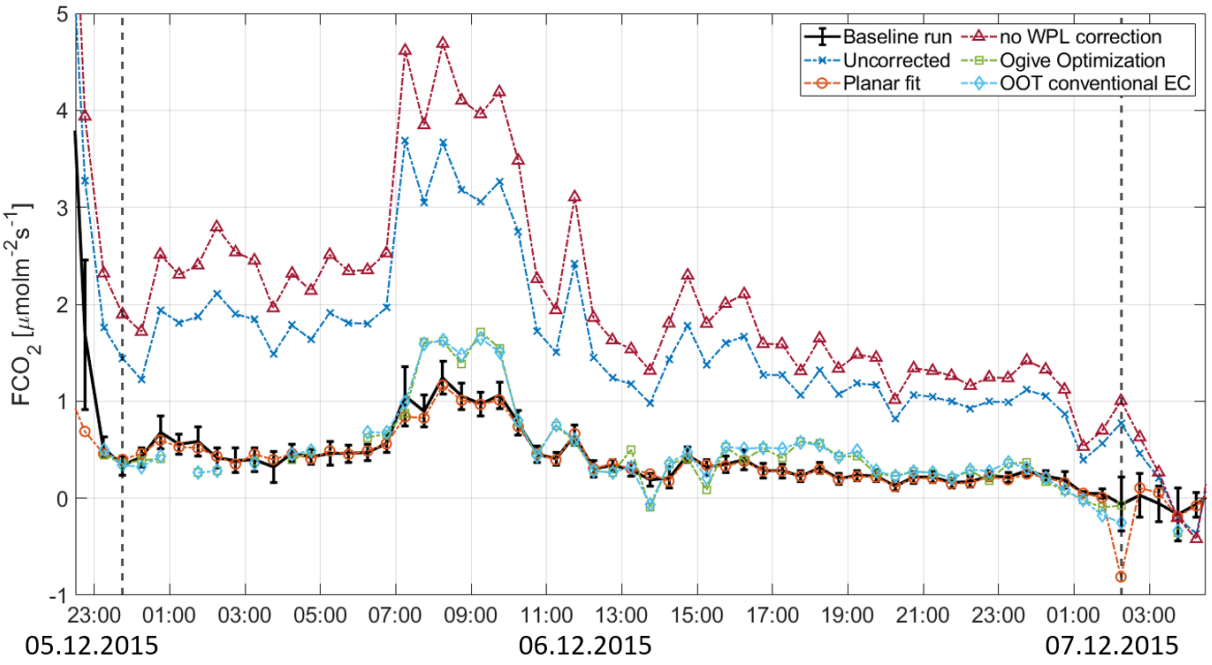

Figure 5.46: CO_2 fluxes resulting from applying different corrections and computation methods. Designations are equivalent to the ones in figure 5.32.

Table 5.6: Overview of the net CO_2 exchange during the event and the absolute and relative average deviation of the individual flux estimates from the base run for the different correction and computation methods.

Computation method	Total net CO_2 exchange during the event [gCm^{-2}] and deviation from the baseline run ([%])	Mean deviation of the individual flux estimates from the baseline run [$\mu molm^{-2}s^{-1}$] ([%])
Baseline run	0.47	
Planar fit	0.46 (+2)	-0.01 (-15)
Ogive optimization	0.51 (+9)	+0.08 (-15)
OOT conventional EC	0.52 (+11)	+0.09 (-9)
uncorrected	1.84 (+291)	+1.22 (+76)
without WPL correction	2.37 (+404)	+1.68 (+81)

Figure 5.47 furthermore reveals a strong positive correlation between the CO_2 fluxes and the friction velocity with a Pearson correlation coefficient of 0.89 for the uncorrected flux estimates. Because the magnitude of the negative WPL term is also correlated to wind speed and friction velocity, the WPL correction counteracts the interdependency between u* and FCO_2. However this effect is not strong enough to dissolve the relationship but only weakens it to a correlation coefficient of 0.85. This could explain the correlation between CO_2 fluxes and sensible heat fluxes, identified in section 5.3.4. It could furthermore indicate an incomplete WPL correction at strong negative sensible heat fluxes for example due to an underestimation of the absolute sensible heat flux, as proposed by Hirata et al. (2005). Using the bulk sensible heat flux to calculate the WPL term would result in mostly negative CO_2 fluxes during the events except for the period of especially high raw CO_2 fluxes between 7 and 10 UTC. Regarding this high sensitivity of the CO_2 flux to the WPL term, simultaneous reference measurements would be useful to estimate the uncertainty in the sensible heat flux. An additional correction for pressure fluctuations would on the contrary further strengthen the correlation between wind speeds and CO_2 fluxes.

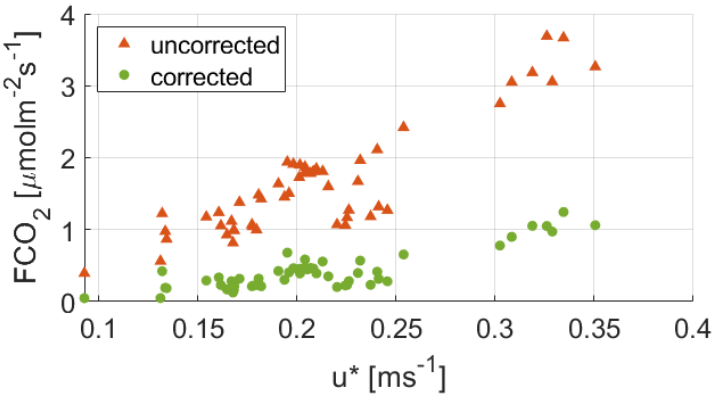

Figure 5.47: CO_2 flux as a function of friction velocity before and after WPL and spectral corrections.

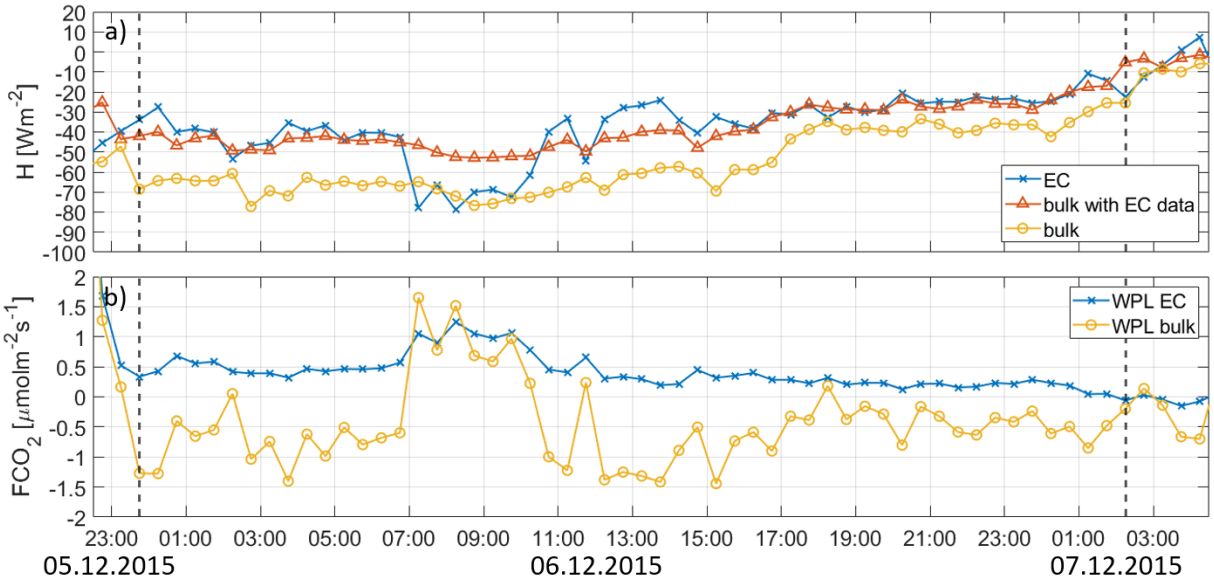

Figure 5.48: (a) Sensible heat fluxes during the event as obtained from the EC method and the bulk method using the data recorded at the EC system (bulk with EC data) and at the Bayelva meteorological station (bulk). **(b)** CO_2 fluxes after WPL correction based on the bulk sensible heat flux as opposed to the baseline run.

5.6.2.4 The possible contributions of physical mechanisms

Except for a possible underestimation of the sensible heat flux, at first sight no methodological reason appears for the large positive CO_2 fluxes, which strongly correlate with wind speed and friction velocity. Therefore the following section will quantify and discuss several physical phenomena that might contribute to the observed fluxes.

5.6.2.4.1 Pressure pumping

One phenomenon that could provide a physical explanation for the correlation between wind speed or friction velocity and the CO_2 fluxes is pressure pumping. According to equations 4.33 – 4.35, and using a snow depth of 0.3 m and a snow dielectric constant of 1.65, the maximum amount of CO_2 that can be stored in the snow back is estimated to 0.08 gCm^{-2}. Figure 5.49 reveals that under the emission rate given by the flux values, this reservoir would be used up only 3.5 hours after the beginning of the event.

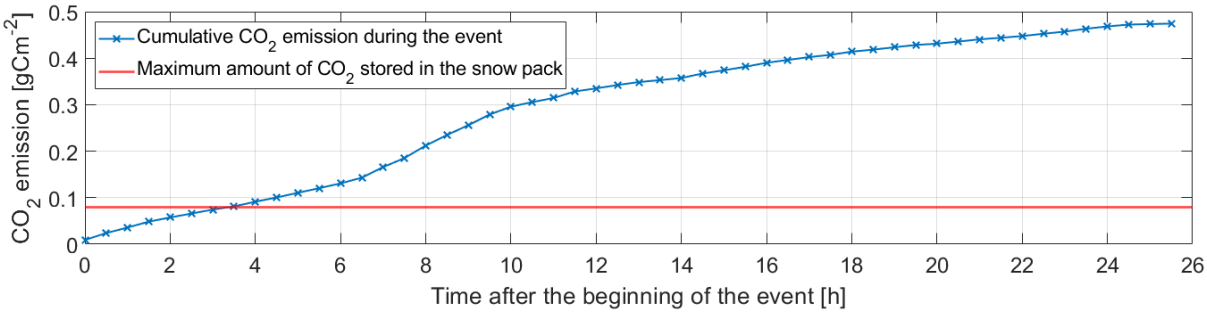

Figure 5.49: Cumulative sum of the CO_2 released during the event, compared to the amount of CO_2 that could maximally be emitted from the snow pack.

However snow density and CO_2 concentration in the snow pores are actually highly variable. Hence the use of values obtained only from sporadic manual measurements might lead to very inaccurate estimates of the amount of CO_2 stored in the snow pack. Therefore its dependency on snow density and CO_2 concentration is investigated in figure 5.50. The figure reveals that a CO_2 concentration of more than 3300 ppm in the snow pores together with a snow density below 80 kgm^{-3} would be needed to allow for a CO_2 emission similar to the one indicated by the flux values. Such densities are typically only attained by fresh snow. However no significant snow fall was recorded for more than one month before the event, probably resulting in a much higher snow density. The possible presence of areas with a larger snow depth inside the footprint of the EC system could imply a higher potential for CO_2 uptake by the snow pack. However the contribution of this high variability of the snow depth is probably not sufficient to explain the large event fluxes. Furthermore the event is surrounded by two other positive single peak events, the first ending one day before and the next beginning four days after the current event. The events feature a total CO_2 emission of approximately 0.4 gCm^{-2}, each and are both associated with high wind speeds, while wind speeds are low in the meantime. On first sight this does not indicate that a CO_2 reservoir in the snow pack is used up during an event and refilled afterwards. Based on further investigations of the CO_2 concentration gradient between soil, snow and atmosphere the time needed to refill the snow pack storage by means of diffusive transport could be estimated to validate this hypothesis. All in all, while it may well be that CO_2 is released from the snow pores due to wind induced pressure pumping, it is most likely not the only process responsible for the positive flux event.

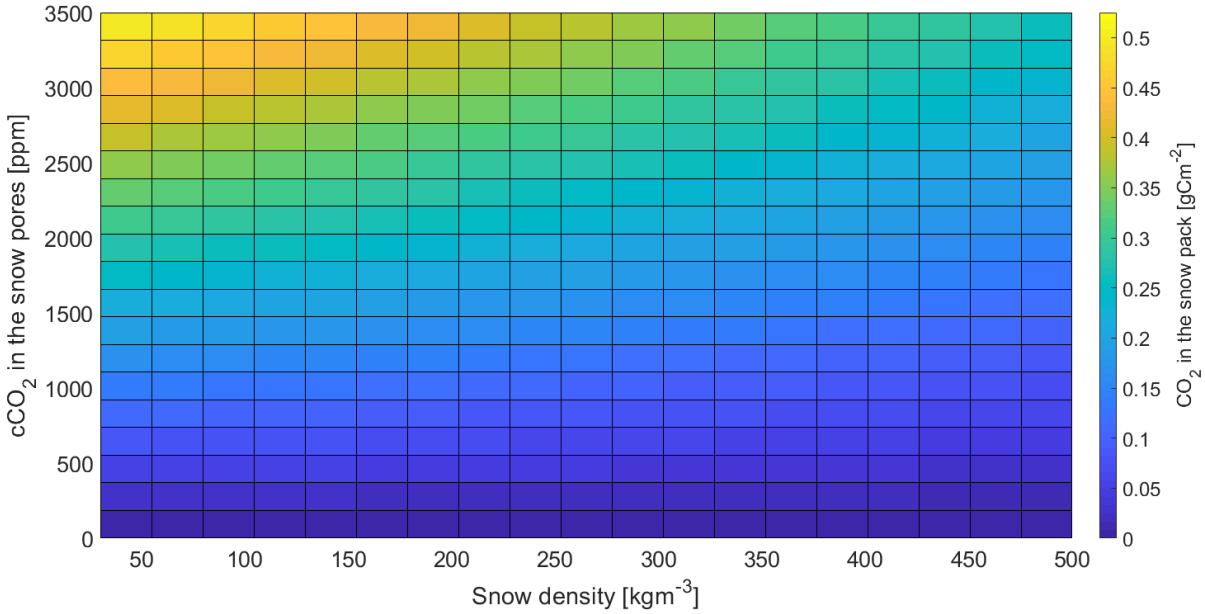

Figure 5.50: Amount of CO_2 that can be stored in the snow pack as a function of the CO_2 concentration in the air-filled snow pores and snow density, given a snow depth of 0.3 m.

5.6.2.4.2 Storage below the measurement height

Another possible explanation could be, that the CO_2, which is released from the soil and the snow pack through diffusion, accumulates below the measurement height during periods of stable stratification. With the onset of turbulent conditions, related to an increase in wind speed, the CO_2 rich air is then mixed up to the measuring instruments. Again the rate of CO_2 release from the ground, as obtained for example by chamber measurements, would be needed to reliably estimate the amount of CO_2 that could accumulate during the time between two consecutive events. The storage flux calculated by EddyPro ranges between -0.03 and 0.06 $\mu molm^{-2}s^{-1}$ during the event and is thus negligible compared to the overall CO_2 flux. However, as mentioned before, considering the lack of CO_2 concentration profile measurements, these estimates might not be overly representative of the reality.

5.6.2.4.3 Advection

The small deviation between the two CO_2 flux time series obtained from the OOT does not indicate a major contribution of the advection of CO_2-rich air to the study site. However, as in the case of the negative peak event, the cospectra reveal a frequent occurrence of bidirectional fluxes. As opposed to the negative event, both high and lower-frequency flux contributions are mostly positive. Nonetheless the cospectral peak is placed at lower frequencies rather than at the prominent peak at the high-frequency end of the spectrum (Figure 5.51). Hence a significant non-local low-frequency influence might still be included in the final flux estimate because it is simply not recognized as such.

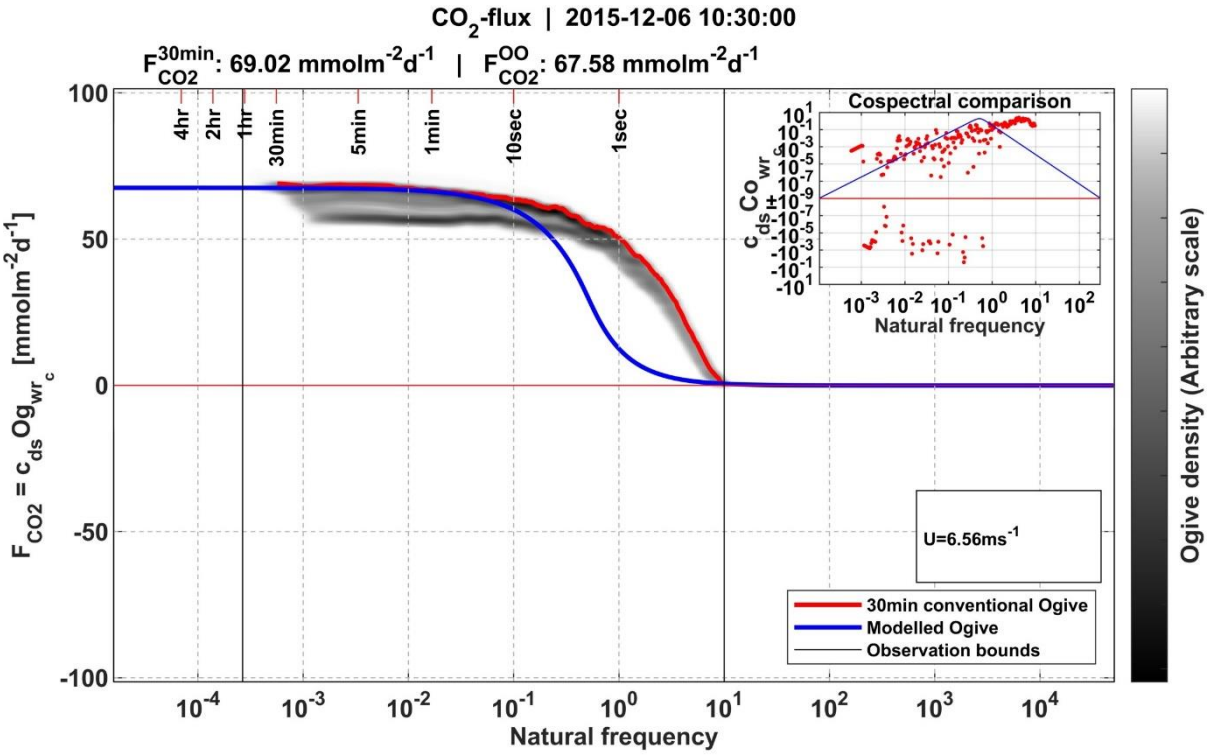

Figure 5.51: Ogive optimization of the CO_2 flux between 10:00 and 10:30 of December 12 2015.

5.6.2.5 Conclusions for the positive events

In contrast to the negative flux event, discussed in the first case study, there is a higher probability that physical processes contribute to the large positive CO_2 fluxes. Pressure pumping, CO_2 accumulation below the measurements height and advection of CO_2 rich air could have a significant influence under the given environmental conditions. However from the sequence of consecutive events there is no evidence for a CO_2 reservoir that alternately used up and refilled as it would be expected for pressure pumping or storage below the instrument height. Therefore accurate high frequency pressure records would be needed to estimate the influence of wind induced pressure pumping. Profile measurements of the CO_2 concentration inside the snow pack and in the atmospheric layer below the measurement height could furthermore help to quantify the respective storage change. However the generally small CO_2 fluxes are furthermore highly sensitive to changes in the WPL correction, which is dominated by the thermal expansion term. The accuracy of the sensible heat flux estimates should therefore be carefully considered based on reference measurements.

6 Implications of the study results for carbon budget studies

In the following section the implications of the study results for the annual carbon balance as well as for future carbon budget studies will be discussed.

The first case study reveals that negative events most likely result from a limited performance of the applied gas analyzer under certain atmospheric conditions. They can thus be considered as unphysical and should be excluded from the flux time series, since they lead to a significant overestimation of the annual carbon uptake. Replacing the CO_2 fluxes affected by significant high frequency noise by a flux of 0 $\mu molm^{-2}s^{-1}$, results in a reduction of the negative annual carbon budget by 15.42 gCm^{-2} to a much smaller annual net uptake of -6.56 gCm^{-2}. However

this simple exclusion of the corrupted flux estimates, just as a standard gap filling procedure, might not be appropriate in the case of the FCO_2 events, if high wind speeds actually have a physical impact on the CO_2 fluxes. The question of how to deal with unphysical negative event fluxes is therefore closely related to the question concerning the reliability of positive event fluxes. The appropriate handling of positive events depends on the drivers of the observed unusual fluxes. Fluxes which are amplified due to pressure pumping or the upward mixing of CO_2 rich air from below the measurement height should generally be included in the annual carbon budget. They comprise CO_2 which is released locally from the soil and whose detection is only delayed due to the buffering effect of the snow pack or the usually stable stratification of the winterly Arctic boundary layer. The effect of advection should on the other hand be excluded from process-oriented studies since it involves non-local CO_2 contributions that are transported to the study site from remote regions.

However the flux events might result from a synergy of all three phenomena. In order to quantify their individual contributions, further measurements and a further adjustment of methodological tools are needed. Accurate high frequency pressure measurements could serve for an improved estimation of the significance of pressure pumping as well as of a possible correction term for pressure fluctuations inside the measurement path. Profile measurements of the CO_2 concentration inside the snow pack and in the atmospheric layer below the measurement height could indicate the storage change in the two media. Regular chamber measurements would moreover provide independent information on the actual carbon release directly at the ground level. Further development of the implementation of the ogive optimization technique would be useful for an effective elimination of advective flux contributions. Shorter averaging intervals could furthermore provide a larger share of usable flux estimates. In this context wavelet analysis could be a valuable tool since it allows for averaging periods in the order of minutes and thus supports the evaluation of EC data under non-steady-state conditions (e.g. Collineau & Brunet, 1993; Katul & Parlange, 1995; Trevino & Andreas, 1996). Considering the high sensitivity of the generally small CO_2 fluxes during the Arctic winter to the WPL correction term, detailed knowledge of the uncertainty of the sensible heat flux estimates is vital for a profound quality assessment of the CO_2 fluxes. Independent reference measurements of the sensible heat flux could thus be used to validate the EC observations. Similarly an EC system involving a closed-path gas analyzer could provide reference values for the CO_2 fluxes in a future study. However although several studies suggest a better performance of closed-path gas analyzers under the extreme Arctic conditions since they better reproduce chamber measurements (e.g. Butterworth & Else, 2018), one cannot be completely sure that the different fluxes obtained from closed-path measurements better reflect the reality than the open-path observations.

A rough visual inspection of time series suggests that FCO_2 events also occur in the summer months during periods of high wind speeds. However since strong winds are more seldom observed in the summer, FCO_2 events are similarly expected to occur predominantly during the winter months. Nevertheless the magnitude of events during the snow free period could help to quantify the contribution of pressure pumping during the winter months, since wind ventilation and pressure fluctuations affect the porous snow pack much more strongly than

the bare soil. Furthermore during the summer month, solar heating initiates additional turbulence through free convection. The generally reduced stability of the atmosphere renders an accumulation of a large amount of CO_2 below the measurement height unlikely. Therefore advection or methodological issues are the most likely drivers of FCO_2 events during the summer. However the analysis of FCO_2 events during the summer months is more difficult due to a superimposition of the seasonal and diurnal cycle of the CO_2 fluxes.

All in all, the results of this study generally question the suitability of the applied measurement system for a reliable quantification of the net carbon exchange under the extreme conditions of the Arctic winter. During low-wind conditions the surface can be decoupled from the measurement height, leading to an accumulation of CO_2 below the instruments. Thus a lower limit of the friction velocity is often applied to filter out CO_2 fluxes under non-turbulent conditions. The resultant data gaps are usually filled with modelled flux values. However, assuming that the detection of the CO_2 released from the soil is just postponed to periods of high wind speeds, gap-filling might result in the CO_2 efflux to be counted twice (Papale et al., 2006), resulting in a serious overestimation of the soil respiration. A significant underestimation of the CO_2 emission can on the other hand arise if the CO_2 stored below the measurement height during stable conditions is transported away horizontally and thus never reaches the measurement height (Aubinet et al., 2012). This indicates that the measurement height of 3 m might be too high to capture the actual CO_2 efflux from the soil during the mostly stable conditions of the Arctic winter. Furthermore this study reveals that due to sensor limitations, especially at a net longwave radiation close to zero and a high relative humidity CO_2 fluxes under conditions of well-developed turbulence are not usable either. Aubinet et al. (2012) additionally recommend an exclusion of CO_2 fluxes, correlating with friction velocity, which is generally the case during positive flux events. Based on these considerations the question arises if sufficient observational data remains to reliably estimate the winter efflux from the permafrost soils after discarding all unphysical flux estimates.

The rough visual inspection of a CO_2 flux time series recorded at an EC system closer to the village of Ny Ålesund suggest that the FCO_2 events simultaneously occur at both stations. This indicates that the events are not specific to the measurement setup at the Bayelva site and might thus appear in CO_2 flux time series recorded all over the Arctic region. Since the drivers of the flux events are not yet sufficiently understood, the handling of the time periods of unusually large CO_2 fluxes probably differs significantly among different studies. While an inclusion of negative flux events might result in a serious overestimation of the annual carbon uptake, a discard and subsequent gap-filling of the positive flux events might lead to a disregard of most of the CO_2 emission during the winter time. Both phenomena might seriously distort the annual carbon budget of Arctic permafrost sites. Thus it cannot be ruled out that current climate projections, involving observational CO_2 flux data are subject to uncertainties that are much larger than expected. Among others Rinke et al. (2017) moreover found an increase in extreme cyclone events on Svalbard in the winter. This indicates that winter time FCO_2 events might occur more frequently in the future. This further underlines the importance of investigating the events and their drivers in order to develop general recommendations on their handling. At the same time the observation and analysis

techniques probably still need to be further improved and adjusted to the exceptional requirements of the high-Arctic winter.

7 Summary and conclusions

In this study 52 events of unusually high positive (apparent CO_2 release from the ground) or negative (apparent CO_2 uptake by the ground) CO_2 fluxes, persisting over time periods from several hours to four days, were identified at the high Arctic Bayelva site during the winter months of 2015. In total these events account for 30 % of the annual net carbon uptake at the study site. Thus a detailed investigation of these largely unexplored time periods of enhanced CO_2 exchange between the surface and the atmosphere is crucial not only for an improved understanding of the drivers of CO_2 fluxes during the Arctic winter but also in order to reliably estimate the net carbon exchange over extended time periods. The events were generally found to occur during distinct changes in atmospheric pressure, temperature, humidity, wind direction and longwave radiation, associated with the large scale shifts of different air masses and an intense cyclone activity during the winter months. Most obviously the occurrence of CO_2 flux events is connected to the onset of turbulent conditions during periods of high wind speeds. While the increase in absolute sensible and latent heat fluxes at high wind speed is directly related to the enhanced turbulent transport, the CO_2 exchange is generally not expected to correlate with the wind speed since it is normally driven by biotic factors like solar irradiation and soil temperatures. This indicates that the observed CO_2 flux events either result from technical or methodological issues or from physical processes, which are not yet sufficiently understood.

For negative events a strong noise contamination of the spectra of CO_2 concentration fluctuations could be identified. This problem predominantly occurs during periods of a longwave net radiation close to zero and a high relative humidity. The exact reason for this malfunction of the gas analyzer could not be determined in this study and should be further investigated to allow for a possible improvement of the sensor technique. The negative flux events, showing a strong correlation between wind speeds and flux magnitude, are therefore caused by the imprint of the strongly negative sensible heat fluxes onto the erroneous CO_2 flux time series via the WPL correction. The negative flux events can therefore be rated as unphysical and should hence be discarded from carbon budget studies.

The causes of positive flux events could on the other hand not be finally clarified. The flux quality during positive events is generally improved compared to the negative events. A methodological explanation for the large flux estimates could be an incomplete WPL correction associated with an underestimation of the sensible heat flux. The most promising explanation concerning the investigated physical drivers is the advection of CO_2 rich air to the study site from remote regions. The potential reservoir of CO_2 rich air inside the snow pack is most likely too small for pressure pumping or wind ventilation alone to be able to explain the large CO_2 efflux. Furthermore from the sequence of consecutive events there is no evidence of a storage process involving a reservoir of CO_2 rich air in the snow pack or below the measurement height which is alternately used up and refilled. Further research is urgently

needed to separate the interacting contributions of various methodological and physical drivers, since the causes of the CO_2 fluxes largely determine the appropriate handling of the flux events. The abrupt release of CO_2 rich air from a reservoir below the measurement height, triggered by the onset of turbulence, might account for a major part of the CO_2 emission from the soil during the winter months and should thus definitely be included in long term carbon budget calculations. Advective contributions should on the other hand be excluded from studies which aim to quantify the net exchange of CO_2 inside the footprint area of an EC system.

Further research concerning the drivers of the CO_2 flux events could make use of the total of 11 years of nearly continuous flux observations at the Bayelva site. However, prior to an extension of the study period, further investigations involving shorter term measurements specifically designed to illuminate the flux events would be useful. For this kind of study reference measurements should be conducted in additions to the open-path EC observations. For example a closed-path EC system could be used to assess the uncertainty of the CO_2 flux estimates. Most importantly, considering the high sensitivity of the generally small CO_2 fluxes to the large WPL terms, reference measurements are needed to evaluate the accuracy of the sensible heat flux measurements. Furthermore continuous profile measurements of the CO_2 concentration inside the snow pack as well as in the atmospheric layer below the measurement height could serve an estimation of the respective storage fluxes. Simultaneous accurate high-frequency observations of the atmospheric pressure might allow for an estimation of the impact of pressure pumping on various time scales as well as of including the pressure fluctuation term in the WPL correction. Moreover regular chamber observations can be used as reference values for the actual CO_2 release from the soil, measured much closer to its source. Due to the exceptional conditions of the Arctic winter, particularly related to the typically very stable atmospheric stratification a measurement height of about 3 m is probably too high for the observations to be generally representative of the exchange processes at the surface. Therefore the additional measurements outlined above could be a reasonable extension of the general EC measurement setup in polar regions. At the same time further research could investigate the possibility of developing novel measurement systems which are better suited for the extreme conditions of the Arctic winter.

Furthermore several recommendations concerning the processing of EC observations can be derived from this study. First of all the study underlines the importance of limiting the possible time lags between the anemometer and the gas analyzer measurement series to a plausible range, particularly in low-flux environments. Furthermore the planar fit method or the use of shorter averaging intervals, when applying the double rotation method, provide more realistic coordinate rotation angles during changing wind regimes. In general the effect of different computation settings should be investigated in detail before applying them to a long term data set. Subsequently a thorough quality assessment should, in addition to the overall flagging policy and standard quality criteria, involve the results from further statistical screening of the raw data set. Most importantly with respect to the negative CO_2 flux events the flux time series should be checked for excessive high-frequency noise contribution to the

gas analyzer measurements. This issue is partly covered by the amplitude resolution test implemented in EddyPro.

Furthermore due to the expected large influence of non-local advective flux contributions, the ogive optimization technique was generally found to be a valuable tool for flux computation, particulary in low-flux environments. As opposed to EddyPro it does not require the existence of a clear spectral gap between turbulent and lower frequency contributions since it allows for varying averaging intervals. However, due to the often bidirectional contributions to the individual fluxes estimates, the ogive optimization technique in many cases erroneously places the cospectral peak to too low frequencies. As a result the assumption of a unidirectional flux by the ogive optimization method further obscures the actual CO_2 exchange. In this context the phenomenon of bidirectional fluxes needs further investigation in order to allow for an improvement of the ogive optimization technique.

All in all, measurement and evaluation techniques conventionally applied for the observation and analysis of gas fluxes are not well suited for the exceptional conditions of the Arctic winter. Therefore future studies should always involve a thorough discussion of suitability of the measurement setup with respect to their specific research aims.

For the processing, analysis and interpretation of already available data sets, the understanding of the unusual flux events, investigated in this study, is of uttermost importance. Particularly since their contribution to the annual carbon budget is expected to further increase in the future due to a rise in the frequency of occurrence of the identified event triggers, namely the winter time cyclonic activity (Rinke et al. 2017). In the absence of a justified and standardized handling of the events of unusually high CO_2 exchange across circum-arctic permafrost sites, the use of long term flux time series as an input for large scale climate modelling efforts might introduce an uncertainty of unexpected magnitude to future climate projections.

Acknowledgement

First of all I would like to thank my supervisors Prof. Dr. Susanne and Prof. Dr. Julia Boike for their great scientific and personal support, always willing to answer my ongoing questions.

A great thanks goes to Dr. Alex Schulz who helped and inspired me a lot with his unlimited enthusiasm for scientific research, as well as with his invaluable skill for highly scientific and at the same time very illustrative explanations.

Furthermore I would like to thank Dr. Norbert Pirk for his great scientific support, always coming up with new ideas and approaches when I did not know how to carry on.

I would like to thank Niko Bornemann for taking me with him to Ny Ålesund, patiently ensuring that I did not cause any greater damage to the measurement systems. Besides the invaluable experience of having been to Svalbard, this thesis would have been much more difficult and exhausting without having had the opportunity to visit the study site and its surroundings.

I furthermore thank the whole SPARC working group for answering my annoying questions regarding calibration certificates and sensor specifications and many others who have contributed to this work.

Last but not least I want to thank Steffen for his enormous patience and emotional support during the last months. Thank you for always supporting and motivating me even when I was probably no pleasant company after having worked late into the night.

Bibliography

Abbott,B. W., Jones, J. B., Schuur, E. A. G., Chapin III, F. S., Bowden, W. B., Bret-Harte, M. S., Epstein, H. E., Flannigan, M. D., Harms, T. K., Hollingsworth, T. N., Mack, M. C., McGuire, A. D., Natali, S. M., Rocha, A. V., Tank, S. E., Turetsky, M. R., Vonk, J. E., Wickland, K. P., Aiken, G. R., Alexander, H. D., Amon, R. M. W., Benscoter, B. W., Bergeron, Y., Bishop, K., Blarquez, O., Bond-Lamberty, B., Breen, A. L., Buffam, I., Cai, Y., Carcaillet, C., Carey, S. K., Chen, J. M., Chen, H. Y. H., Christensen, T. R., Cooper, L. W., Cornelissen, J. H. C., de Groot, W. J., DeLuca, T. H., Dorrepaal, E., Fetcher, N., Finlay, J. C., Forbes, B. C., French, N. H. F., Gauthier, S., Girardin, M. P., Goetz, S. J., Goldammer, J. G., Gough, L., Grogan, P., Guo, L., Higuera, P. E., Hinzman, L., Hu, F. S., Hugelius, G., Jafarov, E. E., Jandt, R., Johnstone, J. F., Karlsson, J., Kasischke, E. S., Kattner, G., Kelly, R., Keuper, F., Kling, G. W., Kortelainen, P., Kouki, J., Kuhry, P., Laudon, H., Laurion, I., Macdonald, R. W., Mann, P. J., Martikainen, P. J., McClelland, J. W., Molau, U., Oberbauer, S. F., Olefeldt, D., Paré, D., Parisien, M.-A., Payette, S., Peng, C., Pokrovsky, O. S., Rastetter, E. B., Raymond, P. A., Raynolds, M. K., Rein, G., Reynolds, J. F., Robards, M., Rogers, B. M., Schädel, C., Schaefer, K., Schmidt, I. K., Shvidenko, A., Sky, J., Spencer, R. G. M., Starr, G., Striegl, R. G., Teisserenc, R., Tranvik, L. J., Virtanen, T., Welker, J. M., Zimov, S., 2016. Biomass offsets little or none of permafrost carbon release from soils, streams, and wildfire: an expert assessment. Environmental Research Letters 11 (3), 034014. 10.1088/1748-9326/11/3/034014.

Aubinet, M., Chermanne, B., Vandenhaute, M., Longdoz, B., Yernaux, M., Laitat, E., 2001. Long term carbon dioxide exchange above a mixed forest in the Belgian Ardennes. Agricultural and Forest Meteorology 108 (4), 293-315. 10.1016/S0168-1923(01)00244-1.

Aubinet, M., Vesala, T., Papale, D., 2012. Eddy covariance: a practical guide to measurement and data analysis, Springer, Berlin. 10.1007/978-94-007-2351-1.

Auer, L. H., Rosenberg, N. D., Birdsell K. H., Whitney, E.M., 1996. The effects of barometric pumping on contaminant transport, J. Contam. Hydrol. 24 (2), 145 – 166. 10.1016/S0169-7722(96)00010-1.

AC3, 2015. Overview. http://www.ac3-tr.de/overview/, 2020-05-26.

Amiro, B., 2010. Estimating annual carbon dioxide eddy fluxes using open-path analysers for cold forest sites. Agric. For. Meteorol. 150 (10), 1366–1372. 10.1016/j.agrformet.2010.06.007.

Bacher, S. M., 2019. Enhanced Warming and Wetting of the Active Layer Caused by Rain and Snow, Svalbard. Bachelor thesis (unpublished), University of Potsdam, Potsdam, Germany.

Bate, G. C., Smith, V. R., 1983. Photosynthesis and respiration in the sub-Antarctic tussock grass poa cookii. New Phytologist 95, 533–543. 10.1111/j.1469-8137.1983.tb03518.x.

Biskaborn, B., Smith, S. L., Noetzli, J., Matthes, H., Vieira, G., Streletskiy, D. A., Schoeneich, P., Romanovsky, V. E., Lewkowicz, A. G., Abramov, A., Allard, M., Boike, J., Cable, W. L., Christiansen, H. H., Delaloye, R., Diekmann, B., Drozdov, D., Etzelmüller, B., Grosse, G., Guglielmin, M., Ingeman-Nielsen, T., Isaksen, K., Ishikawa, M., Johansson, M., Johannsson, H., Joo, A., Kaverin, D., Kholodov, A., Konstantinov, P., Kröger, T., Lambiel, C., Lanckman, J.-P., Luo, D., Malkova, G., Meiklejohn, I., Moskalenko, N., Oliva, M., Phillips, M., Ramos, M., Sannel, A. B. K., Sergeev, D., Seybold, C., Skryabin, P., Vasiliev, A., Wu, Q., Yoshikawa, K., Zheleznyak, M., Lantuit, H., 2019. Permafrost is warming at a global scale. Nature Communications 10 (1), 1-11. 10.1038/s41467-018-08240-4.

Boike, J., Roth, K., Ippisch, O., 2003. Seasonal Snow Cover on Frozen Ground: Energy Balance Calculations of a Permafrost Site Near Ny-Ålesund, Spitsbergen. J. Geophys. Res. 108 (2), 1-11. 10.1029/2001JD000939.

Boike, J., Wille, C., and Abnizova, A., 2008. Climatology and summer energy and water balance of polygonal tundra in the Lena River Delta, Siberia. J. Geophys. Res., 113, G03025, 10.1029/2007JG000540.

Boike, J., Juszak, I., Lange, S., Chadburn, S., Burke, E., Overduin, P. P., Roth, K., Ippisch, O., Bornemann, N., Stern, L., Gouttevin, I., Hauber, E., Westermann, S., 2018. A 20-year record (1998–2017) of permafrost, active layer and meteorological conditions at a high Arctic permafrost research site (Bayelva, Spitsbergen). Earth Syst. Sci. Data 10, 355–390. 10.5194/essd-10-355-2018.

Burba, G. G., Anderson, D. J., Xu, L., McDermitt, D. K., 2006. Correcting apparent off-season CO2 uptake due to surface heating of a an open path gas analyzer: Process report of an ongoing study. Conference: Proceedings Agricultural and Forest Meteorology 27th Conference, San Diego, CA.

Burba, G. G., McDermitt, D. K., Grelle, A., Anderson, D. J., Xu, L., 2008. Addressing the influence of instrument surface heat exchange on the measurements of CO2 flux from open-path gas analyzers. Global Change Biol. 14 (8), 1854–1876. 10.1111/j.1365-2486.2008.01606.x.

Burba, G., 2013. Eddy Covariance Method for Scientific, Industrial, Agricultural and Regulatory Applications: A Field Book on Measuring Ecosystem Gas Exchange and Areal Emission Rates. LI-COR Biosciences, Lincoln, Nebraska.

Bussières, N., 2002. Thermal features of the Mackenzie Basin from NOAA AVHRR observations for summer 1994, Atmos.-Ocean 40 (2), 233–244. 10.3137/ao.400210.

Butterworth, B., Else, B., 2018. Dried, closed-path eddy covariance method for measuring carbon dioxide flux over sea ice. Atmospheric Measurement Techniques 11 (11), 6075-6090. 10.5194/amt-11-6075-2018.
Campbell Scientific Inc., 1998. CSAT3 manual. Campbell Scientific Inc., Shepshed, Loughborough, UK.
Ciais, P., Sabine, C., Bala, G., Bopp, L., Brovkin, V., Canadell, J., Chhabra, A., DeFries, R., Galloway, J., Heimann, M., Jones, C., Le Quéré, C., Myneni, R. B., Piao, S., Thornton, P., 2013. Climate Change 2013: The Physical Science Basis. Contribution of Working Group I to the Fifth Assessment Report of the Intergovernmental Panel on Climate Change. Cambridge University Press, United Kingdom and New York, NY, USA, 530.
Clarke, G. K. C., Waddington E.D., 1991. A three-dimensional theory of wind pumping. Journal of Glaciology 37 (125), 89-96. 10.1017/S0022143000042830.
Clarke, G. K. C., Fisher, D. A., Waddington, E.D., 1987. Wind pumping: a potentially significant heat source in ice sheets. Int. Symp. Physical Basis of Ice Sheet Modeling, IAHS Publ. 170, 169-180.
Clement, R. J., G. G. Burba G. G., Grelle, A., Anderson, D. J., Moncrieff, J. B., 2009. Improved trace gas flux estimation through IRGA sampling Optimization. Agric. For. Meteorol. 149 (3), 623–638. 10.1016/j.agrformet.2008.10.008.
Clements, W. E., Wilkening, M. H., 1974. Atmospheric pressure effects on transport across the earth-air interface. J. Geophys. Res. 79 (33), 5025–5029. 10.1029/JC079i033p05025.
Colbeck, S.C., 1989. Air movement of snow due to windpumping. Journal of Glaciology 35 (120), 209-213. 10.3189/S0022143000004524.
Collineau, S., Brunet, Y., 1993. Detection of turbulent coherent motions in a forest canopy part I: Wavelet analysis, Bound.-Lay. Meteorol. 65 (4), 357–379. 10.1007/BF00707033.
Corradi, C., Kolle, O., Walter, K., Zimov, S., Schulze, E.-D., 2005. Carbon dioxide and methane exchange of a north-east Siberian tussock tundra. Global Change Biology 11 (11), 1910–1925. 10.1111/j.1365-2486.2005.01023.x.
Cunningham, J., Waddington, E. D., 1993. Air flow and dry deposition of non-sea salt sulfate in polar firn: Paleoclimatic implications. Atmospheric Environment Part A 27 (17), 2943-2956. 10.1016/0960-1686(93)90327-U.
Dedering, U., 2010. Arctic Ocean relief location map. https://de.wikipedia.org/wiki/Datei:Arctic_Ocean_relief_location_map.png, 2019-07-07.
DWD, 2015. Surface analysis for 6:00 UTC on 3 March 2015. http://www1.wetter3.de/Archiv/archiv_dwd.html, 2020-05-26.
Ebenhoch, S., 2018. Discussion of the thermo-insulation effect of a seasonal snow cover on permafrost soil in Bayelva, Svalbard (1998 - 2017) with respect to current knowledge. Master thesis (unpublished), Heidelberg University, Heidelberg, Germany.
Elberling, B., Brandt, K. K., 2003. Uncoupling of microbial CO2 production and release in frozen soil and its implications for field studies of Arctic C cycling. Soil Biol. Biochem. 35 (2), 263–272. 10.1016/S0038-0717(02)00258-4.
Esau, I., Repina, I., 2012. Wind climate in Kongsfjorden, Svalbard, and attribution of leading wind driving mechanisms through turbulence-resolving simulations. Advances in Meteorology 16. 10.1155/2012/568454.
Finkelstein, P., Sims, P., 2001. Sampling Error in Eddy Correlation Flux Measurements. J. Geophysical Res. 106 (D4), 3503-3509. 10.1029/2000JD900731.
FLUXNET, 2015. https://fluxnet.fluxdata.org/wp-content/uploads/sites/3/2015-10-19_Global_Site_Year_2015-v2.jpg, 2019-07-07.
Foken, T., Göckede, M., Mauder, M., Mahrt, L., Amiro, B. D., Munger, J. W., 2004. Post-Field Data Quality Control. In: Lee, X., Massman, W., Law, B. (Eds.), Handbook of Micrometeorology. Atmospheric and Oceanographic Sciences Library 29, Springer, Dordrecht, 81-108.
Foken, T., Wichura, B., 1996. Tools for quality assessment of surface-based flux measurements. Agricultural and Forest Meteorology 78 (1-2), 83-105. 10.1016/0168-1923(95)02248-1.
Foken, T., 2016. Angewandte Meteorologie – Mikrometeorologische Methoden. Springer Spektrum, Berlin Heidelberg.
Førland, E., Hanssen-Bauer, I., Nordli, P., 1997. Climate statistics and longterm series of temperatures and precipitation at Svalbard and Jan Mayen, Det Norske Meteorologiske Institutt Klima Report 21/97.
Göckede, M., Foken, T., Aubinet, M., Aurela, M., Banza, J., 2008. Quality control of CarboEurope flux data - Part 1: Coupling footprint analyses with flux data quality assessment to evaluate sites in forest ecosystems. Biogeosciences 5 (2), 433-450. 10.5194/bg-5-433-2008.
Göckede, M., Kittler, F.,Schaller, C., 2019. Quantifying the impact of emission outbursts and non-stationary flow on eddy-covariance CH_4 flux measurements using wavelet techniques. Biogeosciences 16, 3113–3131. https://doi.org/10.5194/bg-16-3113-2019.

Goodrich, J. P., Oechel, W. C., Gioli, B., Moreaux, V., Murphy, P. C., Burba, G., Zona, D., 2016. Impact of different eddy covariance sensors, site set-up, and maintenance on the annual balance of CO_2 and CH_4 in the harsh Arctic environment. Agr. Forest Meteorol. 228–229, 239–251. 10.1016/j.agrformet.2016.07.008.

Graham, L. Risk, D., 2018. Explaining CO_2 fluctuations observed in snowpacks. Biogeosciences 15, 847–859. 10.5194/bg-2017-172.

Gu, L., Falge, E., Boden, T., Baldocchi, D. D., Black, T. A., Saleska, S.R., Suni, T., Vesala, T., Wofsy, S., Xu, L., 2005. Observing threshold determination for nighttime eddy flux filtering. Agric For Meteorol. 128 (3-4), 179–197. 10.1016/j.agrformet.2004.11.006.

Hanssen-Bauer, I., Solås, M. K., Steffensen, E. L., 1990. The Climate of Spitsbergen. DNMI-Report 39/90 KLIMA, 40pp.

Helbig, M., Wischnewski, K., Gosselin, G., Biraud, S., Bogoev, I., Chan, W., Euskirchen, E., Glenn, A., Marsh, P., Quinton, W., Sonnentag, O., 2016. Addressing a systematic bias in carbon dioxide flux measurements with the EC150 and the IRGASON open-path gas analyzers. Agricultural and Forest Meteorology 228-229, 349-359. 10.1016/j.agrformet.2016.07.018.

Hirata, R., Hirano, T., Mogami, J., Fujinuma, Y., Inupkai, K., Saigusa, N., Yamamoto, S., 2005. CO_2 flux measured by an open-path system over a larch forest during the snow-covered season. Phyton - Annales Rei Botanicae 45 (4), 347 - 351.

Hirsch, A., Trumbore, S., Goulden, M., 2004. The surface CO_2 gradient and pore-space storage flux in a high-porosity litter layer. Tellus B. 56 (4). 312 - 321. 10.1111/j.1600-0889.2004.00113.x.

Hodson, A., Tranter, M., Gurnell, A., Clark, M., Hagen, J. O., 2002. The hydrochemistry of Bayelva, a high arctic proglacial stream in Svalbard. J. Hydrol. 257 (1-4), 91–114. 10.1016/S0022-1694(01)00543-1.

Højstrup, J., 1993. Statistical data screening procedure. Meas. Sci. Technol. 4, 153-153. 0.1088/0957-0233/4/2/003.

Humlum, O., 2005. Holocene permafrost aggradation in Svalbard. Geol. Soc. Spec. Publ. 242 (1), 119–129. 10.1144/GSL.SP.2005.242.01.11.

Humphreys, E. R., Lafleur, P. M., 2011. Does earlier snowmelt lead to greater CO_2 sequestration in two low Arctic tundra ecosystems? Geophys. Res. Lett. 38 (9). 10.1029/2011GL047339.

ICOS, 2018. Bottom-up and top-down methods in national GHG emission reporting. Presented at the 3rd ICOS Science Conference in Prague, Czech Republic, 11-13 Sep 2018, https://www.slideshare.net/ICOS_RI/bottomup-and-topdown-methods-in-national-ghg-emission-reporting, 2019-07-14.

Isaksen, K., Nordli Ø., Førland, E. J., Łupikasza, E., Eastwood, S., Niedzwiedz, T., 2016. Recent warming on spitsbergen —influence of atmospheric circulation and sea ice cover. J. Geophys. Res. Atmos. 121 (11), 913–931. 10.1002/2016JD025606.

Jinho, A., Headly, M., Wahlen, M., Brook, E. J., Mayewski P. A., Taylor, K. C., 2008. CO_2 diffusion in polar ice: observations from naturally formed CO2 spikes in the Siple Dome (Antarctica) ice. J. Glaciol. 54 (187), 685–695. 10.3189/002214308786570764.

Jones, H.G., Pomeroy, J.W., Davies, T.D., Tranter, M. Marsh, P., 1999. CO_2 in Arctic snow cover: landscape form, in-pack gas concentration gradients, and the implications for the estimation of gaseous fluxes. Hydrol. Process. 13, 2977-2989. 10.1002/(SICI)1099-1085(19991230)13:18<2977::AID-HYP12>3.0.CO;2-#.

Kaimal, J. C., Finnigan, J. J., 1994. Atmospheric boundary layer flows. Their structure and measurement. Oxford university press, Oxford, UK.

Kappen, L., 1993. Plant activity under snow and ice, with particular reference to lichens. Arctic 46 (4), 297–302.

Katul, G. G., Parlange, M. B., 1995. Analysis of land-surface heat fluxes using the orthonormal wavelet approach. Water Resour. Res. 31 (11), 2743–2749.

Kittler, F., Eugster, W., Foken, T., Heimann, M., Kolle, O., Goeckede, M., 2017. High-quality eddy-covariance CO_2 budgets under cold climate conditions. Journal of Geophysical Research: Biogeosciences 122 (8). 10.1002/2017jg003830.

Kutzbach, L., Wille, C., Pfeiffer, E.-M., 2007. The exchange of carbon dioxide between wet arctic tundra and the atmosphere at the Lena River Delta. Northern Siberia. Biogeosciences 4 (5), 869–890. 10.5194/bgd-4-1953-2007.

Laemmel, T., Mohr, M., Schack-Kirchner, H., Schindler, D., Maier, M., 2017. Direct Observation of Wind-Induced Pressure-Pumping on Gas Transport in Soil. Soil Science Society of America Journal 81 (4), 770-774. 10.2136/sssaj2017.01.0034n.

Lafleur, P. M., Humphreys, E. R., 2008. Spring warming and carbon dioxide exchange over low Arctic tundra in central Canada. Global Change Biology 14 (4), 740-756. 10.1111/j.1365-2486.2007.01529.x.

Lee, X., Massman, W. J., Law, B., 2004. Handbook of Micrometeorology, Kluwer Academic Publishers, the Netherlands.

LI-COR Inc., 2001. LI-7500 Manual. LI-COR Biosciences, Lincoln, Nebraska.
LI-COR Inc., 2009. LI-7500A Manual. LI-COR Biosciences, Lincoln, Nebraska.
LI-COR Inc., 2015. LI-7500RS Manual. LI-COR Biosciences, Lincoln, Nebraska.
LI-COR Biosciences, 2017. Eddy Covariance Processing Software (Version 7.0.6) [Software]. Available at www.licor.com/EddyPro, 2020-05-26.
Licor Inc., 2020. EddyPro version 7 manual, LI-COR Biosciences, Lincoln, Nebraska.
Lloyd, C. R., 2001a. On the Physical Controls of the Carbon Dioxide Balance at a High Arctic Site in Svalbard. Theor. Appl. Climatol. 70 (1), 167–182. 10.1007/s007040170013.
Lloyd, C. R., Harding, R. J., Friborg, T., Aurela, M., 2001. Surface Fluxes of Heat and Water Vapour from Sites in the European Arctic. Theor. Appl. Climatol. 70 (1), 19–33. 10.1007/s007040170003.
Lüers, J., Westermann, S., Piel, K., Boike, J., 2014. Annual CO_2 budget and seasonal CO_2 exchange signals at a High Arctic permafrost site on Spitsbergen, Svalbard archipelago. Biogeosciences 11 (1). 10.5194/bgd-11-1535-2014.
Lüers, J., Bareiss, J., 2010. The effect of misleading surface temperature estimations on the sensible heat fluxes at a high Arctic site – the Arctic Turbulence Experiment 2006 on Svalbard (ARCTEX-2006). Atmos. Chem. Phys. 9 (4), 16913-16939. 10.5194/acpd-9-16913-2009.
Lüers, J., Bareiss, J., 2011. Direct near-surface measurements of sensible heat fluxes in the arctic tundra applying eddy-covariance and laser scintillometry – The Arctic Turbulence Experiment 2006 on Svalbard (ARCTEX-2006), Theor. Appl. Climatol. 105 (3), 387–402. 10.1007/s00704-011-0400-5.
Lüers, J., Bareiss, J., 2013. Turbulent flux and meteorological measurements during ARCTEX-2006 campaign, Datasets #811060 to #811066, PANGAEA Data Publisher for Earth Environ. Sci., doi:10.1594/PANGAEA.811066.
Lüers, J.. Boike, J., 2013. Time series of annual atmospheric CO2- fluxes above a high-arctic permafrost site, Svalbard (Norway), 2008-03 to 2009-03, Department of Micrometeorology, University of Bayreuth, 2013.
Lund, M., Falk, J. M., Friborg, T., Mbufong, H. N., Sigsgaard, C., Soegaard, H., Tamstorf, M.P., 2012. Trends in CO2 exchange in a high Arctic tundra heath, 2000–2010. Journal of Geophysical Research: Biogeosciences, 117(G2). 10.1029/2011JG001901.
Ma, J., Liu, R., Tang, L.-S., Lan, Z.-D., and Li, Y., 2014. A downward CO_2 flux seems to have nowhere to go. Biogeosciences 11 (22), 6251–6262. 10.5194/bg-11-6251-2014.
Mahrt, L., 1991. Eddy Asymmetry in the Sheared Heated Boundary Layer. J. Atmos. Sci. 48 (3), 472–492. 10.1175/1520-0469(1991)048<0472:EAITSH>2.0.CO;2.
Massman, W. J., Lee, X., 2002. Eddy covariance flux corrections and uncertainties in long term studies of carbon and energy exchanges. Agric For Meteorol 113 (1-4), 121–144. 10.1016/S0168-1923(02)00105-3.
Massman, W. J., Sommerfeld, R. A., Mosier, A. R., Zeller, K. F., Hehn, T. J., Rochelle, S. G., 1997. A model investigation of turbulence driven pressure-pumping effects on the rate of diffusion of CO_2, N_2O, and CH_4 through layered snowpacks. J Geophys Res 102 (D15), 18851–18863. 10.1029/97JD00844.
Massman, W. J., Sommerfield, R. A., Zeller, K. F., Hehn, T. J., Hudnell, L., and Rochelle, S. G., 1995. CO_2 flux through a Wyoming seasonal snowpack: diffusional and pressure pumping effects. In: Tonnessen, K. A., Williams, M. W., Tranter, M. (Eds.), Biogeochemistry of Seasonally Snow-Covered Catchments, IAHS Press, Wallingford, UK, 71–79.
Massman, W. J., 2006. Advective transport of CO2 in permeable media induced by atmospheric pressure fluctuations: 1. An analytical model. J. Geophys. Res. 111 (G3). 10.1029/2006JG000163.
Massman, W., Frank, J. M., 2006. Advective transport of CO_2 in permeable media induced by atmospheric pressure fluctuations: 2. Observational evidence under snowpacks. J. Geophys. Res. 111. 10.1029/2006JG000164.
Mauder, M., Cuntz, M., Drüe, C., Graf, A., Rebmann, C., Schmid, H. P., Schmidt, M., and Steinbrecher, R., 2013. A strategy for quality and uncertainty assessment of long-term eddycovariance measurements. Agr. Forest Meteorol. 169, 122–135. 10.1016/j.agrformet.2012.09.006.
Mauder, M., Foken, T., 2004. Documentation and Instruction Manual of the Eddy Covariance Software Package TK2. University of Bayreuth, Bayreuth, Germany. 10.5194/bg-5-451-2008.
Mikan, C., Schimel, J., Doyle, A., 2002. Temperature Controls of Microbial Respiration in Arctic Tundra Soils Above and Below Freezing. Soil Biology and Biochemistry 34 (11), 1785-1795. 10.1016/S0038-0717(02)00168-2.
Miller, L. A., Fripiat, F., Else, B. G. T., Bowman, J. S., Brown, K. A., Collins, E. R., Ewert, M., Fransson, A., Gosselin, M., Lannuzel, D., Meiners, K. M., Michel, C., Nishioka, J., Nomura, D., Papadimitriou, S., Russell, L. M., Sørensen, L. L., Thomas, D. N., Tison, J.-L., van Leeuwe, M. A., Vancoppenolle, M., Wolff, E. W., Zhou, J., 2015. Methods for biogeochemical studies of sea ice: The state of the art, caveats, and recommendations. Elem. Sci. Anthr. 3. 10.12952/journal.elementa.000038.

Moncrieff, J. B., Massheder, J. M., de Bruin, H., Ebers, J., Friborg, T., Heusinkveld, B., Kabat, P., Scott, S., Soegaard, H., Verhoef, A., 1997. A system to measure surface fluxes of momentum, sensible heat, water vapor and carbon dioxide. Journal of Hydrology 188-189 (1-4), 589-611. 10.1016/S0022-1694(96)03194-0.

Moncrieff, J. B., Clement, R., Finnigan, J., Meyers, T., 2004. Averaging, detrending and filtering of eddy covariance time series. In: Lee, X., Massman, W. J., Law, B. E. (Eds.), Handbook of micrometeorology: a guide for surface flux measurements. Dordrecht: Kluwer Academic, 7-31.

NASA Goddard Institute for Space Studies Team https://data.giss.nasa.gov/gistemp/

Natali, S.M., Watts, J.D., Rogers, B.M., et al., 2019. Large loss of CO_2 in winter observed across the northern permafrost region. Nat. Clim. Chang. 9, 852–857. 10.1038/s41558-019-0592-8.

Norwegian Polar Institute, n.d., Maps of Svalbard, Retrieved from https://toposvalbard.npolar.no on 2020-04-08.

Novak, M.D., Chen, W., Orchansky, A. L., Ketler, R., 2000. Turbulent exchange processes within and above a straw mulch. Agric. For. Meteorol. 102 (2), 139–154. 10.1016/S0168-1923(00)00095-2.

Oechel, W. C., Laskowski, C. A., Burba, G., Gioli, B., Kalhori, A. A. M., 2014. Annual patterns and budget of CO2 flux in an Arctic tussock tundra ecosystem. J. Geophys. Res. Biogeosci. 119 (3), 323–339. 10.1002/2013JG002431.

Ono, K., Miyata, A., Yamada, T., 2007. Apparent downward CO2 flux observed with open-path eddy covariance over a non-vegetated Surface. Theor. Appl. Climatol. 92 (3–4), 195–208. 10.1007/s00704-007-0323-3.

Orvig, S., 1970. World survey of Climatology. Climate of the Polar regions, Volume 14. Elsevier Publishing Company. Amsterdam-London-New York.

Papale, D., Reichstein, M., Aubinet, M., Canfora, E., Bernhofer, C., Kutsch, W., Longdoz, B., Rambal, S., Valentini, R., Vesala, T., Yakir, D., 2006. Towards a standardized processing of Net Ecosystem Exchange measured with eddy covariance technique: algorithms and uncertainty estimation. Biogeosciences 3 (4), 571–583. 10.5194/bg-3-571-2006.

Pedersen, C., 2013. Zeppelin Webcamera Time Series [Data set]. Norwegian Polar Institute. https://doi.org/10.21334/npolar.2013.9fd6dae0, 2020-05-26.

Pirk, N., Sievers, J., Mertes, J., Parmentier, F.-J. W., Mastepanov, M., Christensen, T. R., 2017. Spatial variability of CO_2 uptake in polygonal tundra: assessing low-frequency disturbances in eddy covariance flux estimates. Biogeosciences 14 (12), 3157–3169. 10.5194/bg-14-3157-2017.

Powers, D., Colbeck, S. C., Oneill, K., 1985. Experiments on Thermal Convection in Snow. Ann. Glaciol. 6, 43–47. 10.3189/1985aog6-1-43-47.

Price, A. J., Dunne, T., 1976. Energy balance computations of snowmelt in a Subarctic area. Water Resour. Res. 12 (4), 686– 694. 10.1029/WR012i004p00686.

Rees, W., 1993. Infrared emissivities of arctic land cover types. Int. J. Remote Sens. 14 (5), 1013–1017. 10.1080/01431169308904392.

Rinke, A., Maturilli, M. Graham, R., Matthes, H., Handorf, D., Cohen, L., Hudson, S., Moore, J., 2017. Extreme cyclone events in the Arctic: Wintertime variability and trends. Environmental Research Letters 12 (9). 10.1088/1748-9326/aa7def.

Roedel, W., Wagner, T., 2011. Physik unserer Umwelt: Die Atmosphäre. Springer, Berlin/Heidelberg.

Roth, K., Schulin, R., Flühler, H., Attinger, W., 1990. Calibration of time domain reflectometry for water content measurement using a composite dielectric approach. Water Resour. Res. 26 (10), 2267 – 2273. 10.1029/WR026i010p02267.

Roth, K., Boike, J., 2001. Quantifying the Thermal Dynamics of a Permafrost Site Near Ny-Ålesund, Svalbard. Water Resour. Res. 37 (12), 2901–2914. 10.1029/2000WR000163.

Schaefer, K., Lantuit, H., Romanovsky, V. E., Schuur, E. A. G., Ronald Witt, R., 2014. The impact of the permafrost carbon feedback on global climate. Environmental Research Letters 9 (8). 10.1088/1748-9326/9/8/085003.

Schaller, C., Kittler, F., Foken, T., Göckede, M., 2019. Characterisation of short-term extreme methane fluxes related to non-turbulent mixing above an Arctic permafrost ecosystem. Atmos. Chem. Phys. 19, 4041–4059. 10.5194/acp-2018-277.

Schuur, E. A. G., McGuire, A. D., Schädel, C., Grosse, G., Harden, J. W., Hayes, D. J., Hugelius, G., Koven, C. D., Kuhry, P., Lawrence, D. M., Natali, S. M., Olefeldt, D., Romanovsky, V. E., Schaefer, K., Turetsky, M. R., Treat, C. C., Vonk, J. E., 2015. Climate change and the permafrost carbon feedback. Nature 520, 171-179. 10.1038/nature14338.

Seok, B., Helmig, D., Williams, M. W., Liptzin, D., Chowanski, K., Hueber, J., 2009. An automated system for continuous measurements of trace gas fluxes through snow: an evaluation of the gas diffusion method at a subalpine forest site, Niwot Ridge, Colorado. Biogeochemistry 95, 95–113. 10.1007/s10533-009-9302-3.

Serreze, M., Barry, R., 2011. Processes and impacts of Arctic amplification: A research synthesis. Global and Planetary Change 77 (1), 85-96. 10.1016/j.gloplacha.2011.03.004.
Sievers, J., 2020. Ogive optimization toolbox (https://www.mathworks.com/matlabcentral/fileexchange/53545-ogive-optimization-toolbox), MATLAB Central File Exchange, 2020-05-26.
Sievers, J., Papakyriakou, T., Larsen, S. E., Jammet, M. M., Rysgaard, S., Sejr, M. K., Sørensen, L. L., 2015. Estimating surface fluxes using eddy covariance and numerical ogive optimization. Atmos. Chem. Phys. 15, 2081–2103. 10.5194/acp-15-2081-2015.
Soegaard, H., Nordstroem, C., 1999. Carbon dioxide exchange in a high-arctic fen estimated by eddy covariance measurements and modelling. Global Change Biology 5 (5), 547–562. 10.1111/j.1365-2486.1999.00250.x.
Sorensen, L. L., Larsen, S. E., 2010. Atmosphere-Surface Fluxes of CO_2 using Spectral Techniques. Bound.-Lay. Meteorol. 136 (1), 59–81. 10.1007/s10546-010-9499-7.
Stull, R. B., 1988. An Introduction to Boundary Layer Meteorology. The Netherlands: Kluwer Academic Publishers, Dordrecht.
Sturm, M., 1991. The role of thermal convection in heat and mass transport in the subarctic snow-cover. Cold Regions Research and Engineering Laboratory (U.S.), CRREL Technical Report 91-19, Army Corps of Engineers Cold Regions Research&Engineering Laboratory, Hanover, NH, USA.
Sturm M., Johnson, J. B., 1991. Natural convection in the Subarctic snow cover. Journal of Geophysical Research 96 (B7), 11657-11671. 10.1029/91JB00895.
Sveinbjörnsson, B., Oechel, W. C., 1981. Controls on CO_2 exchange in two polytrichum moss species. 2. The implication of belowground plant parts on the whole-plant carbon balance. Oikos 36 (3), 348–354. 10.2307/3544632.
Takagi, K., Nomura, M., Ashiya, D., Takahashi, H., Sasa, K., Fujinuma, Y., Shibata, H., Akibayashi, Y., Koike, T., 2005. Dynamic carbon dioxide exchange through snowpack by wind-driven mass transfer in a conifer-broadleaf mixed forest in northernmost Japan. Global Biogeochemical Cycles 19 (2). 10.1029/2004GB002272.
Takle, E. S., Massman, W. J., Brandle, J. R. , Schmidt R.A., Zhou X. H., Litvina I. V., Garcia R., Doyle G., Ric C. W., 2004. Influence of high-frequency ambient pressure pumping on carbon dioxide efflux from soil. Agricultural and Forest Meteorology 124 (3-4), 193–206. 10.1016/j.agrformet.2004.01.014.
Tarnocai, C., Canadell, J. G., Schuur, E. A. G., Kuhry, P., Mazhitova, G., Zimov, S., 2009. Soil organic carbon pools in the northern circumpolar permafrost region. Global Biogeochem. Cycles 23 (2). 10.1029/2008GB003327.
Trevino, G., Andreas, E. L., 1996. On wavelet analysis of nonstationary turbulence. Bound.-Lay. Meteorol. 81, 271–288. 10.1007/BF02430332.
Vickers, D., Mahrt, L., 1997. Quality control and flux sampling problems for tower and aircraft data. J. Atmos. Ocean. Tech. 14 (3), 512–526. 10.1175/1520-0426(1997)014<0512:QCAFSP>2.0.CO;2.
Walton, D. W. H., Doake, C. S. M., 1987. Antarctic Science. Cambridge Univ. Press, Cambridge, New York.
Webb, E., Pearman, G., Leuning, R., 1980. Correction of flux measurements for density effects due to heat and water vapor transfer. Quarterly Journal of Royal Meteorological Society 106, 85-100. 10.1002/qj.49710644707.
Wei, L., Qin, T., Li, C., 2017. Seasonal and inter-annual variations of Arctic cyclones and their linkage with Arctic sea ice and atmospheric teleconnections. Acta Oceanologica Sinica, 36 (10), 1–7. 10.1007/s13131-017-1117-9.
Weiss, R.F., 1974. Carbon dioxide in water and seawater: the solubility of a non-ideal gas. Mar. Chem. 2 (3), 203-215. 10.1016/0304-4203(74)90015-2.
Wendisch, M., Brückner, M., Burrows, J. P., Crewell, S., Dethloff, K., Ebell, K., Lüpkes, Ch., Macke, A., Notholt, J., Quaas, J., Rinke, A., Tegen, I., 2017. Understanding causes and effects of rapid warming in the Arctic. Eos 98. 10.1029/2017EO064803.
Westermann, S., 2010. Sensitivity of Permafrost, Doctor of Natural Sciences PhD thesis, Combined Faculties for the Natural Sciences and for Mathematics, Ruperto-Carola University, Heidelberg, Germany, 2010.
Westermann, S., Lüers, J., Langer, M., Piel, K., Boike, J., 2009. The annual surface energy budget of a high-arctic permafrost site on Svalbard, Norway. The Cryosphere 3 (2), 245–263. 10.5194/tcd-3-631-2009.
Westermann, S., Langer, M., Boike, J., 2011. Spatial and temporal variations of summer surface temperatures of high-arctic tundra on Svalbard – Implications for MODIS LST based permafrost monitoring. Remote Sens. Environ., 115 (3), 908–922. 10.1016/j.rse.2010.11.018.
Wilczak, J., Oncley, S., Stage, S., 2001. Sonic Anemometer Tilt Correction Algorithms. Boundary-Layer Meteorology 99 (1), 127-150. 10.1023/A:1018966204465.

Zhang, X., Walsh, J. E., Zhang, J., Bhatt, U. S., Ikeda, M., 2004. Climatology and Interannual Variability of Arctic Cyclone Activity: 1948–2002. J. Clim. 17 (12), 2300–2317. 10.1175/1520-0442(2004)017<2300:CAIVOA>2.0.CO;2.

Zhang, J., Lee, X., Song, G., Han, S., 2011. Pressure correction to the long-term measurement of carbon dioxide flux. Agricultural and Forest Meteorology 151 (1), 70-77. 10.1016/j.agrformet.2010.09.004.

Appendix

A.1 Example for the planar fit coordinate rotation

The following section analyzes the performance of the planar fit method as an alternative to the double rotation scheme at the example of the negative single peak event between 21:30 UTC on March 2 and 7:00 on March 3, used in the first case study (Section 5.6.1).

Given the three distinct local wind directions at the Bayelva site (section 5.3.2.1) a sectorwise application of the planar fit method is reasonable. Therefore the planar fit methods is applied independently for each of the three main wind sectors occurring at the Bayelva site (Figure A.1) and the appropriate rotation matrix is chosen, depending on the current wind direction.

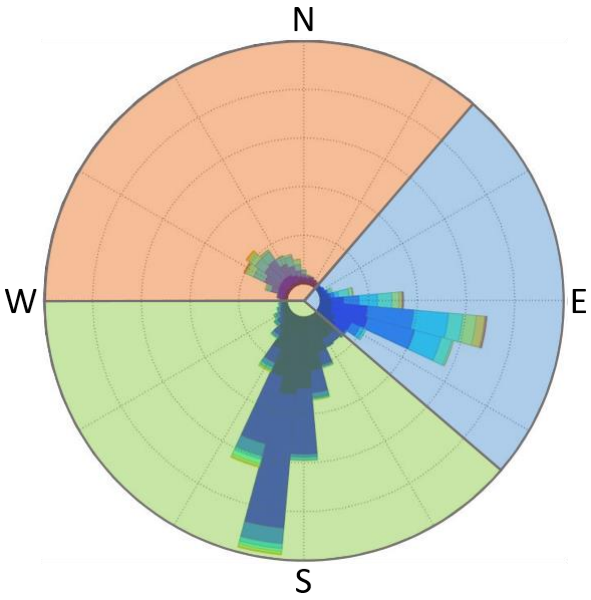

Figure A.1: Wind direction sectors featuring the three prevailing wind directions at the Bayelva site as used in the planar fit method. Sectors span the wind directions between 40 ° and 130 °, 130° and 270 ° and 270° and 40°, respectively.

For the present event the planar fit parameters for the three sectors are calculated based on the time period between 18.02.2015 and 18.03.2015, during which all of the three main wind directions are represented sufficiently. Figure A.2 reveals how the north-western slope of the study site determines the interdependencies between the three components of the unrotated mean wind vector. For example the vertical wind speed is strongly positive when the wind comes from the northwest and rises along the terrain slope in negative y-direction of the unrotated coordinate system. The vertical wind velocity therefore strongly increases with increasingly negative values of $\bar{v}$, while for the north western wind sector there is no strong dependency between the $\bar{w}$ and the $\bar{u}$ component of the wind vector. On the contrary when coming from the southwestern or eastern sector, the air descends along the slope of the terrain, resulting in a negative vertical wind component. Fitting a plane through the wind components data, based on equations 4.16 – 4.19, results in the planar fit parameters and rotation angles, listed in table A.1.

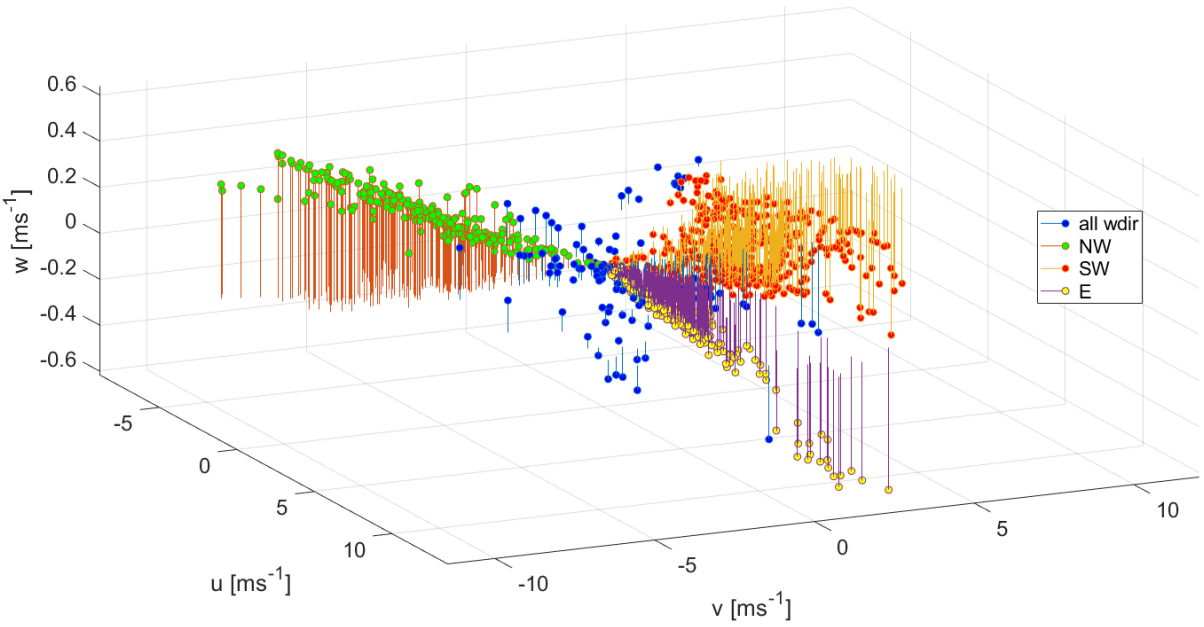

Figure A.2: Interdependencies between the three unrotated mean wind components for the three prevailing wind directions at the Bayelva site, namely wind coming roughly from the north-west (NW), the south-west (SW) and the east (E), between 18.02.2015 and 18.03.2015. Blue symbols mark wind directions which deviate from the main wind sectors.

Table A.1: Planar fit parameters and the corresponding rotation angles for the three wind sectors.

Wind sector [°]	b_0 [ms^{-1}]	b_1	b_2	α [°]	β [°]
40 - 130	0.0033236	-0.0427056	-0.0528927	2.4420	3.0277
130 - 270	-0.0127094	-0.0300339	-0.0612789	1.7171	3.5066
270 - 40	0.0150634	-0.0277072	-0.0440120	1.5856	2.5201

The best-fit plane is found to account for 97 % of the variance of $\overline{w}$. Residual vertical velocities that remain after subtracting the best-fit plane are shown in Figure A.3. Their magnitudes are clearly much smaller, and their distribution is nearly random except for a remaining slightly positive correlation between $\overline{w}$ and $\overline{v}$ for the north western wind sector.

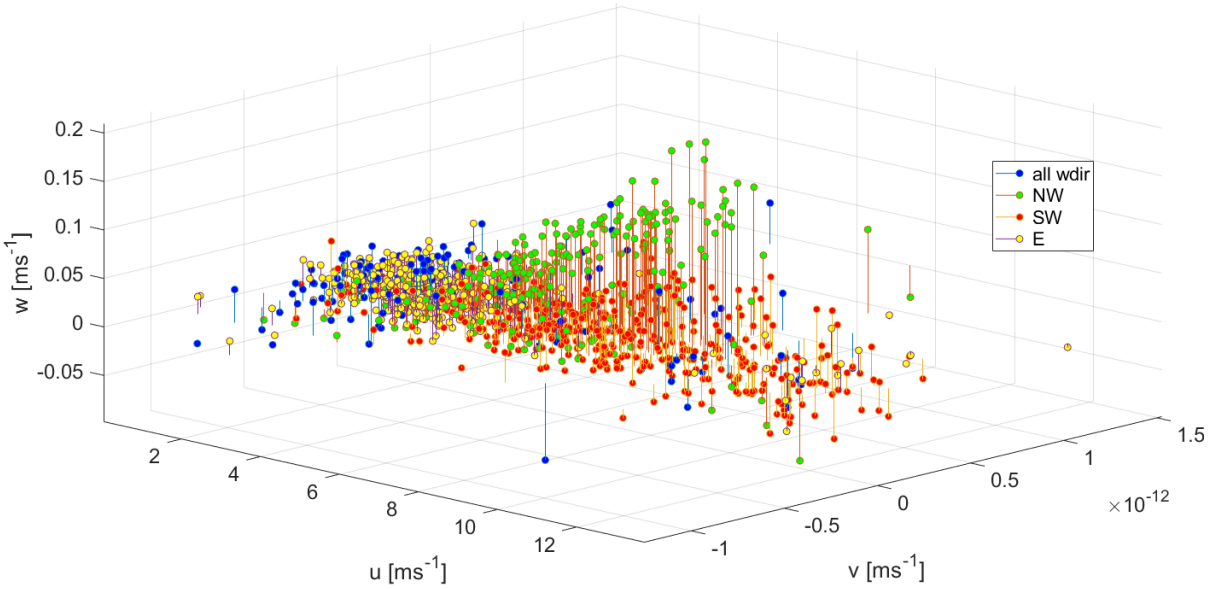

Figure A.3: Interdependencies between the three mean wind components after the planar fit rotation for the three prevailing wind directions at the Bayelva site, namely wind coming roughly from the north-west (NW), the south-west (SW) and the east (E), between 18.02.2015 and 18.03.2015. Blue symbols mark wind directions which deviate from the main wind sectors.

In Figure A.4 the specific effect of the planar fit rotations at the Bayelva site is visualized for the example of the wind coming from the south western wind sector. For the whole planar fit period of March 2015 the components of the wind vector in the instrument frame are rotated along the x and y axis to place the z axis approximately orthogonal to the slope of the terrain in order to nullify the monthly mean of the vertical wind velocity (Figure A.4 a). Subsequently the resultant intermediate coordinate system is rotated around its z-axis by γ, to align the x-axis with the currently prevailing wind direction of about 190 ° in this example (Figure A.4 b.

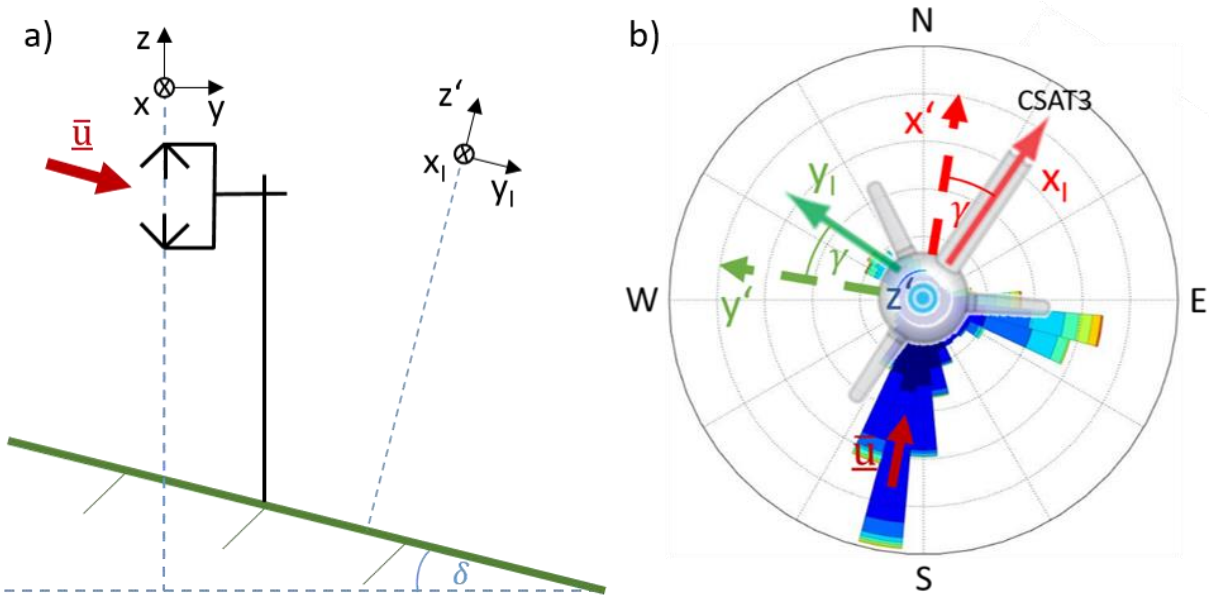

Figure A.4: Schematic illustration of the planar fit rotations at the Bayelva site from the original axes x, y, z over intermediate axes x_I, y_I, z_I to the final axes x', y', z'. **(a)** First rotation to nullify the vertical wind speed. The slope angle δ amounts to approximately 5 ° at the study site. **(b)** Second rotation to align the x-axis with the mean streamlines.

A.2 Overview of all FCO_2 events detected during the study period

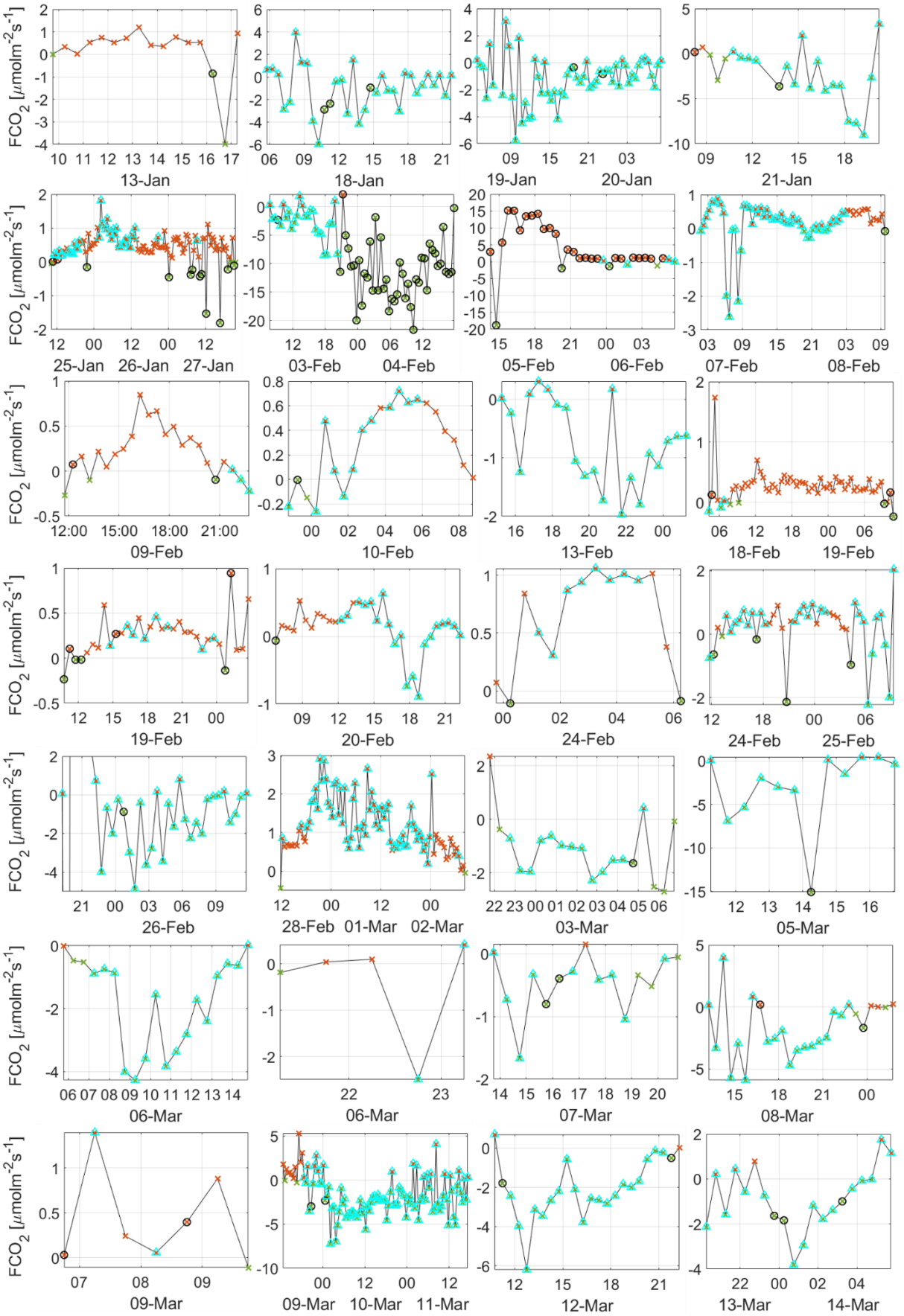

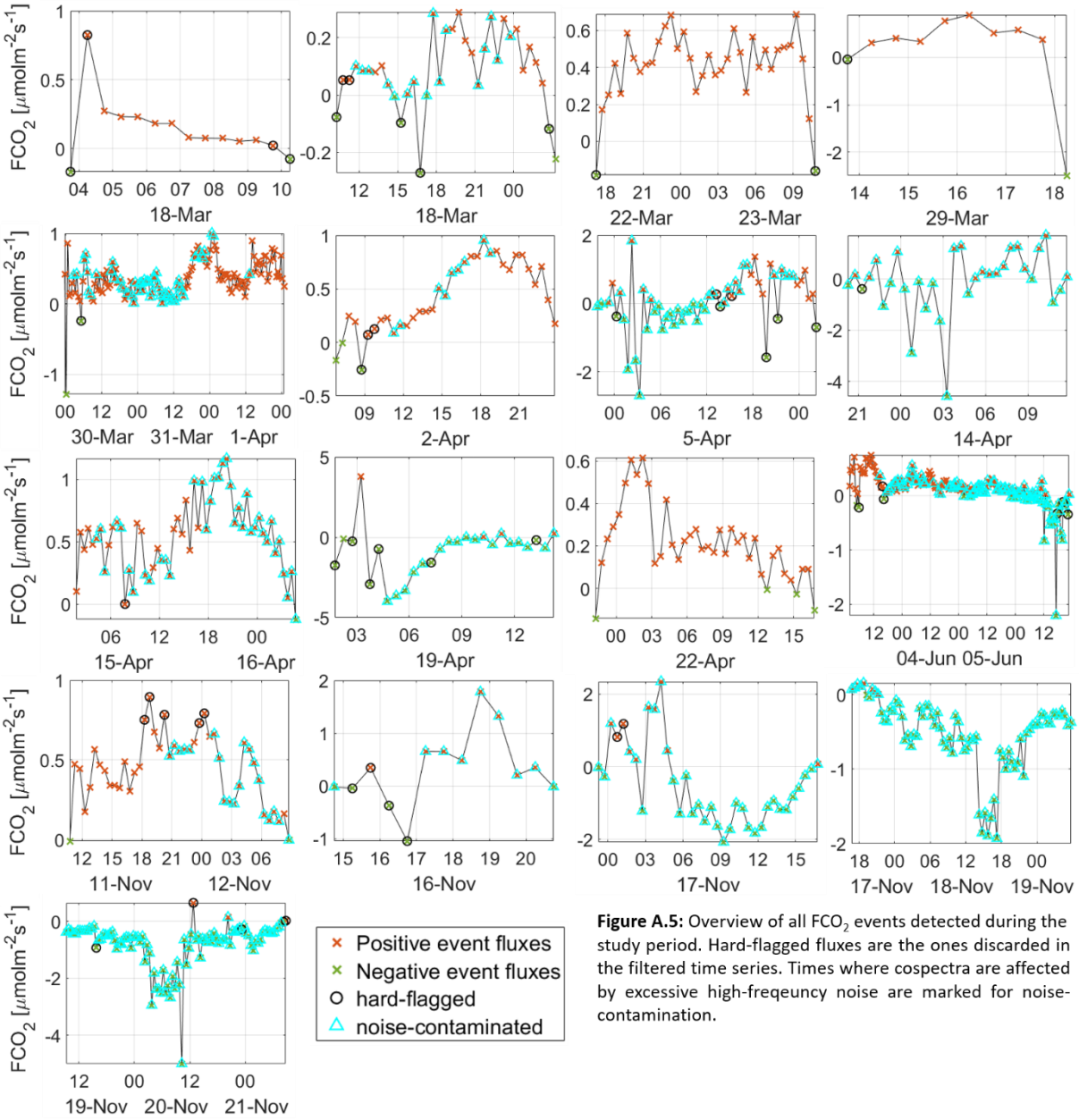

Figure A.5: Overview of all FCO_2 events detected during the study period. Hard-flagged fluxes are the ones discarded in the filtered time series. Times where cospectra are affected by excessive high-freqeuncy noise are marked for noise-contamination.

A.3 Symbols

Table A.1: Overview of the symbols used in this thesis.

$\bar{a}$	Mean value of quantity a
a'	Turbulent part of quantity a (deviation of a from its mean value)
$\overline{a'b'}$	Covariance of the quantities a and b
F_ξ	Vertical turbulent flux of quanity ξ
H	Sensible heat flux
LE	Latent heat flux
E	Water vapor flux
$L_{v,s}$	Latent heat of vaporization/sublimation
r_ξ	Mixing ratio of the quantity ξ
c_ξ	Molar density of the quantity ξ
n_ξ	Amount of quantity ξ
SF_ξ	Storage flux of quantity ξ
α, β, γ	Rotation angles
x, y, z	Coordinate system of the anemometer
x', y', z'	Intermediate anemometer coordinate system
x_I, y_I, z_I	Anemometer coordinate system after rotation
$\vec{v}$	Three dimensional wind vector
u, v, w	Components of the three dimensional wind vector
u_*	Friction velocity
T	Temperature
T_s	Sonic temperature
θ_v	Virtual potential temperature
$LW_{in,out,net}$	Incoming, outgoing, net longwave radiation
$SW_{in,out,net}$	Incoming, outgoing, net shortwave radiation
p	Atmospheric pressure
p_ξ	Partial pressure of quantity ξ
e	Water vapor pressure
ρ	Air density
ρ_d	Dry air density
ρ_v	Water vapor density
L	Obukhov length
ζ	Stability parameter
R_i	Bulk Richardson number
δ	Snow depth
η	Snow porosity
θ_w	Volumetric liquid water content
$\rho_{a,air,ice,w}$	Density of snow, air, ice, water
$\tau_{a,air,ice,w}$	Dielectric constant of snow, air, ice, water
ε	Emissivity
U_T	Transport velocity
$D_{(n,s,u)}$	Bulk transfer coefficient for neutral, stable, unstable conditions
MAD	Median absolute deviation
μ	Ratio of molar masses of air and water
c_p	Specific heat capacity of air at constant pressure
g	Gravitational constant
κ	von Kármán constant
R	Ideal gas constant
σ	Stefan-Boltzman constant
h_m	Measuring height
Δz	Distance between snow surface and measuring height
z_0	Roughness length

S_ξ	Spectrum of the quantity ξ
C_{ab}	Cospectrum of the quantities a and b
k	Wave number
f	Frequency
t	Time

Eidesstattliche Erklärung

Hiermit versichere ich, dass ich die vorliegende Masterarbeit selbstständig und nur unter Zuhilfenahme der ausgewiesenen Hilfsmittel angefertigt habe.
Sämtliche Stellen, die im Wortlaut oder dem Sinn nach anderen gedruckten oder im Internet verfügbaren Werken entnommen sind, habe ich durch genaue Quellenangaben kenntlich gemacht.

Siegburg, den 27.05.2020

_____

Katharina Jentzsch